Ph.D. DISSERTATION

STUDY ON IMPROVEMENT OF THREE-DIMENSIONAL DISPLAYS BASED ON MULTI-VIEW DISPLAY AND PINHOLE-TYPE INTEGRAL IMAGING

다시점 디스플레이와 핀홀 방식 집적영상에 기반한 3차원 디스플레이의 개선에 관한 연구

BY

JAE-HYUN JUNG

AUGUST 2012

DEPARTMENT OF ELECTRICAL ENGINEERING AND
COMPUTER SCIENCE
COLLEGE OF ENGINEERING
SEOUL NATIONAL UNIVERSITY

Abstract

STUDY ON IMPROVEMENT OF THREE-DIMENSIONAL DISPLAYS BASED ON MULTI-VIEW DISPLAY AND PINHOLE-TYPE INTEGRAL IMAGING

JAE-HYUN JUNG
DEPARTMENT OF ELECTRICAL ENGINEERING AND COMPUTER SCIENCE
COLLEGE OF ENGINEERING
SEOUL NATIONAL UNIVERSITY

This dissertation presents studies on improvement of three-dimensional (3D) displays based on multi-view display and pinhole-type integral imaging. Among various types of 3D displays, integral imaging and multi-view display such as parallax barrier and lenticular 3D display are almost commercialized autostereoscopic 3D display. For commercialization, autostereoscopic 3D display has three issues that are limitation of display technology, human factors related on human visual system and optical information processing technology. In this dissertation, the author will address the studies about the improvement methods for multi-view display and pinhole-type integral imaging in three issues.

In the issue of display technology, the improvement methods of pinhole-type integral imaging using electroluminescent (EL) film and color filters on display panel are proposed to enhance the viewing angle, resolution, ray density and two-dimensional (2D)/3D convertibility. For large expressible depth range and 2D/3D convertibility in pinhole-type integral imaging, pinhole-type integral imaging is modified by new light

source conversion layer based on EL film. The EL film has the advantage that it can operate continuously even when it is cut or punctured. Using this characteristic, the author generates an array of pinholes on an EL film to form a point light source array for reconstructing 3D images based on integral imaging. Taking advantage of the flexibility of EL films, a 2D/3D convertible integral imaging system with a wide viewing angle using a curved EL film is proposed which is extended to 360-degree viewable cylindrical 3D display system. For enhancement of ray density, resolution and expressible depth range in pinhole-type integral imaging, the system using color filter pinhole array on liquid crystal display panel with projection scheme is proposed. A color filter structure on liquid crystal display panel acts as pinhole array in integral imaging with separation of color channel. The use of color filter pinhole array and projection scheme can enlarge the region of one-elemental image and improve the resolution and ray density remarkably.

In addition to the improvement of pinhole-type integral imaging, analysis and convergence of multi-view display and one-dimensional (1D) integral imaging are presented for improvement of characteristics in autostereoscopic display. For the convergence of two different autostereoscopic 3D display, multi-view display and integral imaging, light field analysis of spatio-angular distribution and its frequency domain analysis are performed. From the analysis, the convergence type of autostereoscopic 3D display based on multi-view display and 1D integral imaging is proposed by using time-multiplexing and sub-pixel multiplexing technique.

On another issue in autostereoscopic 3D display, the depth resolution and accommodation response of human factors in multi-view display and integral imaging are researched. To find the effect of fundamental depth resolution and cardboard effect to the perceived depth resolution in multi-view display, the fundamental depth resolution and the cardboard effect from the synthesis process in the multi-view 3D TV broadcasting are analyzed and a subjective test is performed. In addition, the analysis and measurement of accommodation response of integral imaging with satisfying super multi-view display is performed to reveal the relation between the accommodation response of integral imaging and super multi-view condition.

On the other issue of autostereoscopic 3D display, the optical information processing from elemental image and multi-view images in depth extraction and computational

pickup method without pseudoscopic problem is presented. A more accurate depth extraction algorithm using optical flow from sub-images of elemental image is proposed and its applications are also presented in this dissertation.

Keywords: Three-dimensional display, multi-view display, integral imaging, pinhole-type integral imaging, depth resolution, accommodation, depth extraction, object reconstruction

Student number: 2007-21085

Contents

List of Figures

List of Tables

Chapter 1

Introduction

1.1 Overview of autostereoscopic three-dimensional displays

The three-dimensional (3D) display, which shows various views of an object, is thought of as the ultimate form of display by optical scientists and engineers and aroused their endeavors in the history of 3D display. As shown in Table 1.1, 3D display is classified to autostereoscopic, stereoscopic 3D display and other methods by the use or non-use of special glasses on the part of viewer [1].

After early record of stereoscopy in 1838 by Sir Charles Wheatstone, some pioneers appeared in the history of 3D display from the end of 19th century to early 20th century [2, 3]. During this period, various types of 3D displays appeared and were investigated vigorously. To develop a realistic 3D display, the trends of 3D display research was changed from stereoscopic 3D displays to autostereoscopic displays. The first autostereoscopic 3D display was proposed in 1903 by Ives, which was named parallax stereogram and was the basis for the development of modern autostereoscopic 3D displays [3]. The other remarkable invention of autostereoscopic 3D display is integral photography which was proposed by G. Lippmann in 1908, which was based on a two-dimensional (2D) lens array and photographic plate [4]. In 1915 and 1932, the simplified version of integral photography using one-dimensional (1D) lens array was proposed by Hess and Ives, which is lenticular display and a common type in modern autostereoscopic 3D display.

After the embryonic stage of autostereoscopic 3D display, 3D research and industry were waning rapidly until the end of 20th century because of the shoddy quality of 3D image and limitation in manufacturing good quality devices. In the end of 20th century, display market was grown explosively with the development of flat panel devices, which tore down the walls of manufacturing of 3D display gradually. In addition, the development of materials and manufacturing technology facilitates commercialization of 3D displays. In recent years, the 3D display based on stereoscopy with glasses was successfully deployed on a commercial scale for 3D movie theater, theme park, and home television market with the development of flat panel displays and manufacturing technologies [5–7].

Table 1.1 Classification of 3D display

Classification	**Implementation**
Stereoscopy	Polarization glass (Film patterned retarder)
	LC shutter glass
	Head mount display
Autostereoscopy	Parallax barrier
	Lenticular lens
	Slanted lenticular lens
	Integral imaging
	Super multi-view display
	LC shutter
	Holographic optical element
Volumetric display	Spinning screen
	Varifocal mirror
	Crossed-beam
Holographic display	Electro-holography

The present key issues of development in 3D display technology are the question of using or not using glasses and the enhancement of 3D display characteristics. Among various autostereoscopic displays, multi-view display based on the parallax barrier or lenticular lens and integral imaging are almost commercialized techniques. Two methods are based on spatial multiplexing of different view images using barriers or lens array. The major difference of two methods is convergence of viewpoints. However, these methods have some problems such as limited depth cues, resolution limitation and narrow

viewing angle or limited viewpoints. In addition, the number of 3D contents is remarkably low compared to 2D contents. Because of all these problems, integral imaging and multi-view display are not yet commercialized.

Furthermore, 3D television (TV) broadcasting environment is one of the issues in 3D display field. 3D TV broadcasting has been constructed with the development of 3D display and digital broadcasting technology by many research groups, broadcasters and equipment manufacturers in recent years [8–12]. The system architecture of recently commercialized 3D TV broadcasting is composed of capturing stereo images of 3D object or a single image with its depth map, transmitting a 3D contents with compression algorithm and displaying them in a commercialized 3D TV set [9–12]. Although the stereoscopic technique based on 3D TV broadcasting is central to the mainstream technology, autostereoscopic multi-view displays will be developed as the next-generation 3D TV for overcoming the limitation of the number of views and the use of glasses [13–17]. For the compatibility between stereoscopic and multi-view 3D TV broadcasting, the contents format for multi-view display has to keep the stereo images and additional depth map information. In multi-view 3D TV broadcasting, the view synthesis process is needed to generate multi-view images from the stereo images and the depth map information. In the synthesizing process, accuracy and quality of synthesized view image depend on the synthesizing algorithm and the depth resolution of depth map [18–22]. However, the depth map with high depth resolution needs the wide bandwidth in the transmission process, which leads to the high costs of all broadcasting systems. Therefore, the guide lines of human factors and optimized depth resolution are needed in 3D research field.

In addition, 3D optical information acquisition and processing technology has emerged recently as an important issue with the rapid growth of 3D display market and 3D broadcasting [8, 23]. Various methods for 3D image acquisition, analysis and reconstruction have been proposed for more effective and realistic 3D display and broadcasting system. 3D optical information acquisition has shown much advance in technology, from the stereo camera based method with horizontal parallax to the 2D lens array based method with full parallax [9, 10]. Many kinds of 3D optical information processing techniques using integral imaging and light field, such as computational

pickup, depth extraction, 3D object recognition, and 3D image synthesis, were proposed by many research groups [24–38]. However, the accuracy of recognition and precision of extracted depth map are not good for commercialization. Therefore, this dissertation addresses the issues of major autostereoscopic displays which are multi-view display and integral imaging in three different points - display technology, human factor and optical information processing.

1.2 **Motivation of this dissertation**

This dissertation introduces improvement methods for primary types of autostereoscopic 3D displays, multi-view display and integral imaging, in three issues of display technology, human factors and optical information processing. In display technologies, the characteristics of multi-view display and integral imaging have fundamental limitations such as viewing angle limitation, depth limitation, resolution limitation and 2D/3D convertibility.

In integral imaging, various researches to overcome the fundamental limitation have been conducted by many research groups as shown in Table 1.2. Integral imaging (or integral photography), which was invented by Lippmann about 100 years ago [4], is one of the most attractive autostereoscopic 3D displays. Integral imaging can display 3D images using a 2D lens array and a 2D display system that provides elemental images. It has many advantages such as full parallax, quasi-continuous view points, and ability to show moving color images [10, 39–49]. However, integral imaging still has some problems such as limited depth cues, resolution limitation, pseudoscopic problem and narrow viewing angle.

To enhance the viewing angle of integral imaging, the structural and geometrical methods were proposed such as curved structure, embossed screen and switching of polarization barriers [50–53]. For enlargement of expressible depth range in integral imaging, the optical path length or central depth plane of integral imaging was adjusted by using optical elements and the use of focal mode integral imaging or pinhole-type integral imaging was one of the solution [45, 54–56]. To enhance the resolution of integral imaging, the use of rotated prism or multiple elemental image layer with projection scheme was proposed [57, 58]

The integral imaging is also divided into subcategories of pinhole-type integral imaging and lens based integral imaging by the use of lens array or pinhole array to multiplex elemental image [10, 11, 56]. The pinhole-type integral imaging can easily convert 2D/3D mode using light source conversion between point light source and surface light source. In pinhole-type integral imaging, the limitation of 3D display can be improved by grafting the idea of integral imaging and new materials for backlight.

Table 1.2 Improvement methods of integral imaging

Classification	Enhancement	Implementation
Lens array based integral imaging	Viewing angle	Lens switching
		Polarization switching
		Curved lens array
		Eye tracking
	Resolution	Tiled projection scheme
		Multiple elemental image layer
	Depth range	Optical path control
		Multilayered display devices
		Polymer-dispersed liquid crystal layers
	2D/3D convertibility	Concave half mirror array
		Dual depth configuration
Pinhole-type integral imaging	2D/3D convertibility	Pinhole array on a liquid crystal panel
		Optical fiber array
		OLED panel
		Moving pinhole array

This dissertation introduces the improvement methods for each integral imaging and multi-view display and related issues. When the lenticular system and integral photography were proposed, there was no difference between principles of integral photography and multi-view display except the use of 1D lens array or barriers and 2D lens array. However, multi-view display and integral imaging are generally classified in recent years by the convergence of viewpoints as show in Figure 1.1.

On the other hand, multi-view display was proposed by Hess and Ives, which was a simplified methods of integral imaging to 1D parallax display in early days of 3D display research. In recent years, the multi-view display generally refers to autostereoscopic 3D

display using lenticular lens array or parallax barrier. Unlike integral imaging, multi-view display based on lenticular lens or parallax barrier has finite viewpoints and fixed observer distance as shown in Figure 1.1(b).

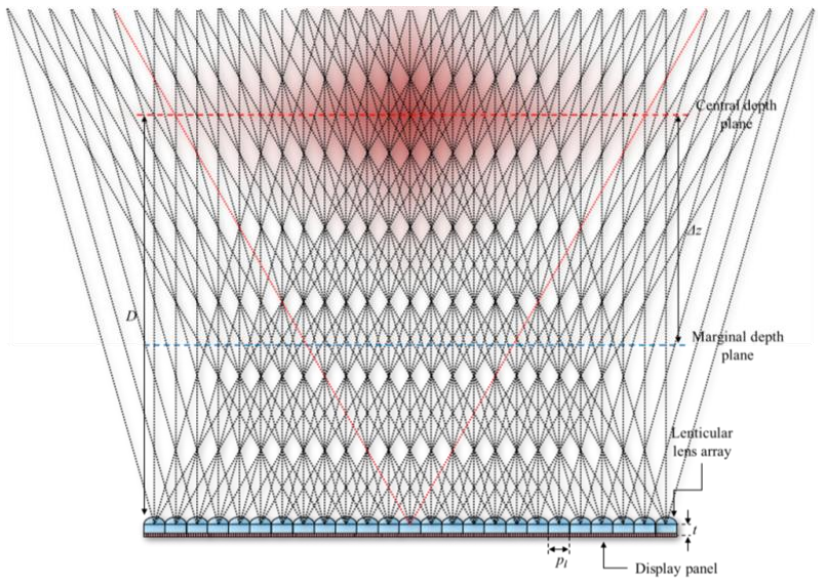

(a)

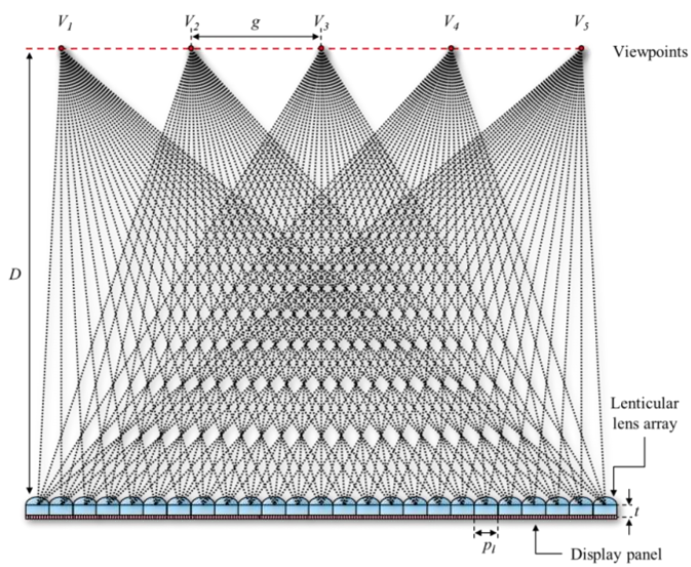

(b)

Figure 1.1 Principles of multi-view display and integral imaging: (a) ray distribution of integral imaging and (b) multi-view display

As shown in Figure 1.1, two methods are composed of same components such as lens array and display panel for elemental image or view images except sampling method of 3D object. From the different sampling methods, two methods have quite different characteristics for 3D images. To reveal the difference of two methods and improve each system, the convergence type of autostereoscopic display will be needed for overcoming limitation of multi-view display and integral imaging.

From these issues of autostereoscopic display technologies, the human factors of observer have to be studied by subjective test and measurement of accommodation response. The study about human factors can give the guideline of autostereoscopic 3D display technologies and broadcasting environments to 3D display manufacturers and broadcasters. With the display technologies and human factor related studies, 3D information process will be the other issues in autostereoscopic display to application field of 3D display.

1.3 **Scope and organization**

This dissertation is focused on three issues of multi-view display and pinhole-type integral imaging in autostereoscopic displays such as display technologies, human factors and information processing as shown in Figure 1.2. This dissertation presents the studies about three issues in autostereoscopic display.

In the issue of display technology, I propose various types of improvement methods in pinhole-type integral imaging and multi-view display to overcome the limitation of autostereoscopic display in Chapter 2 and 3. Chapter 2 presents the improvement methods of pinhole-type integral imaging for 2D/3D convertibility, wide-viewing angle and high resolution of 3D image. For large expressible depth range and 2D/3D convertibility in pinhole-type integral imaging, pinhole-type integral imaging is modified by new light source conversion layer based on the electroluminescent (EL) film. The EL film has the advantage that it can operate continuously even when it is cut or punctured. Using this characteristic, I generate an array of pinholes on an EL film to form a point light source array for reconstructing 3D images based on integral imaging. The EL pinhole film is attached on another EL film and they are electrically controlled to generate a point light source array or a surface light source; hence the system converts 3D and 2D modes.

Taking advantage of the flexibility of EL films, I also propose a flexible 3D/2D convertible integral imaging system with a wide viewing angle using a curved EL film. In addition, I implement a 360-degree viewable cylindrical 3D display system based on integral imaging using the flexibility of EL film.

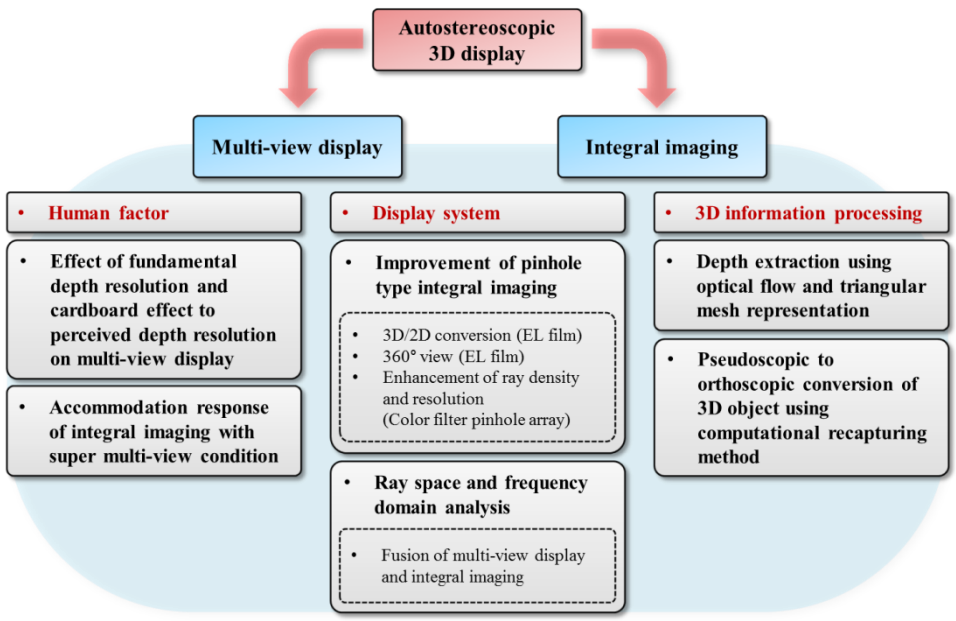

Figure 1.2 Scope of this dissertation

For enhancement of ray density, resolution and expressible depth range in pinhole-type integral imaging, I propose enhancement methods of pinhole-type integral imaging using color filter pinhole array on liquid crystal display panel with projection-type integral imaging scheme. A color filter structure on liquid crystal display panel acts as pinhole array in integral imaging with separation of color channel. In conventional pinhole-type integral imaging, the resolution, viewing angle and ray density are limited by the pinhole interval, the width and thickness of pinhole structure and the gap between display panel and pinhole array. To overcome the limitation of pinhole interval, I use the color filter pinhole array on display panel and the projection-type integral imaging scheme. The use of color filter pinhole array and projection scheme can enlarge the region of one-elemental image and improve the resolution and ray density remarkably. This chapter presents the proposed enhancement methods for pinhole-type integral

imaging and their experimental results.

In Chapter 3, analysis and convergence of multi-view display and 1D integral imaging are presented for improvement of characteristics in autostereoscopic display. In this study, I analyze the multi-view display and integral imaging in light fields and its frequency domain for improvement of each characteristic to convergence type of autostereoscopic display. To compare each display, the principles of display and pickup of each display and analyses of spatio-angular distribution in light fields are presented. In addition of analysis, the issue of pseudoscopic problem in pickup process using integral imaging is solved by using optical flow from sub-images of elemental image. The depth information of sub-images from the acquired elemental image set is extracted using the optical flow with sub-pixel accuracy, which alleviates the depth quantization problem. The extracted depth map is reconstructed and represented to triangular mesh 3D model using triangular mesh representation form sub-images and depth map. From the 3D object reconstruction with sub-pixel accuracy, computational reacquisition for real 3D object in integral imaging is proposed without pseudoscopic problem. The pseudoscopic problem and matching of lens array in pickup and display are fundamental problems for real-time broadcasting based on integral imaging. I propose the reconstruction method of real 3D object and computational reacquisition method without matching of pickup and display lens array.

From the analysis, the convergence type of autostereoscopic 3D display based on multi-view display and 1D integral imaging is proposed by using time-multiplexing technique. The multi-view display and 1D integral imaging use the same optical components except the method of ray sampling. The ray density of multi-view display is non-uniform and focused on each viewpoint, whereas the 1D integral imaging has uniform ray density. To enhance the quality of reconstructed 3D image, the principles of multi-view display and 1D integral imaging are analyzed by quality function and combined using time-multiplexing technique in fast response display panel. This chapter presents the principles, analyses and experimental results of convergence type of autostereoscopic 3D display.

In the issue of human factor, Chapter 4 presents the studies about the depth resolution and accommodation response of human factors in multi-view display and

integral imaging. To find the effect of fundamental depth resolution and cardboard effect to the perceived depth resolution in multi-view display, I analyze the fundamental depth resolution and the cardboard effect from the synthesis process in the multi-view 3D TV broadcasting. After the analysis, the numerical comparison and subjective tests with 20 participants are performed to find the effect of fundamental depth resolution and the cardboard effect to the perceived depth resolution.

In addition, the analysis and measurement of accommodation response of integral imaging with satisfying super multi-view (SMV) display is performed to reveal the relation between the accommodation response of integral imaging and SMV condition. I analyze viewing region satisfying SMV condition in integral imaging and evaluate the accommodation response when the observer is located inside and outside of the SMV region in integral imaging. To reveal the relation between the SMV condition and accommodation response of integral imaging, I perform the numerical analysis with SMV condition in integral imaging and present the experimental results of accommodation response using autorefractometer.

Chapter 2

Enhancement of pinhole-type integral imaging using electroluminescent film and color filters on display panel

2.1 Integral imaging system using an electroluminescent film backlight for three-dimensional/two-dimensional convertibility and a curved structure

I propose a thin and compact integral imaging system using electroluminescent (EL) films as backlight. The EL film has the advantage that it can operate continuously even when it is cut or punctured. Using this characteristic, I generate an array of pinholes on an EL film to form a point light source array for reconstructing 3D images based on integral imaging. The EL pinhole film is attached on another EL film and they are electrically controlled to generate a point light source array or a surface light source; hence the system converts between three-dimensional (3D) and two-dimensional (2D) modes. Taking advantage of the flexibility of EL films, I also propose a flexible 3D/2D convertible integral imaging system with a wide viewing angle using a curved EL film. I explain the principle of the proposed methods and present experimental results.

2.1.1 Introduction

The 3D display, which shows various views of an object, is thought of as the ultimate

form of display. In recent years, due to the development of the display technique, many kinds of 3D displays were proposed [59]. Among them, integral imaging (or integral photography), which was invented by Lippmann more than 100 years ago [4], is one of the most attractive methods. Integral imaging can display 3D images using a 2D lens array and a 2D display system that provides elemental images. It has many advantages such as full parallax, quasi-continuous view points, and ability to show moving color images [10, 39–49]. However, integral imaging still has some problems such as limited depth cues, resolution limitation, pseudoscopic problem and narrow viewing angle. Also, the number of 3D contents is remarkably low compared to 2D contents. Because of all these problems, integral imaging is not yet commercialized, and it needs a complementary type of display. This situation has instigated the research on 3D/2D convertible integral imaging system.

Several methods of 3D/2D convertible integral imaging system were devised [56, 60–65]. The main idea in most of these systems is a light source converting layer (LCL), which is a convertible light source that can be either surface light source or point light source array as shown in Figure 2.1. This system operates in two modes, point light source array mode for 3D image and surface light source mode for 2D image. In 3D mode, the system shows 3D image to observer by displaying elemental images on transmission-type display panel when LCL is operated in the point light source mode. In the other mode, observer can see 2D images using the surface light source mode of LCL.

The attention of research on 3D/2D convertible integral imaging system has been paid to the method generating more efficient LCL. Many methods for convertible light source were proposed [56, 60–65]. For examples, polymer-dispersed liquid crystal (PDLC), pinhole array on a polarizer (PAP), and organic light-emitting diode (OLED) panel were fabricated to LCL. These systems might be suitable for cellular phones or other mobile devices because they have small system size and simple structure.

However, each of them has some disadvantages. The method using PDLC has complex structure and the gap between lens array and display panel should be adjusted precisely to twice the focal length of lens array [56]. In another method using PAP, although it has a thin structure and is a simple method, its brightness of 3D image is degraded by using polarizer [61]. The latest proposed method used OLED panel for

LCL [64]. This method also has a simple structure and thin thickness. Nevertheless, an OLED panel with the high resolution and small pixel size is expensive and difficult to produce. In addition, it has color separation problem because of separated red/green/blue pixels of OLED panel.

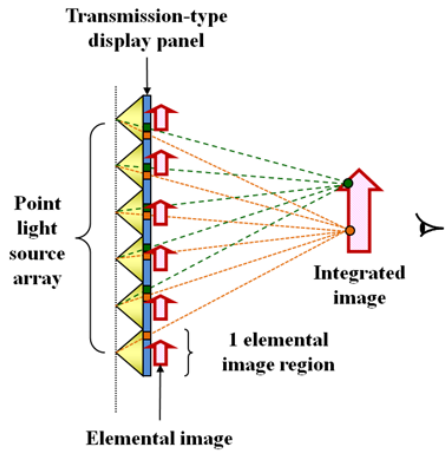

(a)

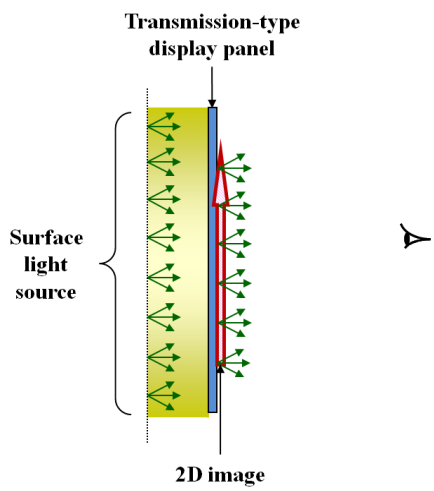

(b)

Figure 2.1 Concept of the 3D/2D convertible integral imaging system: (a) 3D mode and (b) 2D mode

To solve these disadvantages in conventional methods, I propose an electroluminescent (EL) film LCL using EL film and EL pinhole film in this study. The

use of EL film LCL in 3D/2D convertible integral imaging system makes reduction of the system thickness and operation voltage possible, while keeping simple structure. Moreover, the characteristics of EL film LCL can improve conventional integral imaging system. In 3D/2D convertible integral imaging, I propose selectively convertible system using multi-domain EL film LCL by segmented EL pinhole film. It enhances the image expression because it can display 3D and 2D images at once. Using flexibility of EL film LCL, I also implement viewing-angle-enhanced curved integral imaging system. This system has a potential of flexible 3D/2D convertible integral imaging system if a flexible transmission-type spatial light modulator (SLM) could be used together with this backlight unit (BLU).

2.1.2 **Principles of 3D/2D convertible integral imaging using EL film**

2.1.2.1 **Light source converting layer using EL films**

In this study, I use EL films to improve the recent researches on 3D/2D convertible integral imaging system. The EL film is a self-light-emitting device using electroluminescence which is non-thermal generation of light resulting from the application of an electric field to a substance [66]. The EL film has many kinds of structures such as AC thin-film type, AC powder type, DC thin-film type, and DC powder type. They have advantages such as thin structure, low power consumption, less heating problem, and low-cost. Among many kinds of EL films, powder type EL films only have the important advantage which can operate continuously, even when it is cut or punctured. I use the AC powder type EL film to fabricate the EL pinhole film because DC powder type is not developed yet.

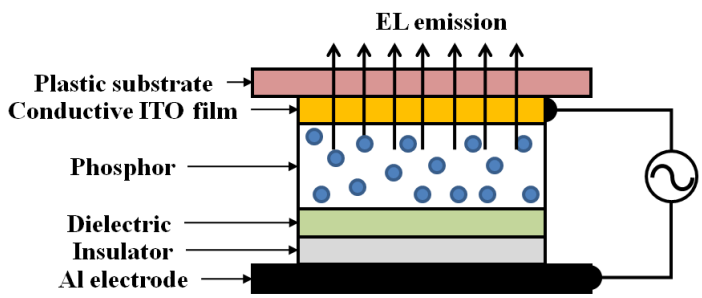

Figure 2.2 The structure of AC powder type EL film

The AC powder type EL film is used as a BLU of liquid crystal display (LCD). It relies on phosphorescent powder materials which glow when exposed to small electrical currents. As shown in Figure 2.2, the source of light is a phosphorous mixture powder which is spread onto a transparent conductive indium tin oxide (ITO) film and then covered with another thin film of conductive material. The phosphor layer consists of a suitably doped zinc sulfide (ZnS) powder suspended in a dielectric, which acts as a binder as well. The phosphor layer is sandwiched between two electrodes, one is transparent, and the other is supported by a substrate, which is a flexible plastic. In AC powder type EL film, it has important advantage that it can emit the light, even when it is cut or punctured because the phosphorescent layer consists of powder materials and other layers have flexibility. Since phosphorescent layer consists of powder materials and substrates are flexible, it has flexibility and can emit light even when it is cut or punctured. I take advantage of these features in this research. I use two kinds of EL film, one punctured in the shape of pinhole array and the other without puncturing. I call the former EL pinhole film and the latter EL film. The EL film LCL is created by stacking the EL pinhole film on the EL film. The EL film LCL can change between two light source modes by switching the EL pinhole film. In point light source array mode, EL pinhole film acts like a pinhole film (by cutting off electrical currents) while EL film shines behind the EL pinhole film. The rays from EL film are blocked by EL pinhole film except the pinhole area. Hence, these pinhole areas act like point light source array for generating 3D image based on integral imaging. In surface light source mode, EL film and EL pinhole film are both switched on to produce a surface light source with uniform intensity. In consequence, a thin and compact LCL can be realized using EL film and EL pinhole film.

The above-mentioned EL film LCL can evolve to selectively convertible EL film LCL that generates a light source in which certain area becomes point light source array and the other area becomes surface light source at once by segmenting EL film LCL to multiple domains. As shown in Figure 2.3, the EL pinhole film in EL film LCL can be segmented to multi-domain of controllable pinholes. In this situation, pinhole domains can be independently controlled by switching each electrical current. Using two-domain EL film LCL, it can be operated in point light source array mode, surface light source mode, and additional selective light source generation mode where one of the pinhole

domains generates point light source array and the other domain generates the surface light source. The selective light source generation mode is adopted to 3D/2D convertible integral imaging system and it can be possible to reconstruct 3D and 2D images at once, which is called mixed 3D/2D mode or partial 3D mode.

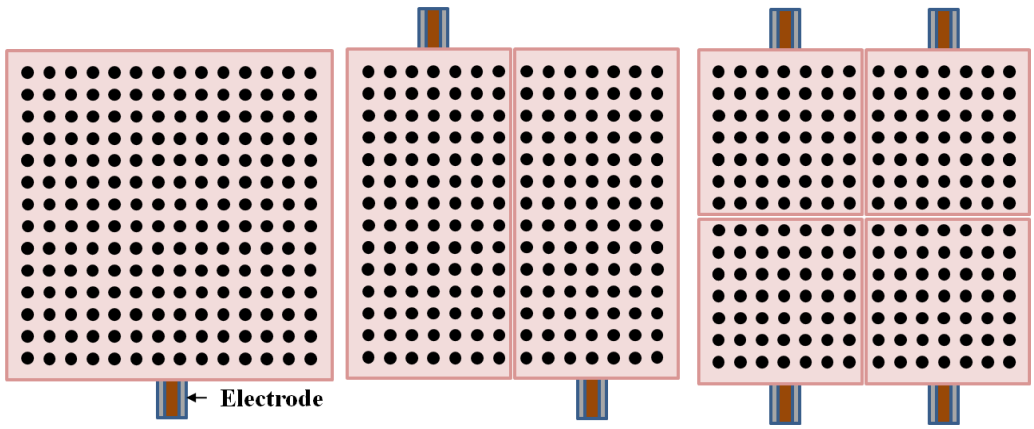

(a) (b) (c)

Figure 2.3 The multi-domain EL film LCL: (a) one-domain, (b) two-domain, (c) four-domain structures

2.1.2.2 **A 3D/2D convertible integral imaging system using EL film LCL**

The overall structure of the proposed 3D/2D convertible integral imaging system using EL film LCL is shown in Figure 2.4. In the proposed method, I only use EL film LCL and transmission-type display panel. A use of EL film LCL provides many improvements to the previous methods. EL film LCL can reduce the system thickness because the thickness of commercial AC powder type EL film is about 400 ㎛. The system structure is also simplified. EL film LCL has advantages of low power consumption, less heat problem, and low-cost. Above all, it has flexibility. Due to the virtue of the characteristic of AC powder type EL film, 3D/2D convertible integral imaging system using EL film LCL has same advantages.

In the principle of the proposed method, 3D/2D convertible integral imaging system operates in two modes. EL pinhole film and EL film in the EL film LCL should be synchronized with the displayed image on transmission-type display panel.

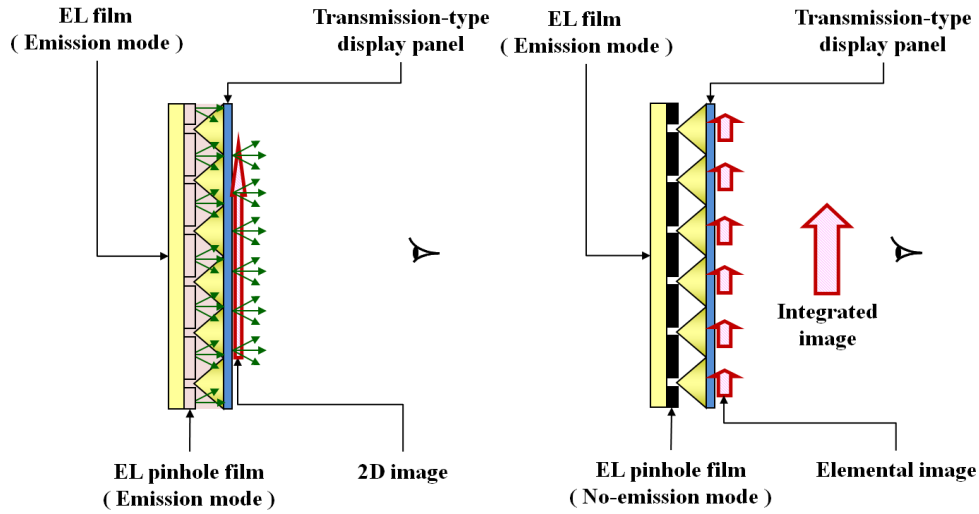

Figure 2.4 Principle of the 3D/2D convertible integral imaging system using EL film LCL: (a) 3D mode, (b) 2D mode

In the 3D mode, the EL film LCL generates a point light source array by turning EL film on and EL pinhole film off while transmission-type display panel shows the elemental image for 3D image. The resolution of 3D mode in the proposed method is proportional to the number of point light sources when the size of each point light source and the pixel pitch of the transmission-type display panel are ideally small [63]. However, the pixel pitch of transmission-type display panel has some non-zero size in real experiments, and the resolution of the 3D image is influenced by the pixel pitch because the rays are modulated by the transmission-type display panel. When the pixel pitch of the transmission type display panel is small, the resolution of the 3D image is improved because the light rays are modulated more finely. In the 2D mode, EL film and EL pinhole film in the EL film LCL both emit the light, and the observer can see the 2D image on transmission-type display panel with its full resolution.

To evolve the proposed method, a multi-domain EL film LCL can be applied to the system. By selectively converting the mode of each domain, 3D image and 2D image can be implemented simultaneously. The 3D/2D selectively convertible integral imaging system using multi-domain EL film LCL is shown in Figure 2.5. If the number of EL film domains is increased by more segmenting the EL pinhole film, the selective

reconstruction area will be broadened.

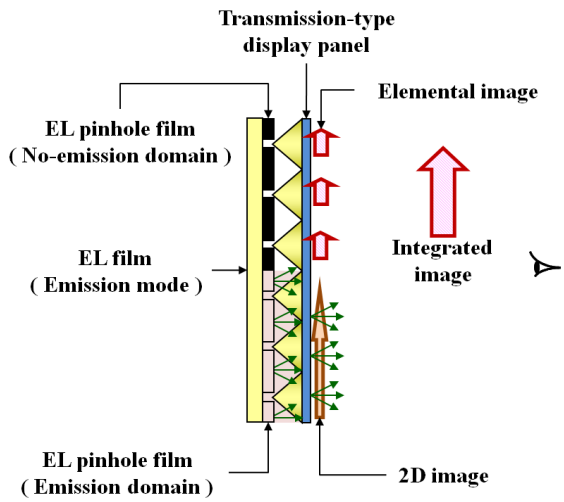

Figure 2.5 Concept of the 3D/2D selectively convertible integral imaging system using multi-domain EL film LCL

2.1.2.3 **A flexible integral imaging system using EL film LCL**

The most important advantage of EL film is that it is a flexible self-light-emitting device. This advantage allows integral imaging to improve its viewing angle by using curved structure. The previously reported curved structure uses the lens array arranged in curved plane to enhance viewing angle [50, 52, 67]. However, in these systems, it is hard to make the curved lens array and 3D/2D conversion is impossible. To solve the problems, I propose the flexible 3D/2D convertible integral imaging system with wide viewing angle using curved EL film LCL. Making curved structure using EL film LCL is easier than using lens array because of EL film's flexibility. In addition, a use of EL film LCL enables the system to evolve to the 3D/2D convertible display system. Using this improved performance of integral imaging, the curved structure with transmission-type flexible display panel might be adopted to various 3D display applications such as 3D television, 3D theater and 3D signboard with wide-viewing angle. Above all applications, the proposed method is suitable to mobile 3D display because of its flexibility and 3D/2D convertibility.

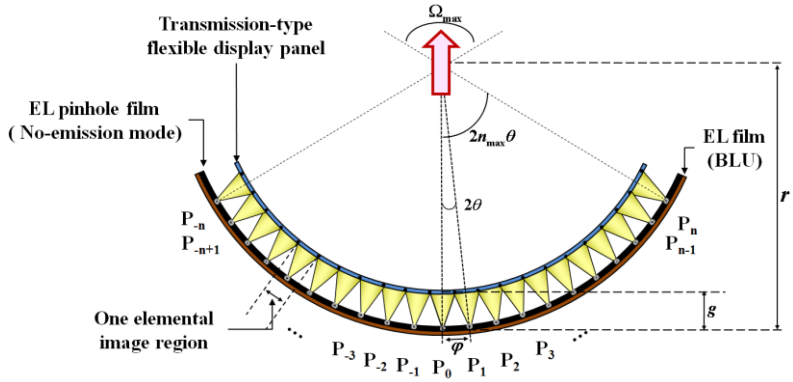

(a)

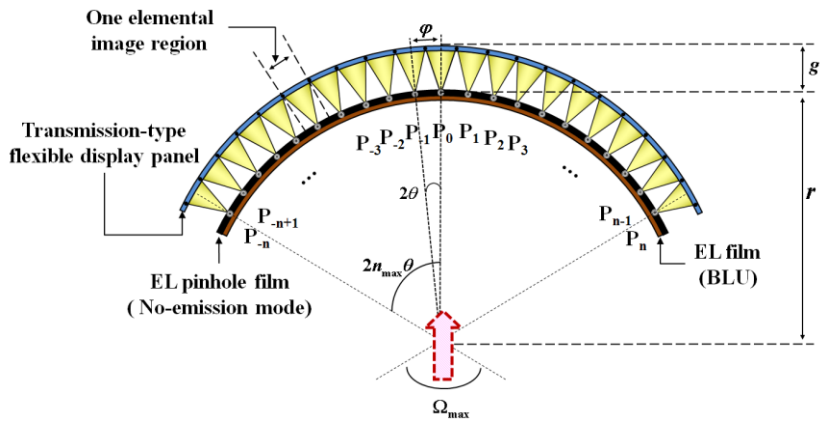

(b)

Figure 2.6 Configuration of the flexible 3D/2D convertible integral imaging system with wide viewing angle using curved EL film LCL: (a) real mode, (b) virtual mode

Figure 2.6 shows the configuration of the flexible 3D/2D convertible integral imaging system with wide viewing angle using curved EL film LCL. The system has two types of structure for displaying real or virtual 3D image as shown in Figure 2.6(a) and (b). The EL film LCL is curved with a radius of curvature *r*, and it is located behind the transmission-type flexible display panel at a distance of gap *g*. In the point light source array mode of LCL, the transmission-type flexible display panel displays elemental images for curved pinhole array, and rays from the point light sources pass through each elemental image region of the transmission-type flexible display panel. A 3D object is integrated and shown in front of observer with an enhanced viewing angle. On the other

hand, 2D images on the transmission-type flexible display panel are displayed in the surface light source mode LCL.

2.1.2.4 **Analysis on the viewing angle of the flexible 3D/2D convertible integral imaging system**

For a more detailed principle of the proposed method, the maximum number of pinholes in one direction n_{max} is determined in consideration of radius of curvature r, pinhole interval φ, and gap g. In Figure 2.6(a), curved EL film LCL generates $2n_{max}+1$ point light sources in an array on curved plane, and each point light source reconstructs 3D image around the central point of a curved structure with maximum viewing angle Ω_{max}. The maximum viewing angle Ω_{max} can be derived as follows,

$$\Omega_{\max} = 2 \times 2n_{\max}\theta = 4n_{\max} \arctan\left(\frac{\varphi}{2r}\right). \tag{2.1}$$

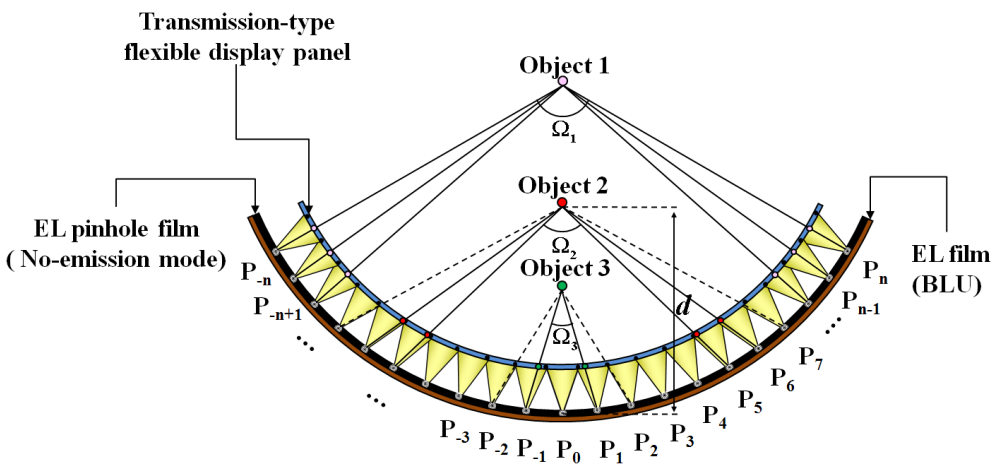

Figure 2.7 Viewing angles depending on object locations in the proposed system

The maximum viewing angle is achieved in the situation when integrated 3D image is located around the central point of the curve. For the more detailed analysis of viewing angle in more general cases, the consideration about distance from integrated 3D image to pinhole array is needed. In Figure 2.7, objects 1, 2, and 3 are integrated on positions off the central point. In the case of object 1, 3D image is located at the nearest position among the three to the central point, and all elemental image regions are used to integrate

3D image without intrusion of rays into the neighbor elemental image regions; the observer sees it with the widest viewing angle Ω_1. As decreasing the distance from the object to the middle pinhole of pinhole array P_0, some rays pass through adjacent elemental image regions which correspond to other pinholes and cause the flipped image problem. In the case of object 2, the ray from P_6 to object 2 passes its own elemental image region correctly, but the ray from P_7 intrudes into the elemental image region of P_6, so the maximum number of pinholes in one direction, n, is 6. Likewise, n is 1 in the case of object 1, which has the narrowest viewing angle. This condition can be expressed as follows,

$$\frac{(r-g)\sin(2n+1)\theta}{(r-g)\cos(2n+1)\theta-(r-d)} \geq \frac{r\sin(2n\theta)}{r\cos(2n\theta)-(r-d)}, \tag{2.2}$$

where d is 3D image distance from P_0. The maximum number of pinholes in one direction is the highest value of n satisfying Eq. (2.2). With n acquired from the above condition, the maximum viewing angle, Ω_n can be derived as follows,

$$\Omega_n = 2\arctan\left\{\frac{r\sin(2n\theta)}{r\cos(2n\theta)-(r-d)}\right\}. \tag{2.3}$$

If the curved structure is for virtual 3D image as shown in Figure 2.6(b), Eqs. (2.2) and (2.3) are derived as follows:

$$\frac{(r+g)\sin(2n+1)\theta}{(r+g)\cos(2n+1)\theta-(r+g-d)} \geq \frac{r\sin(2n\theta)}{r\cos(2n\theta)-(r+g-d)}, \tag{2.4}$$

$$\Omega_n = 2\arctan\left\{\frac{r\sin(2n\theta)}{r\cos(2n\theta)-(r+g-d)}\right\}. \tag{2.5}$$

Figure 2.8 shows viewing angle versus image distance for different gaps using Eq. (2.3) when the EL film LCL's radius of curvature r is set to 80 mm, and the pinhole interval φ is 1 mm. As shown in Figure 2.8, the maximum viewing angle is 180 degrees when integrated 3D image is located near the central point of curve. However, it decreases rapidly as integrated 3D image goes far from the central point. The distribution

of viewing angle is calculated with various gaps between the EL film LCL and transmission-type flexible display panel as shown in Figure 2.8. When the gap becomes wider, the viewing angle changes rapidly while the image distance increases. The viewing angle can be enhanced as the gap becomes narrower, or as the position of integrated 3D image approaches the central point.

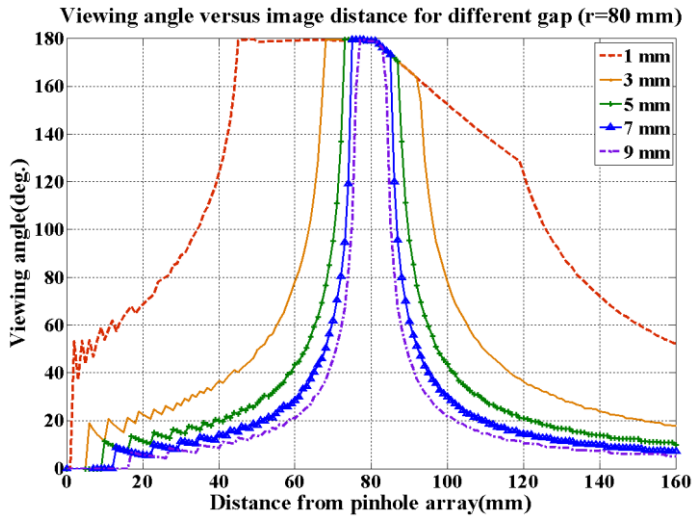

Figure 2.8 Viewing angle versus image distance for different gaps in the proposed system

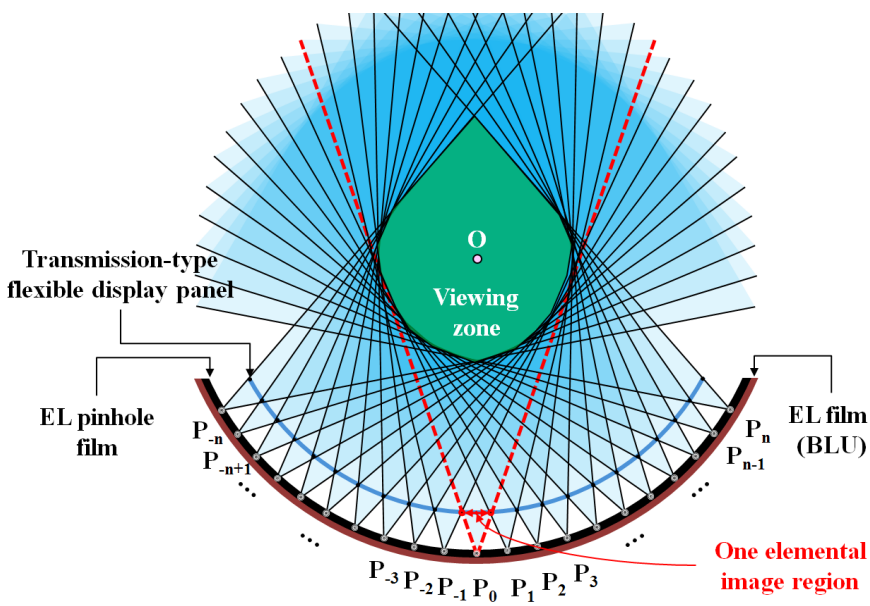

Figure 2.9 The viewing zone limitation in the proposed system

From viewing angle analysis, the viewing zone, which is the feasible region where integrated 3D image can be shown with a wide viewing angle, is limited around the central point O in Figure 2.9. As shown in the figure, the integrated 3D image in the viewing zone can be shown to observer with the widest viewing angle.

The viewing zone is limited by the intensity of point light source array. Although 3D image in the viewing zone has the widest viewing angle, the observer cannot see it exactly when the radius of curvature is sufficiently large because the intensity of a point light source is proportional to the inverse-square of distance. Moreover, the rays from one point light source can diverge to all directions, so they intrude neighbor elemental image regions and induce the flipped image. In consequence, 3D image can be seen with wide viewing angle and clearness when it is located at the nearest position from pinhole array in the viewing zone with barrier.

2.1.3 **Experimental results**

I performed experiments to verify the feasibility of the proposed methods. In this section, I present two experimental results; one shows the 3D/2D convertible integral imaging system using EL film LCL and the other shows the flexible 3D/2D convertible integral imaging system with wide viewing angle using curved EL film LCL. For the experiments, EL film LCL which is the main component of proposed method is composed of commercial AC powder type EL films. For EL film LCL in the 3D/2D convertible integral imaging system, I used commercial AC powder type EL film that has 50 mm × 50 mm in size and 400 μm in thickness. The EL pinhole film is fabricated by using a drilling machine to have 40 × 40 pinholes whose diameter is 200 μm and separation of 1 mm between neighboring pinholes. For multi-domain EL film LCL, I cut the one domain EL pinhole film to two domains. Each domain has 20 × 40 pinholes. For the other proposed method, I used 170 mm × 70 mm size EL film and generated 150 × 50 pinholes on it with the same pinhole specification. The EL film and EL pinhole film are operated by AC voltage of 110 V, 400 Hz that is generated by the inverter using input voltage of DC 3 V.

As shown in Figure 2.10, EL film LCL is composed of two-domain EL pinhole film and EL film. The luminance of EL film LCL is 150 cd/m^2 in surface light source mode

and 100 cd/m^2 in point light source array mode. With the control of each domain of EL pinhole film, the selective light source generation mode is possible and light source is converted partially.

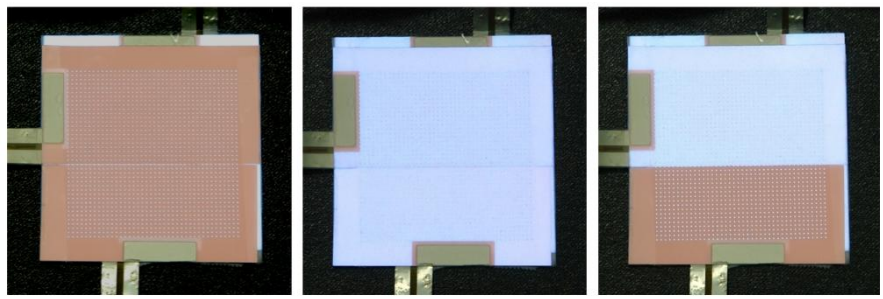

(a) (b) (c)

Figure 2.10 The light source conversion of two-domain EL film LCL: (a) surface light source mode, (b) point light source array mode, (c) selective light source generation mode

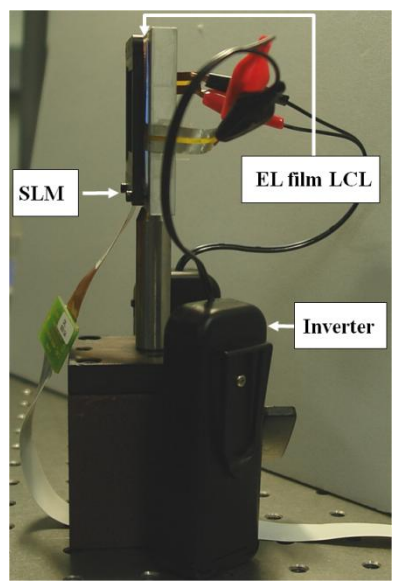

Figure 2.11 Experimental setup of 3D/2D convertible integral imaging system using EL film LCL

I built up the proposed 3D/2D convertible integral imaging system using EL film LCL, as shown in Figure 2.11. The experimental setup consists of two-domain EL film LCL and transmission-type display panel. As a transmission-type display panel, I used an

SLM that has a 36 μm pixel pitch in the horizontal and vertical directions with 37 mm × 28 mm active area and resolution of XGA (1024 × 768). The thickness of the SLM is 360 μm. The total thickness of the proposed system is about 2.8 mm, including thickness of EL film LCL, the gap between EL film LCL and SLM, and the thickness of SLM. With this specification, EL film enables a thin and compact 3D/2D convertible integral imaging system.

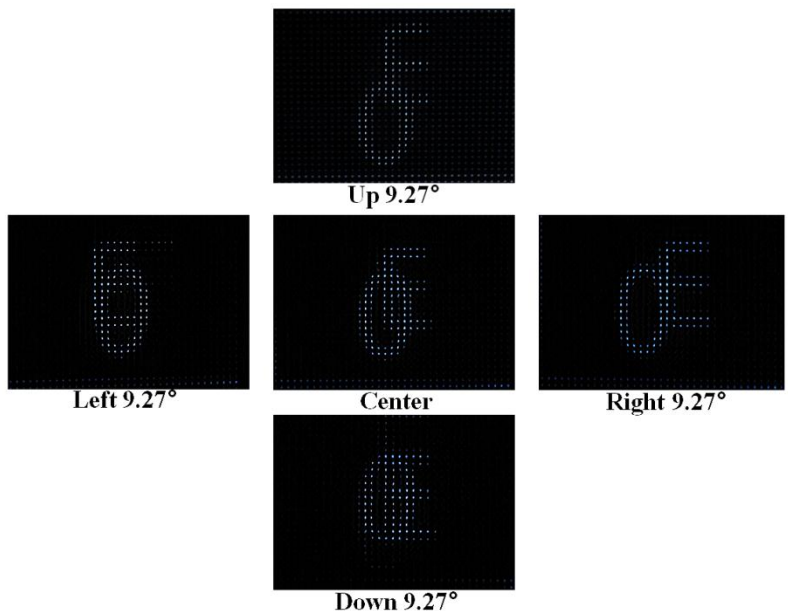

Figure 2.12 Experimental results: 3D images observed from different viewing directions

In the 3D mode, I used the computer generated elemental image for reconstructing 3D image. The integral imaging has the pseudoscopic problem, which is the fundamental problem in real pick up of integral imaging, and it needs the pseudoscopic-to-orthoscopic conversion [24, 26]. In this study, I used computer generated elemental images for avoiding pseudoscopic problem [68]. The computer generated elemental image enables the image of two letters ‘O’ and ‘E’ to form at 20 mm in front of and behind the point light source array. The experimental results in 3D mode are shown in Figure 2.12. The directional rays are generated from the point light source array in the diverging angle passing through pixels of the SLM in front of EL pinhole film and form the 3D image of two letters. I can see different perspectives from different viewing positions as shown in Figure 2.12. The viewing angle is approximately 18.54 degrees in the experiment. In this

experiment, I see the discontinuity of integrated image and image degradation at the brim of image. That is the multifacet effect which is caused by inappropriate overlapping of elemental image in field of view of each pinhole. This is a fundamental problem of pinhole array structure [69]. The multifacet effect can be reduced by use of the moving pinhole array technique [70].

In the 2D mode, EL film LCL generates the surface light source because I provide electrical currents to the EL pinhole film. The SLM displays the 2D image, a sea turtle, with full resolution of XGA on it as shown in Fig. 13. As shown in Figure 2.13(a), a problem is the difference of brightness of the EL pinhole film and the rays which pass through pinhole array from the EL film. To solve this uneven brightness problem, I increase the voltage of the EL pinhole film and adjust it to the suitable voltage to emit the light of same brightness. In the experiment, I adjust the output voltage of the inverter from 123.5 V to 128.5 V. I can see 2D image clearly as shown in Figure 2.13(b).

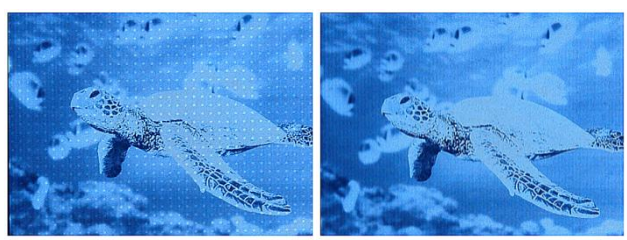

(a) (b)

Figure 2.13 Experimental results in 2D mode: (a) before the brightness adjustment, (b) after the brightness adjustment

Figure 2.14 Experimental result in 3D/2D selectively convertible mode

In addition to 3D and 2D modes, the 3D/2D selectively convertible mode in 3D/2D convertible integral imaging system is experimented by using the two-domain EL film LCL. 3D and 2D images can be displayed at once by controlling each domain as shown in Figure 2.14.

I also experimented the other proposed method, which is the flexible 3D/2D convertible integral imaging system with wide viewing angle using a curved EL film LCL. The proposed system consists of EL film LCL and transmission-type flexible display panel. However, transmission-type flexible display panel is not developed and commercialized yet. Hence I used an overhead projector (OHP) film and printed elemental images on it using a laser printer. The printed elemental image resolution is 1200 DPI. In this situation, although OHP film cannot display moving image and change the elemental image, it can verify possibility of the proposed method. The actual experimental setup is shown in Figure 2.15. It simply consists of curved EL film LCL, OHP film, and transparent-curved-acryl structure. The transparent-curved-acryl structure maintains a correct gap between curved EL film LCL and OHP film, and sustain whole system structure. I also used a barrier array for preventing flipped 3D image and enhancing the brightness of the 3D image. I experimented two different types of curved structure for displaying real and virtual 3D image as shown in Figure 2.15 (a) and (b).

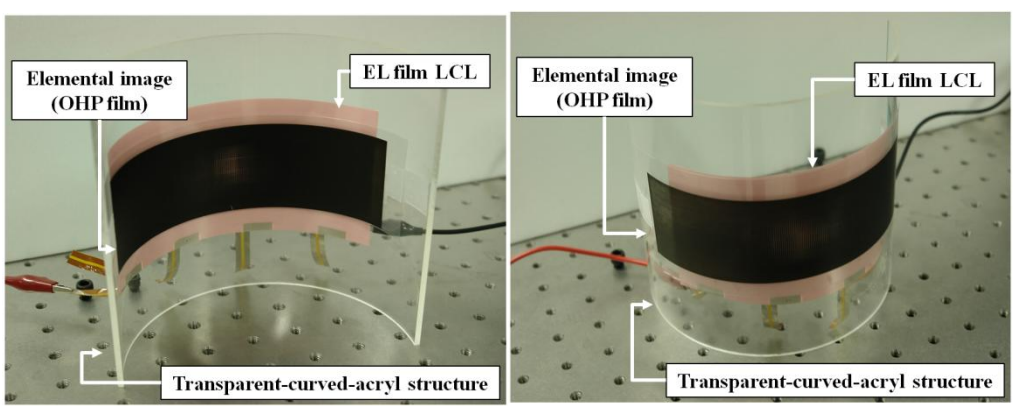

(a) (b)

Figure 2.15 Experimental setup of the flexible 3D/2D convertible integral imaging system with wide viewing angle using curved EL film LCL: (a) real 3D mode, (b) virtual 3D mode

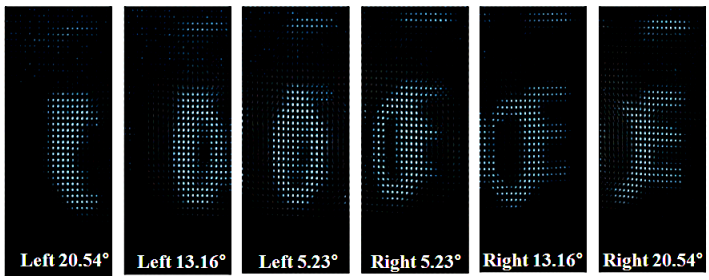

(a)

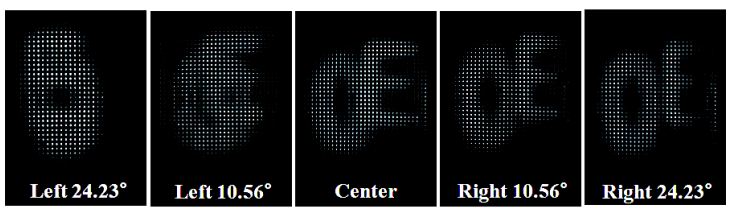

(b)

(c)

Figure 2.16 Experimental results of the flexible 3D/2D convertible integral imaging system with wide viewing angle using curved EL film LCL: (a) real 3D mode, (b) virtual 3D mode, (c) 2D mode

The elemental image for the proposed method on OHP film is generated by ray tracing calculation using computer generated integral imaging. It reconstructed two 3D images – two letters ‘O’ and ‘E’ at two different positions, 60 mm and 40 mm. As shown in Figure 2.16(a) and (b), the results show a remarkable enhancement of viewing angle in the proposed method. The viewing angle of the proposed curved pinhole system is about

48.46 degrees in real 3D mode and 41.08 degrees in virtual 3D mode. The viewing angle of the conventional method is about 18.54 degrees; so the enhancement of viewing angle in the proposed method is certainly verified. In addition to the viewing-angle-enhancement, the proposed method can convert display modes between 3D and 2D using EL film LCL. As shown in Figure 2.16(c), 2D image on OHP film is shown by observer clearly.

2.1.4 **Conclusion**

In conclusion, I proposed a thin and compact EL film LCL. EL film LCL has the advantage such as thin thickness, compact structure, low power consumption, less heating problem, low-cost, and flexibility. In this study, I proposed two types of integral imaging system using EL film LCL. One is 3D/2D selectively convertible integral imaging system. By using multi-domain EL film LCL, 3D and 2D images are displayed at once. Because of the use of EL film LCL, the proposed system is thinner and more compact than other systems of recent researches. The other proposed method is the flexible 3D/2D convertible integral imaging system with wide viewing angle using curved EL film LCL. It is originated by the flexibility of EL film LCL. Even though the transmission-type flexible display panel is not commercialized yet, this method shows the feasibility of a simple and thin flexible 3D/2D convertible integral imaging system with a wide viewing angle. Due to thin thickness, low power consumption and flexibility of EL film LCL, I expect my proposed methods to have applications in mobile displays, cellular phones or other portable displays.

2.2 360°-viewable cylindrical integral imaging system using a three-dimensional–two-dimensional switchable and flexible backlight

I implement a 360-degree viewable cylindrical 3D display system based on integral imaging. The proposed system is composed of a cylindrically arranged EL pinhole film, an EL film backlight, a barrier structure, and a transmission-type flexible display panel. The cylindrically arranged point light source array which is generated by the EL pinhole film reconstructs 360-degree viewable virtual 3D images at the center of the cylinder. In addition, the proposed system gives the 3D/2D convertibility using the switching of EL pinhole film from point light source to surface light source. In this study, the principle of operation, analysis of the viewing parameters, and the experimental results are presented.

2.2.1 Introduction

The 3D display technology has emerged recently as a new paradigm for visual display market, and received much attention as a next-generation display technology. Many types of 3D display technologies have been developed and are announced [5, 6, 59, 71, 72]. Among them, the 3D display based on stereoscopy with glasses is successfully deployed on a commercial scale for 3D movie theater, theme park, and home television market [5–7]. The key issues of development in 3D display technology are the question of using or not using glasses and the enhancement of 3D display characteristics. Therefore, the 3D display market will be evolved from stereoscopic display to autostereoscopic display with wide viewing angle and high resolution, and 3D volumetric display at the end. The 360-degree viewable volumetric 3D display will be the final form of display and the most ideal type in the development of display technology. Observing the reconstructed 3D image in 360-degrees, the observer would feel more realistic.

Frontier groups and companies are performing researches on wide viewing angle 3D volumetric display technologies. The widely-used volumetric 3D display technique is based on the spinning screen system [73, 74]. The spinning screen type volumetric 3D display can reconstruct the 3D object at the center of the volume and the observer can see

it whole around the system. However, the system is very complicated because of the use of the motorized spinning screen and synchronized system with digital micromirror device. Therefore, the system needs huge size and high cost, and involves a safety problem from the rotating screen.

In this study, I propose the 360-degree viewable 3D display system based on integral imaging to overcome the disadvantage of the spinning screen based volumetric 3D display system. Integral imaging is a 3D display implementation method which was firstly proposed by Lippmann in 1908 [4], and it is composed of a 2D display panel and lens array which is a set of elemental lenses. Integral imaging can show the reconstructed 3D image to the observer without any special viewing-aids. Using 2D lens array, integral imaging can provide the reconstructed 3D image with full-parallax and motion color image with quasi-continuous viewing points in simple scheme. However, it also suffers from the issues of insufficient depth, resolution, and viewing angle problems. Some techniques to overcome its weakness have been proposed by many groups [10, 28, 35, 39, 42, 44, 45, 53].

Among them, the curved lens array based integral imaging is one of the viewing angle enhancement methods; it enhances the viewing angle of integral imaging by arranging the lens array in a curve [50]. The modified integral imaging is another enhancement method of integral imaging, which uses a pinhole array instead of lens array [56]. The use of pinhole array gives the simple structure and a 3D/2D convertibility which is implemented by switching the backlight from surface light source to point light source for integral imaging. The most recently proposed method for 3D/2D convertible integral imaging is the EL pinhole film based method which is generated by the pinhole array on the EL film in front of another EL film that is used as backlight [75]. The system can convert light source from a surface to point array by switching the EL pinhole film. In addition, the EL film-based integral imaging system is modified to a curved pinhole array system for viewing angle enhancement using the flexibility of the EL film.

In this study, I propose the simplest method for 360-degree viewable 3D display with full-parallax using the above-mentioned curved structure and EL pinhole film based integral imaging. Figure 2.17 is the concept of the 360-degree viewable cylindrical integral imaging system using 3D/2D switchable and flexible backlight. As shown in

Figure 2.17, I used two EL films for generating point light source array in a cylindrical shape using their flexibility. Also, the 3D/2D convertibility is obtained by using the EL pinhole film backlight switching. In the proposed system, each point light source is arranged cylindrically instead of flatly. The cylindrical arrangement of point light source array enhances the viewing region to 360-degrees when the reconstructed virtual 3D image is displayed at the center of the cylinder structure. For preventing flipping problem, I implement the barrier structure in each point light source when the transmission-type flexible display panel shows the elemental image. Using this method, 3D display for many viewers, 3D signboard, and 3D information display might be easily made in a simple structure.

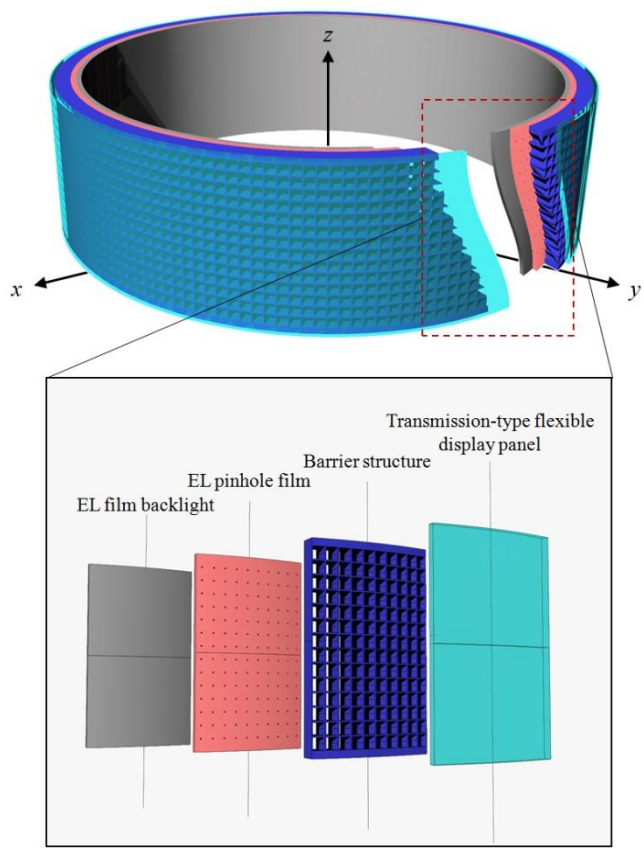

Figure 2.17 The concept and the layer structure of the 360-degree viewable cylindrical integral imaging system

To begin with, I explain the fundamental principles of proposed system and show how the 3D/2D convertibility is realized in my system. In Section 2.2.3, I analyze the characteristic parameters of the proposed system and viewing zone where the reconstructed virtual 3D image can be seen without flipping. In Section 2.2.4, I present the experimental setup and results of the proposed system.

2.2.2 Principles of the 360-degree viewable cylindrical integral imaging system

The 3D display principle of the proposed system is based on the modified integral imaging which is based on the point light source array instead of lens array. For 3D/2D convertibility and viewing angle enhancement to 360-degrees, I propose the cylindrically arranged layer structure as shown in Figure 2.17. The proposed system is composed of transmission-type flexible display panel, barrier structure, and cylindrically arranged point light source array. For generating cylindrically arranged point light source array, I stacked the EL pinhole film and EL film backlight without any gap in cylindrical structure. The barrier structure is located in front of the cylindrically arranged point light source array for preventing the flipped image and keeping the gap between point light source array and elemental image. The outermost layer is the transmission-type flexible display panel which displays the elemental image in cylindrical shape using its flexibility.

The proposed system reconstructs the virtual 3D image at the center of the cylinder while each ray from cylindrically arranged point light source passes through elemental image which is bound by the barrier structure. The more detailed 3D display principle of the proposed system is shown in Figure 2.18 and Figure 2.19. The cross section of the proposed system in *yz* plane shows the 3D display principle in vertical parallax as shown in Figure 2.18. The point light source array is generated by the EL film backlight and EL pinhole film which is in non-emitting mode and acts like the pinhole array. In this situation, the cross section structure of the proposed system in *yz* plane is the same as modified integral imaging [50, 56, 75], and each elemental image is integrated at the center of the cylinder and reconstructs the virtual 3D image which has the vertical parallax as shown in Figure 2.18.

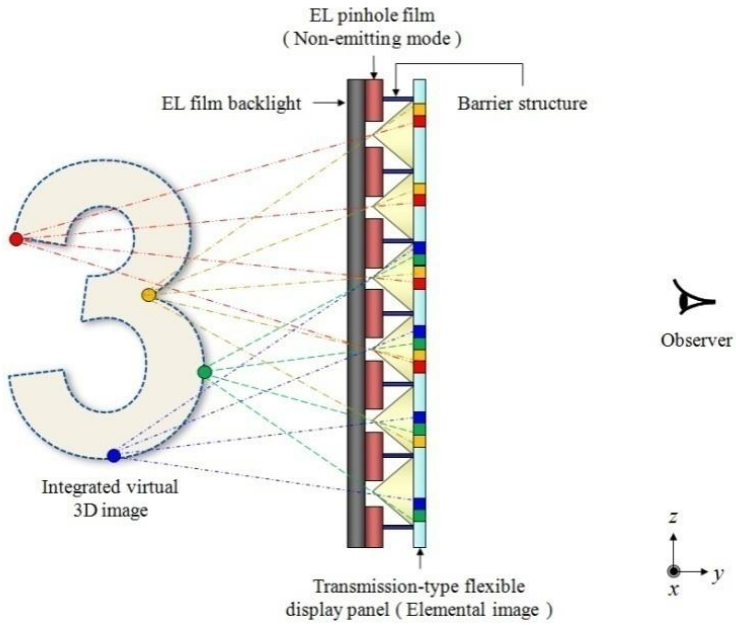

Figure 2.18 The 3D display principle of the proposed system in vertical parallax

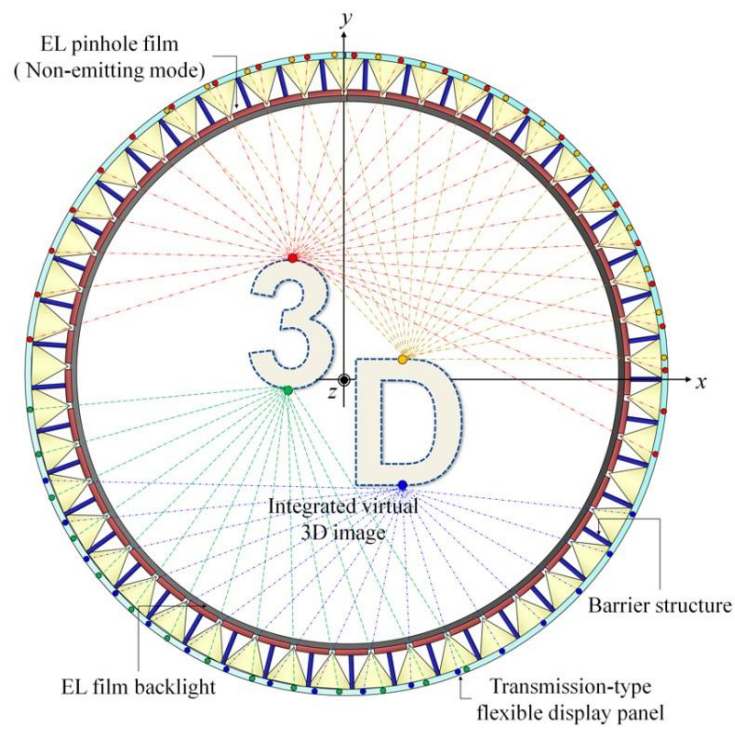

Figure 2.19 The 3D display principle of the proposed system in horizontal parallax

The other cross section of the proposed system in *xy* plane shows the 3D display principle in horizontal parallax as shown in Figure 2.19. Each point light source gives the horizontal parallax which is limited by the viewing angle in modified integral imaging. However, the cylindrically arranged point light source array gives the continuous horizontal parallax in 360-degrees. Therefore, the observer can see the virtual 3D image all around the cylinder structure and feel the virtual reality as shown in Figure 2.19.

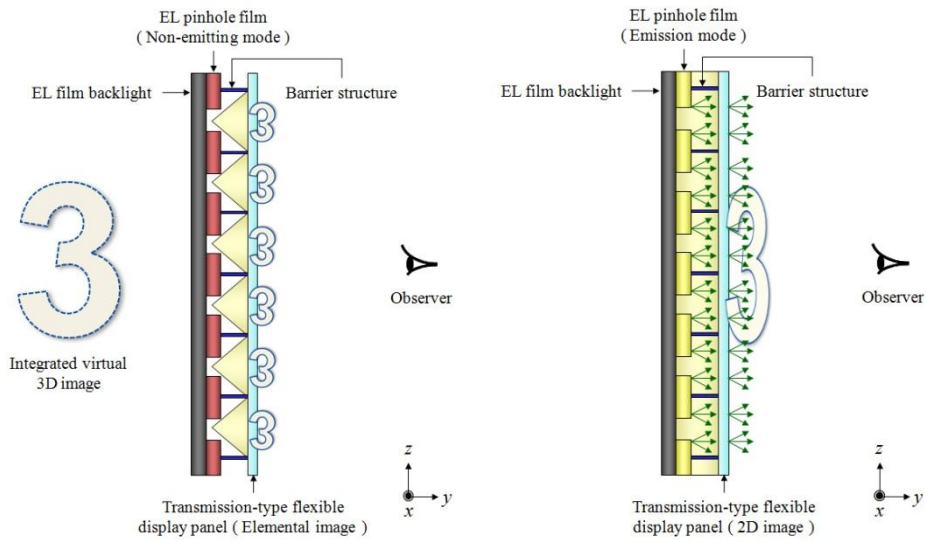

(a) (b)

Figure 2.20 The principle of the 3D/2D convertibility in the proposed system: (a) 3D mode, (b) 2D mode

In addition to the 360-degree viewing angle, the proposed system has 3D/2D convertibility which is based on the backlight switching from the point light source to surface light source as shown in Figure 2.20. Two sheets of EL film generate the point light source array when the EL pinhole film is in non-emitting mode and the EL film backlight shines behind the EL pinhole film in 3D mode as shown in Figure 2.20(a). In this situation, the transmission-type flexible display panel shows the elemental image set of the virtual 3D image, and the principles are the same in Figure 2.19 and Figure 2.20. In 2D mode, the EL film and EL pinhole film emit the light together and generate the surface light source as shown in Figure 2.20(b).

2.2.3 **Analysis on the characteristic parameters and viewing zone of the 360-degree viewable cylindrical integral imaging system**

The parameters for the analysis on the characteristics of the proposed system are shown in Figure 2.21. The point light source array is located on a cylinder with radius *r*, and the transmission-type flexible display panel has gap *g* distant from the point light source array. When the point light source is arranged at a regular interval *p*, each elemental image region without flipping p_E is fixed, and each diverging angle of point light source θ is derived as follows:

$$\theta = 2\arctan\left\{\frac{(r+g)\sin\left(\frac{p}{2r}\right)}{(r+g)\cos\left(\frac{p}{2r}\right)-r}\right\}. \tag{2.6}$$

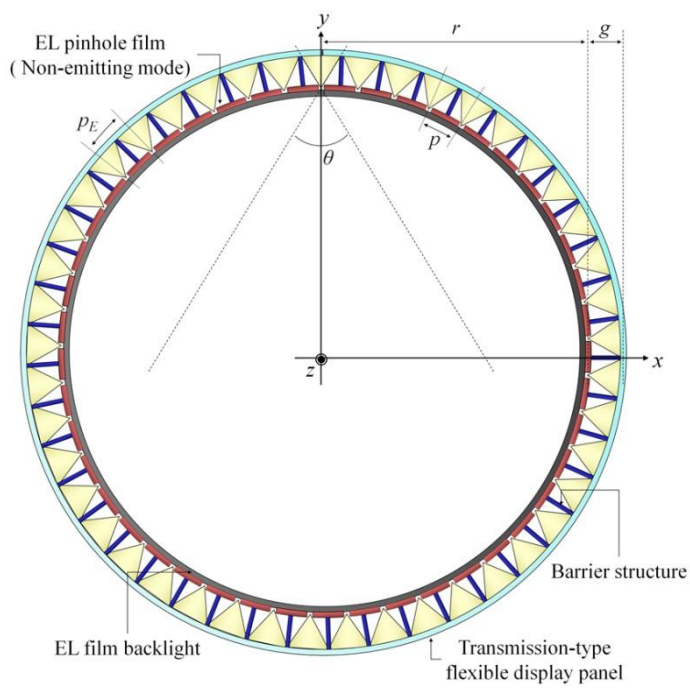

Figure 2.21 The viewing parameters of the proposed system

For preventing flipping problem, the viewing angle of each point light source is limited by Eq. (2.6) and the implementation of the barrier structure is essential to block

the rays. Figure 2.22 shows the necessity of the barrier structure. As shown in Figure 2.22(a), the rays in the viewing angle of each point light source interfere with each other in the system without barrier structure. In this situation, t is the thickness of the EL pinhole film, d is the diameter of the pinhole, and the viewing angle of each point light source without the barrier structure θ_r is derived as follows:

$$\theta_r = 2\arctan\left(\frac{d}{t}\right). \tag{2.7}$$

From Eq. (2.7), the elemental image regions of each point light source are interfered with each other, and the flipped regions appear as shown in Figure 2.22(a). To overcome these problems, I implement the barrier structure in the interval of each elemental image region without flipping as shown in Figure 2.22(b). Each elemental image region for the point light source without flipping p_E is derived as follows:

$$p_E = \frac{p(r+g)}{r}. \tag{2.8}$$

As shown in Figure 2.22(b), the observer can see the 3D image without flipping when each viewing angle of point light source is limited by Eq. (2.6).

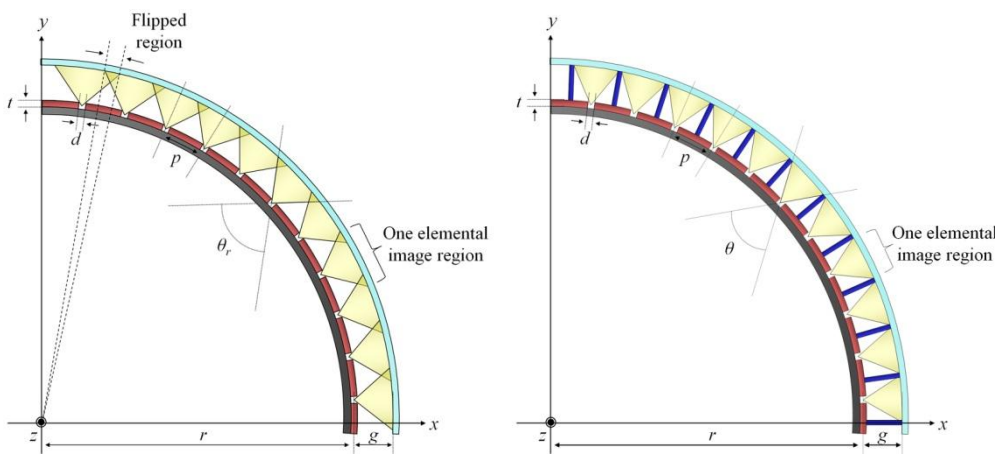

(a) (b)

Figure 2.22 The 360-degree viewable cylindrical integral imaging (a) without barrier structure and (b) with barrier structure

However, the size of reconstructed virtual 3D image is limited by each viewing angle of point light sources as shown in Figure 2.23. The total overlapped area of maximum viewing angles in each point light source is located at the center of the cylinder structure with radius r_v, which is defined as viewing zone. The observer can see the reconstructed 3D image without flipping in 360 degrees when it is integrated in the viewing zone. Through some calculations using the tangent line at the boundary of the viewing zone, the maximum radius of the viewing zone r_v can be expressed as

$$r_v = r\sin\left(\frac{\theta}{2}\right) = r\sin\left[\arctan\left\{\frac{(r+g)\sin\left(\frac{p}{2r}\right)}{(r+g)\cos\left(\frac{p}{2r}\right)-r}\right\}\right]. \tag{2.9}$$

From Eq. (2.9), I find that I can enhance the viewing zone using a larger cylinder radius and shorter gap.

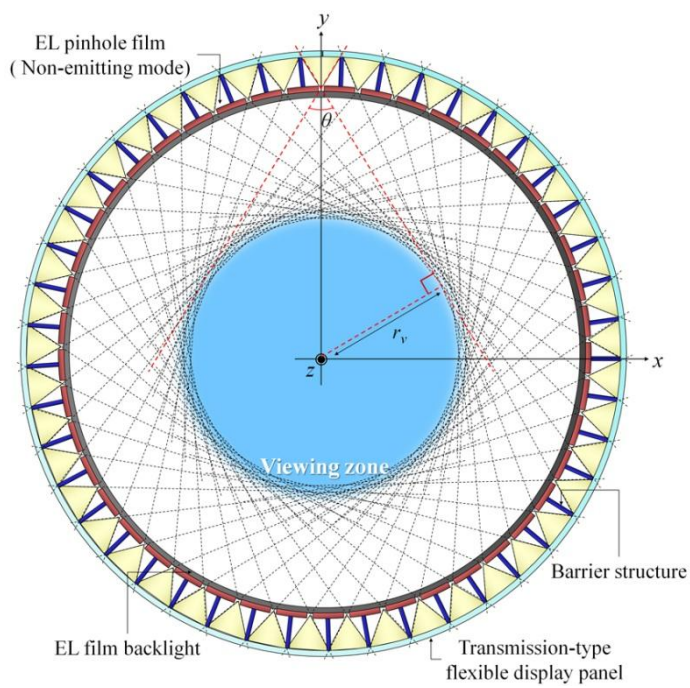

Figure 2.23 The viewing zone of the proposed system

2.2.4 **Experiment**

I performed experiments to verify the feasibility of the proposed system as shown in Figure 2.24. The system is composed of the EL pinhole film, EL film backlight, barrier structure, transmission-type flexible display panel, and DC-AC inverter for the power supply. Each specification of the proposed system component is shown in Table 2.1. In order to generate the cylindrically arranged point light source array, I stacked EL film and EL pinhole film, and the barrier structure for preventing flipped image is implemented by the acryl. The proposed system displays the elemental image on the transmission-type flexible display panel. However, the transmission-type flexible display panel is not developed and commercialized yet. Therefore, I used an overhead projector (OHP) film and printed elemental images on it using a laser printer. In this situation, although OHP film cannot display moving image and change the elemental image, it can verify the feasibility of the proposed method. If the flexible display panel is applied in the proposed method, the moving image can be displayed. However, the resolution and brightness of the integrated 3D image will be lower, and the thickness of the system will be thicker than the OHP film based method. Therefore, the pinhole specification and viewing characteristic need to be recalculated by the specification of the flexible display panel.

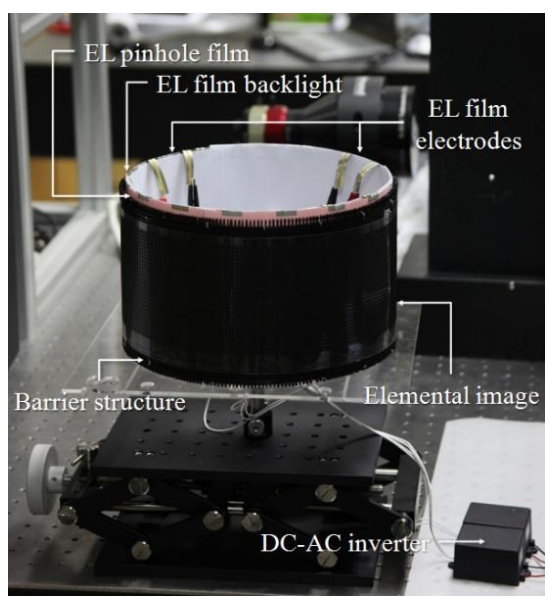

Figure 2.24 The experimental setup

Table 2.1 The specification of experimental setup

Barrier structure	
Width (gap)	4 mm
Thickness	1.5 mm
Radius	117 mm
Height	140 mm
EL pinhole film	
Size	710 mm × 136 mm
Thickness	0.4 mm
The number of pinholes	236 × 45
The diameter of pinholes	200 ㎛
The pinhole interval	3 mm
The radius of the cylinder structure	113 mm
Operation voltage	DC 12 V to AC 110 V
Current consumption	18 mA/mm^2
Luminance	150 cd/m^2
Elemental image	
Resolution	1200 DPI (21.2 ㎛)

Figure 2.25 shows the experimental results of the backlight conversion for the 3D/2D convertibility. For reconstructing 3D image, the EL film backlight emits the light and EL pinhole film is in non-emitting mode, and the point light source array is generated as shown in Figure 2.25(a). The use of pinhole array leads to the brightness degradation in 3D mode, and the barrier structure also dims the backlight. The brightness of the proposed method is 150 cd/m^2 in 2D mode and 2.1 cd/m^2 in 3D mode. Therefore, the optical efficiency of the 3D mode is 1.4% of the 2D mode and nearly same as the aperture ratio of the EL pinhole film. The viewing angle of each point light source is 42.5 degrees from Eq. (2.6) in ideal case and 38.8 degrees in the experimental result. Therefore, the width of observed viewing zone is about 75 mm, which is near the width of calculated viewing zone 82 mm from Eq. (2.9).

Figure 2.25(b) shows the surface light source for 2D mode which is generated by the EL film backlight and EL pinhole film in emission mode. Some degradation in surface light source is incurred by the thickness of the barrier structure. However, it can be resolved by using a thinner barrier structure.

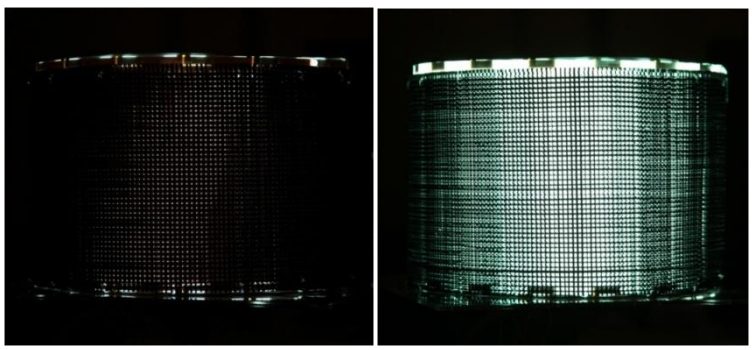

(a) (b)

Figure 2.25 The experimental result of backlight switching: (a) 3D mode, (b) 2D mode

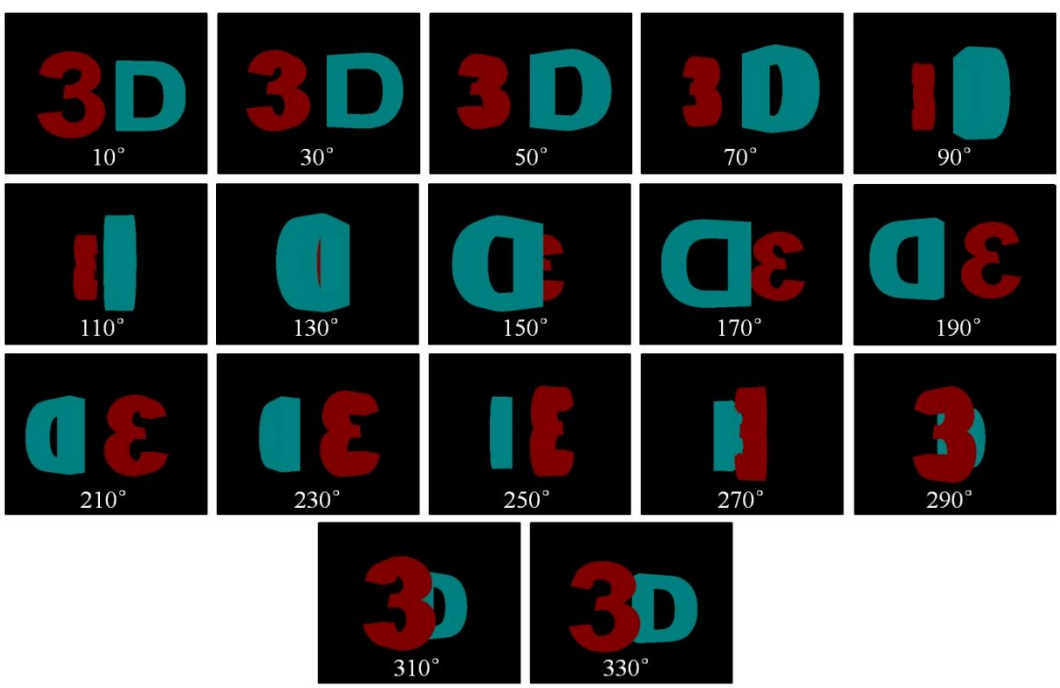

Figure 2.26 The 3D modeled letters of computer generated elemental image

For experiments in 3D mode, I generate the elemental image set of virtual 3D image

and print it on the OHP film in 1200 DPI. The elemental image is generated by computer using OpenGL for the virtual 3D images at the center of the cylinder, which are 3D modeled letters ‘3’ and ‘D’. Figure 2.26 presents the 3D modeled letters using OpenGL at different viewing positions.

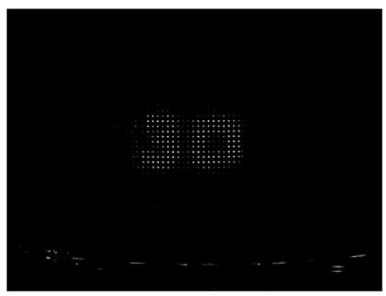

(a)

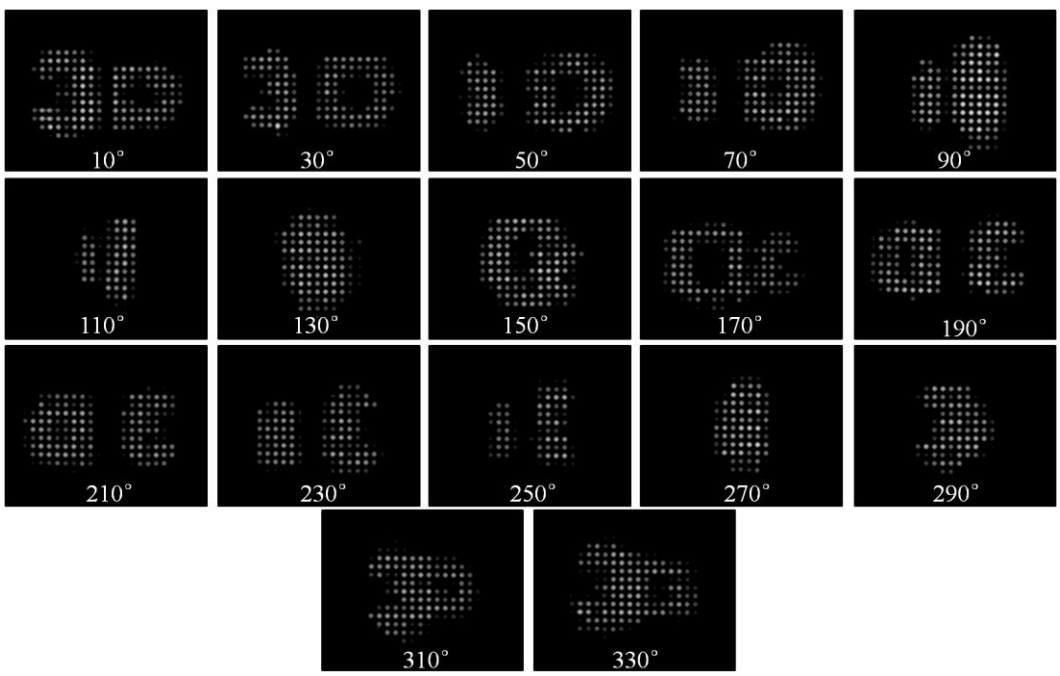

(b)

Figure 2.27 The experimental results of 3D mode: (a) example of reconstructed virtual 3D image observed from a specific direction, (b) reconstructed virtual 3D images at different viewing positions around the *z*-axis

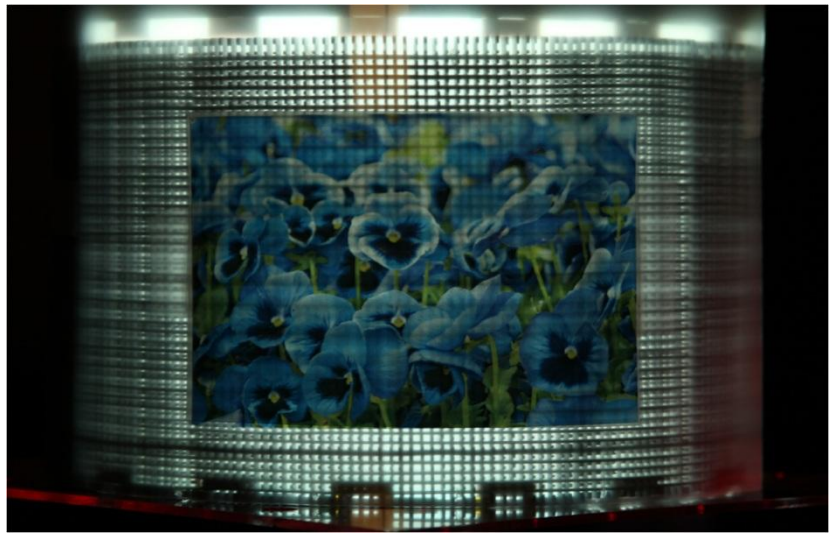

Figure 2.28 The experimental result of 2D mode

Figure 2.27 shows the experimental results in 3D mode, and the observer can see the different perspectives in the different viewing positions around the cylinder in 360 degrees. The 3D modeled letters ‘3’ and ‘D’ are formed 25 mm in front of and behind the center position, respectively. Thus, the proposed system can reconstruct the virtual 3D image in the viewing zone without flipping. After switching EL film backlight to surface light source mode, I perform an experiment on 2D mode as shown in Figure 2.28. The 2D image on OHP film instead of elemental image is displayed using surface light source mode of EL film backlight of cylindrical structure.

2.2.5 **Conclusion**

In this study, I proposed a 360-degree viewable cylindrical integral imaging system using EL films. It is based on cylindrically arranged point light source array which is generated by the EL film backlight and the EL pinhole film. Using this method, 360-degree viewable 3D display can be made easily and cheaply with simple structure. Moreover, the proposed system has 3D/2D convertibility. Therefore, this structure could be competitive for 3D display for many viewers, 3D signboard, and 3D information display.

2.3 Integral imaging using color filter pinhole array on display panel

I propose enhancement methods of pinhole-type integral imaging for ray density, resolution and expressible depth range using color filter pinhole array on liquid crystal display panel with projection-type integral imaging scheme. A color filter structure on liquid crystal display panel acts as pinhole array in integral imaging with separation of color channel. In conventional pinhole-type integral imaging, the resolution, viewing angle and ray density are limited by the pinhole interval, the width and thickness of pinhole structure and the gap between display panel and pinhole array. To overcome the limitation of pinhole interval, I use the color filter pinhole array on display panel and the projection-type integral imaging scheme. The use of color filter pinhole array and projection scheme can enlarge the region of one-elemental image and improve the resolution and ray density remarkably. This paper presents the experimental result of proposed method and comparison of conventional methods.

2.3.1 Introduction and motivation

2.3.1.1 Introduction

Integral imaging is one of promising techniques in autostereoscopic type three-dimensional (3D) displays [3, 4, 10, 35]. After the emergence of display market to stereoscopic type 3D display, autostereoscopic type 3D display will be the main stream of 3D display and integral imaging is one of promising autostereoscopic display technologies. In the autostereoscopic type 3D display based on the lens array and spatial multiplexing technique, integral imaging has many advantages, which can reconstruct 3D image with full-parallax and quasi-continuous viewing points using elemental image and lens array.

Pinhole-type integral imaging which uses the pinhole array instead of lens array is one of the modified integral imaging systems, which can be made more simplified than lens array based method and easily convert between 2D and 3D modes [56, 60–64, 70, 76, 77]. However, the pinhole based integral imaging has intensity degradation, limited viewing angle, and low resolution problems fundamentally. The principle of pinhole-type

integral imaging is the same as focal mode of integral imaging [10, 35]. In focal mode of integral imaging and pinhole-type integral imaging, each lens acts as the voxel of reconstructed 3D image and the spatial resolution of 3D image is the same as the number of pinhole array or lens array. The major difference between focal mode integral imaging and pinhole-type integral imaging is the use of pinhole array instead of lens array, which incurs another limitation from pinhole specification. The specification of pinhole-type integral imaging is derived from characteristics of pinhole array and parameters. The viewing angle, resolution, ray density and expressible depth range are limited by the diameter, thickness and interval of pinhole array. Pinhole intervals, size of elemental image region and system parameter limit the viewing angle, depth range, ray density and resolution [78, 79].

To overcome the limitation in pinhole-type integral imaging, I propose the color filter pinhole array based integral imaging with projection scheme. In pinhole-type integral imaging, the interval of pinhole array is limited as following viewing angle of each pinhole when the gap between pinhole array and display, thickness and diameter of pinhole array are fixed. In previous researches, many research groups proposed the enhancement methods of viewing angle and resolution in integral imaging using display panel as pinhole array with time-multiplexing technique and pinhole pattern control [70, 75, 77, 80]. The pinhole-type integral imaging with color filtering and sub-pixel sampling is the first proposed method for enhancement of integral imaging. In this study, I explain the limitation of pinhole parameters in pinhole-type integral imaging system and propose the enhancement method using color filter pinhole array. I show the comparison between analyses of the specification of proposed method and previous pinhole-type integral imaging systems and present experimental result with resolution-enhanced system.

2.3.1.2 **Limitation of viewing angle**

In pinhole-type integral imaging, the characteristics of system is limited by specification of pinhole array as shown in Figure 2.29. The parameters of pinhole-type integral imaging is composed of interval between pinhole array I_p, diameter of pinhole d, gap between pinhole array and display panel g, thickness of pinhole array t and the viewing angle of display panel θ. From the principle of pinhole-type integral imaging, the spatial

resolution of system is the same as the number of pinhole array and the ray density, viewing angle and angular resolution are limited by pinhole specifications.

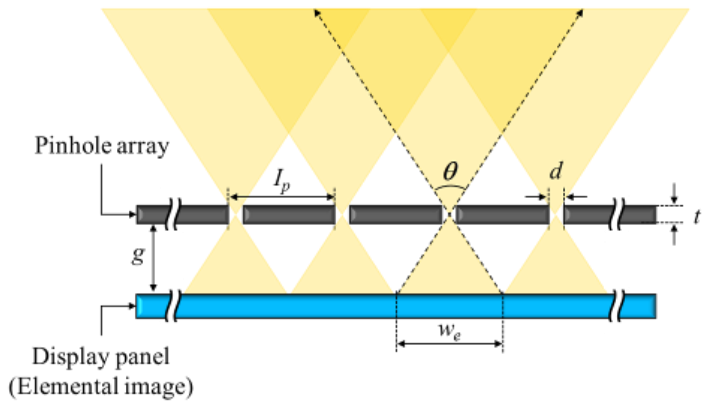

Figure 2.29 Parameters of pinhole-type integral imaging

Generally, viewing angle of integral imaging is the same as viewing angle of each pinhole, and one elemental image region w_e is derived from the relation between the gap g and viewing angle θ as following:

$$\theta = 2\tan^{-1}\left(w_e / g\right). \tag{2.10}$$

When the thickness of pinhole array and diameter are fixed, the viewing angle θ is limited by the ray optic assumption because of larger diameter than wavelength of visible light. Equation (2.11) shows the derived viewing angle of pinhole array with geometrical parameters.

$$\theta = 2\tan^{-1}\left(d / t\right). \tag{2.11}$$

From Eqs. (2.10) and (2.11), the pinhole interval between each pinhole array I_p is limited as follows:

$$I_p = d\left(1 + 2g / t\right), \tag{2.12}$$

where pinhole diameter is denoted as d, gap g and thickness t. In general pinhole-type integral imaging system, pinhole diameter, gap and thickness are fixed and the pinhole interval and derived viewing angle θ are limited by fixed parameters. In addition, the

spatial resolution of pinhole-type integral imaging is also limited because it is the same as the number of pinholes in the array on the same plate. Therefore, the optimized pinhole interval I_p is the same as the one elemental image region w_e as shown in Figure 2.30.

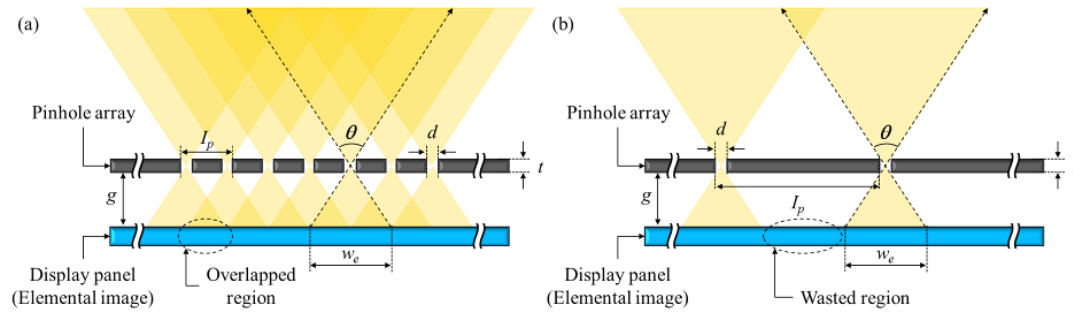

Figure 2.30 Limitation of pinhole interval with fixation of pinhole specification d, t and g: (a) case of too narrow pinhole interval ($I_p < w_e$) and (b) too broad pinhole interval ($I_p > w_e$)

If the pinhole interval is smaller than one elemental image region, each elemental image is overlapped and the observer cannot avoid a flipped image problem as shown in Figure 2.30(a). On the other hand, elemental image region is wasted and the spatial resolution is decreased when the pinhole interval is larger than one elemental image region. In pinhole-type integral imaging or focused mode integral imaging, the spatial resolution and viewing angle has trade-off relation, fundamentally. However, pinhole-type integral imaging has additional constraint which is caused by the specification of pinhole. Therefore, the other structural or methodological idea is needed to overcome the limitation of pinhole interval from pinhole specification.

2.3.2 **Principles of proposed method**

2.3.2.1 **Pinhole-type integral imaging using color filter pinhole array with projection scheme**

To overcome the limitation from the relation between pinhole interval and viewing angle, I propose the color filter pinhole array based integral imaging using projection scheme. As shown in Figure 2.30, the characteristics of pinhole-type integral imaging are defined by the pinhole interval and size of one elemental image region, which cannot be extended without time multiplexing or spatial multiplexing techniques. In previous researches, the

moving pinhole array with time multiplexing or polarization switching techniques were proposed for enhancement of resolution or viewing angle [60, 70]. In this study, the proposed method uses the other multiplexing technique which is color channel multiplexing using color filter pinhole array on display panel and projection scheme.

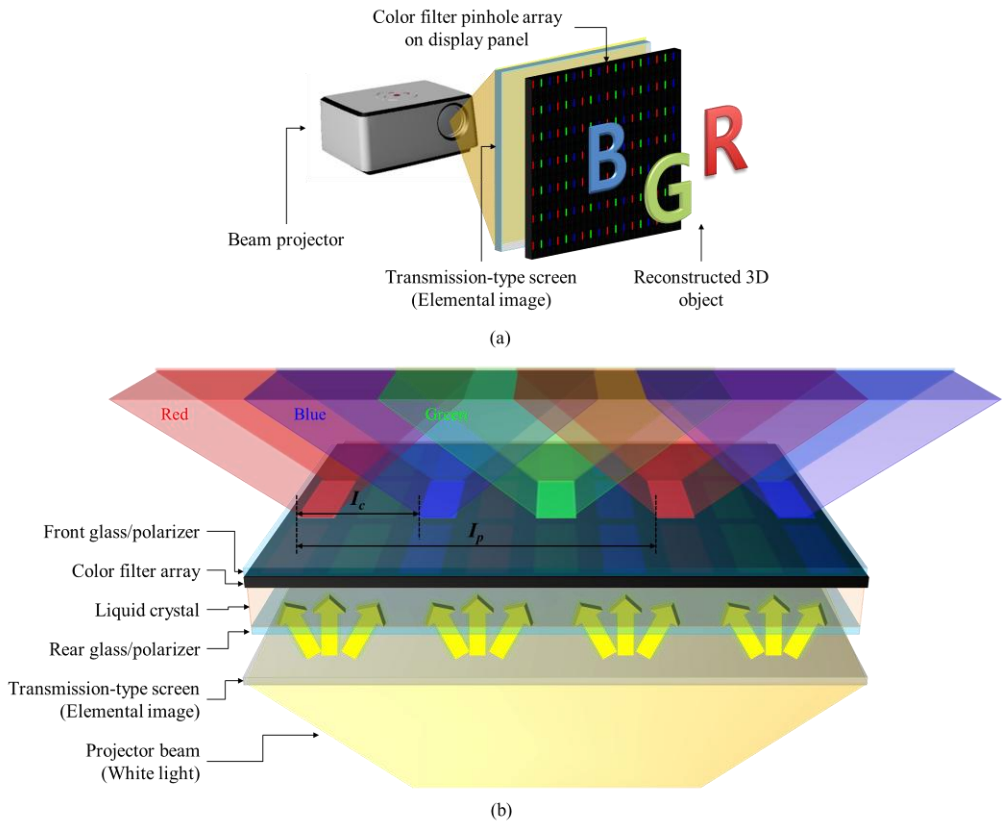

Figure 2.31 Concept of proposed method: (a) scheme of proposed method, (b) structure of color filter pinhole array on LCD with projection-type integral imaging

Figure 2.31 shows the concept of the proposed method and its layer structure. The scheme of the proposed method is not a complex and singular setup. In the proposed method, sub-pixel structure with color filters on liquid crystal display (LCD) or other transparent type display panel is substituted for the conventional pinhole array and the rear display which has to show the elemental image is also replaced by the projection screen and projector as shown in Figure 2.31(a). Many research groups already used LCD panel or other types of display panels as the pinhole array with electrical control in

integral imaging [60, 70, 80]. However, they did not focus on the sub-pixel structure on display panel and filtering of color channels, but the electrical controllability for 3D/2D convertible system or time multiplexing technique. In previous researches, the pinhole array of integral imaging is generated by turning on and off of each pixel on display panel without controlling sub-pixels and its color filters.

In this study, the proposed method controls the sub-pixels of transparent type display panel for filtering color channels of elemental image set, which can enhance the resolution, viewing angle and ray density of integral imaging. In conventional case of integral imaging, the attachment of color filters on the lens array or pinhole array causes the loss of information and reduction of resolution. To avoid loss of information, the proposed method is based on the projection type integral imaging which can emit red, green and blue channels on one pixel of projection screen, which can enhance the characteristics of pinhole-type integral imaging when used in combination with color filter pinhole array.

Figure 2.31(b) shows more detailed concept of the proposed method with layer structure. When the elemental image is projected on the projection screen located at rear of transparent type display panel by beam projector, the elemental image has white light information mixed by three channels in one pixel unit on projection screen and is diffused to all directions in diffusing angle of projection screen. The white light rays passing through the gap distance and liquid crystal layer are filtered to red, green and blue channel elemental image by the color filter on the sub-pixel structure. To enhance the viewing angle and intensity of reconstructed 3D image, the transmission-type screen is attached on the back surface of display panel. Therefore the gap is set to the thickness of the layers of rear glass and polarizer and the thickness of pinhole is the same as the thicknesses of the transparent electrode layer, the color filter layer and liquid crystal layer. From the limitation of pinhole structure, the viewing angle and interval between pinholes are defined by limited size I_p, which causes the limitation of conventional integral imaging. However, the color filter pinhole array can reduce the pinhole interval between different color channels. In the proposed method, elemental images in different color channels can be overlapped with each other, which enhances the resolution and ray density.

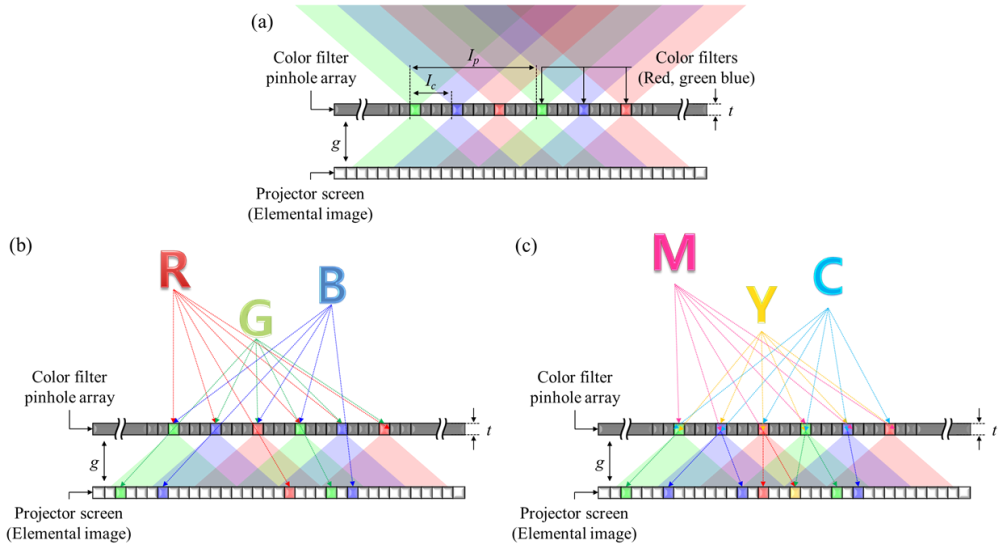

Figure 2.32 Principle of pinhole-type integral imaging using color filter pinhole array: (a) viewing angle and elemental image region of each color channel, (b) principle of pickup process using color filter pinhole array in red, green and blue color objects, (c) principle of pickup process using color filter pinhole array in magenta, yellow and cyan color objects

Figure 2.32 shows the principle of proposed method in detail. From Eq. (2.12), the interval of pinhole array is limited by I_p which is the same as the largest elemental image region with maximum viewing angle. However, the use of color filter pinhole array makes the proposed system possible to increase the resolution and reduce the interval of each pinhole. As shown in Figure 2.32(a), the pinhole interval of same color channel has to keep the minimum pinhole interval I_p from Eq. (2.12) which is defined by the specification of pinhole whereas the color filter pinhole of different color channel can be generated between the pinholes of same color channel. For example, when the red color pinhole keeps the minimum pinhole interval I_p, the green and blue color pinholes can be made between two red pinholes with same interval I_c. Each different color channel of elemental image can be mixed freely whereas the same color channels obviously keep the minimum pinhole interval I_p. Therefore, the optimized interval of color filter pinhole array I_c is one third of minimum pinhole interval I_p which is limited by the width of pinhole for color filter pinholes as follows:

$$I_p = 3I_c = d\left(1 + 2g / t\right) > 3d. \tag{2.13}$$

From Eq. (2.13), the minimum interval of pinholes in same color channel I_p cannot be set to a multiple of three for prevention of repeating same color pinholes and the gap has to be larger than thickness of pinhole array.

In the pickup process for the proposed method, the spatial information of 3D object is recorded by the different color filter pinhole array depending on the color channels of 3D object as shown in Figure 2.32(b) and (c). As shown in Figure 2.32(b), if each 3D object has red, green and blue color texture, spatial information of 3D object is filtered by red, green and blue color channel filter on pinholes. In the case of Figure 2.32(b), the 3D object is sampled by the minimum pinhole interval I_p and its rays pass only one color pinholes. On the other hand, the rays from 3D object is passing through the two different color filter pinholes and record the spatial information of 3D object when the textures of 3D object are composed of magenta, yellow and cyan colors as shown in Figure 2.32(c). Therefore, the sampling rate of 3D object in the proposed method depends on the texture color of 3D object.

2.3.2.2 **Comparison of the proposed method with conventional pinhole-type integral imaging**

The main idea of the proposed method is sub-pixel sampling of 3D object with color channel filtering using color filters on LCD panel and projection scheme. To show the advantage of the proposed method compared with previous pinhole-type integral imaging, I plan all possible types of pinhole-type integral imaging using display panels or projection scheme as shown in Figure 2.33. The pinhole-type integral imaging is composed of pinhole array part for spatial sampling of 3D object and display part for recording and displaying elemental image. I assume that the pinhole array is made by the same thickness, diameter and pinhole interval for same viewing angle, size of elemental image and gap distance. In addition, the sub-pixel pitch of display panel and pixel pitch of projection image on the projection screen are same. To compare each setup of pinhole-type integral imaging and the proposed method, I analyze the resolution, ray density and expressible depth range of each method.

To compare each method on the characteristics of 3D display, the resolution, maximum ray density and expressible depth range have to be defined. The resolutions of 3D display are classified by the spatial resolution and angular resolution. In pinhole-type integral imaging, the spatial resolution R_s is defined by the number of pinholes in pinhole array and the angular resolution R_θ is defined by the number of pixels in one elemental image region as follows:

$$\begin{aligned} R_s &= W / I, \\ R_\theta &= w_e / T_p, \end{aligned} \tag{2.14}$$

where the width of pinhole array is W, the minimum interval of pinholes is I and the period of pixel on elemental image plane is T_p.

Figure 2.33(a) shows the one of conventional pinhole-type integral imaging systems composed of passive pinhole array and display panel and Figure 2.33(e) shows the proposed method with ray distribution. In the comparison of two different setups, the resolution, ray density and expressible depth range are enhanced by color filter pinhole array and projection scheme. In the case of Figure 2.33(a), the minimum pinhole interval is derived from Eq. (2.12) and set as I_p, and the period of pixel T_p is the same as the pitch of three sub-pixels $3p_{sb}$. However, the pinhole interval of the proposed method is set as I_c one-third of I_p and the period of pixel is defined by p_{sb}. From different specifications, the spatial resolution R_s is enhanced by 3 times, from $W/3I_c$ to W/I_c, and the angular resolution R_θ is also increased, from $w_e/3p_{sb}$ to w_e/p_{sb}, in each color channel. The ray density of system R_d is derived by the number of rays in unit area w_e, which is defined by consideration of each color channel as follows:

$$R_d = \left(R_{\theta,R} + R_{\theta,G} + R_{\theta,B} \right) / w_e, \tag{2.15}$$

where the angular resolutions of each channel are $R_{\theta,R}$, $R_{\theta,G}$ and $R_{\theta,B}$. From Eq. (2.15), the ray density of the proposed method is enhanced by 3 times, from $1/p_{sb}$ to $3/p_{sb}$. In addition, the nearest expressible depth d_{near} of the proposed method is reconstructed at nearer than the case of Figure 2.33(a), from $3I_c g/w_e$ to $I_c g/w_e$ using trigonometric proportion. Therefore, the proposed method is improved in the spatial and angular resolution, ray density and expressible depth range as compared with Figure 2.33(a). In comparison of

the case of Figure 2.33(b) and (e), the angular resolution and ray density are improved by 3 times whereas the spatial resolution and nearest expressible depth are conserved.

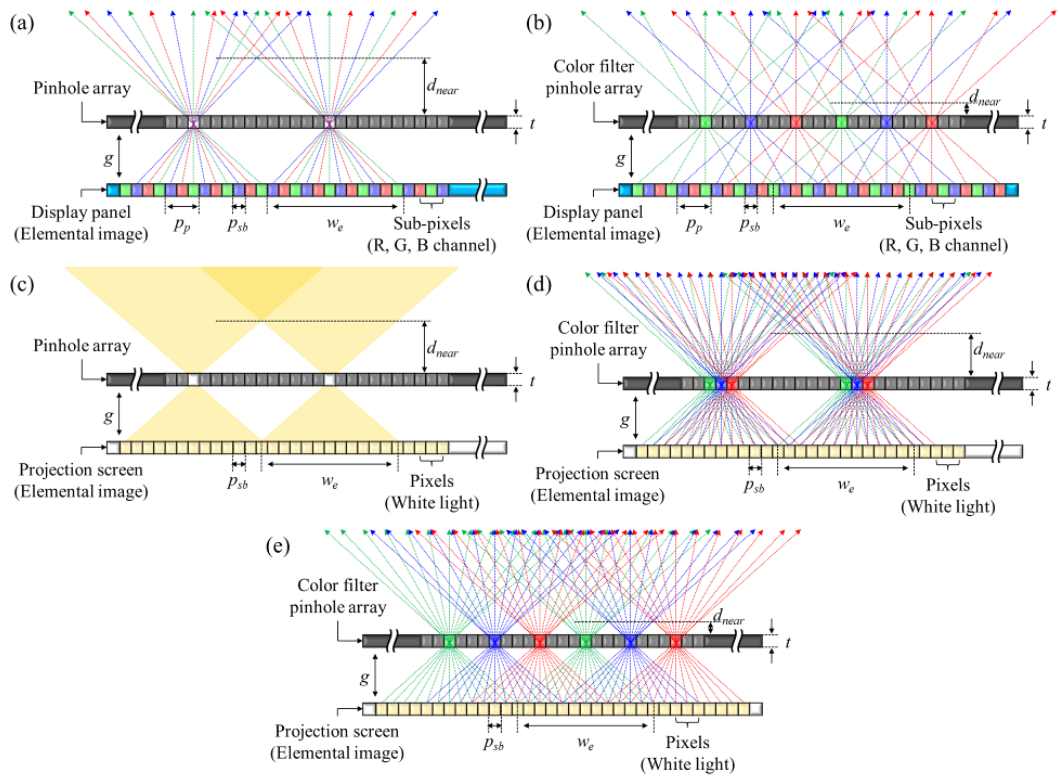

Figure 2.33 Comparison of proposed method and other pinhole-type integral imaging methods: (a) conventional pinhole-type integral imaging using passive pinhole array and display panel, (b) conventional pinhole-type integral imaging using two LCD display panels, (c) conventional pinhole-type integral imaging using passive pinhole array and projector, (d) conventional pinhole-type integral imaging using display panel and projector and (e) proposed method using color filter pinhole array on display panel and projector

In comparison of the proposed method and conventional methods using projection scheme as shown in Figure 2.33(c) and (d), the angular resolution and ray density are conserved while the nearest expressible depth, spatial resolution and color uniformity of reconstructed image are improved. In the case of the conventional projection-type integral imaging using pinhole array as shown in Figure 2.33(c), the voxels are reconstructed on a

cycle of the interval of pinhole I_p which is 3 times larger than I_c with full color expression. On the other hand, the proposed method reconstructs the voxels on 3D space with I_c cycle in red, green and blue channels with sub-voxel sampling. Therefore, the reconstructed 3D object using the proposed method has higher fill-factor and spatial resolution although the color expression is limited in the scale of sub-voxel. However, the observer cannot be perceived the color separation of sub-voxels in the optimized observer distance where the observer cannot perceive the cycles of voxel in the conventional projection-type integral imaging using pinhole array. Therefore, the proposed method can reconstruct the 3D image in higher spatial resolution than conventional method. In the conventional projection-type integral imaging using pixels on display panel, the resolution and ray density are conserved whereas the nearest expressible depth and the color uniformity of reconstructed 3D object are improved as shown in Figure 2.33(d) and (e).

2.3.3 **Experimental setup and results**

2.3.3.1 **Experimental setup**

To verify the feasibility of the proposed method, I performed the experiment as shown in Figure 2.34. The experimental setup is composed of LCD display panel for pinhole pattern generated by color filters using sub-pixel control, transparent-type projection screen, relay optics and beam projector for projection of elemental image. In the proposed method, the one of improvements is the use of beam projector for displaying elemental image with narrow pixel pitch and multichromatic pixel unit. For narrow pixel pitch of elemental image from beam projector, I set the relay optics from beam projector to LCD panel using normal prime lens and zoom lens of camera. The elemental image from the beam projector is focused to the CCD size of digital camera and then it is magnified to the transparent-type projection screen attached on the back surface of LCD by zoom lens without severe distortion. To enhance the resolution of 3D image in the proposed method, the gap between pinhole array and projection screen is set to the minimum value which is the same as the thickness of rear structures in LCD panel. Therefore, the projection screen is attached on the back surface of LCD panel, the gap is set to minimum distance and the 3D image is reconstructed by highest resolution with minimum pinhole interval.

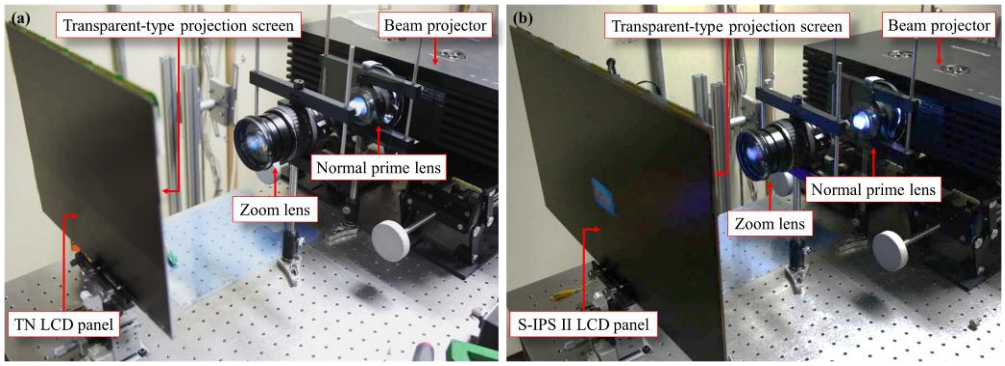

Figure 2.34 Two different experimental setups for proposed method: (a) experimental setup using TN LCD panel and (b) S-IPS II panel

Table 2.2 Specification of experimental setup

Setup	**Specification**	**Characteristic**
TN LCD panel (LG LM170E01)	Size	17-inch
	Resolution	1280 by 1024
	Pixel pitch	0.264 mm
	Sub-pixel pitch	88 μm
	Viewing angle	120° by 110°
S-IPS II LCD panel (LG IPS236V-PN)	Size	23-inch
	Resolution	1920 by 1080
	Pixel pitch	0.265 mm
	Sub-pixel pitch	88.3 μm
	Viewing angle	178° by 178°
Relay optics	Normal prime lens	Canon EF 50mm f/1.4 USM
	Zoom lens	Canon EF 28-135mm f/3.5-5.6 IS USM
Projection image	Resolution	1920 by 1080
	Pixel pitch	32 μm
Pinhole specification	Thickness	0.217 mm
	Gap	1.192 mm
Pinhole specification in conventional method	Pinhole width	88 μm, 88.3 μm
	Pinhole interval	4 pixels (1.056 mm, 1.06 mm)
Pinhole specification in proposed method	Pinhole width	88 μm, 88.3 μm
	Pinhole interval of same color channel	4 pixels (1.056 mm, 1.06 mm)
	Pinhole interval of different color channel	4 sub-pixels (0.352 mm, 0.3533 mm)

For considering effect of viewing angle of LCD panel, I set the two different setups

of proposed method using twisted nematic (TN) panel and super in-plane switching (S-IPS) II panel as shown in Figure 2.34(a) and (b). The geometrical specifications of two different LCD panels, such as thickness and pixel pitch, are approximately the same with each other but the viewing angle, brightness and contrast are improved in S-IPS II panel. Table 2.2 shows the further specifications of experimental setups.

To compare the conventional method and proposed method, I generated the two different pinhole patterns electrically as shown in Figure 2.35. In the pinhole patterns for conventional method, each pixel acts as one pinhole and the pinholes are arranged by 4 pixels pinhole interval as shown in Figure 2.35(a) and (c), whereas the proposed method uses the sub-pixel as color filter pinhole and the pinhole interval of same color channel is the same as the conventional method, 4 pixels, and the pinhole interval of different color channel is one-third of conventional method, 4 sub-pixels, as shown in Figure 2.35(b) and (d).

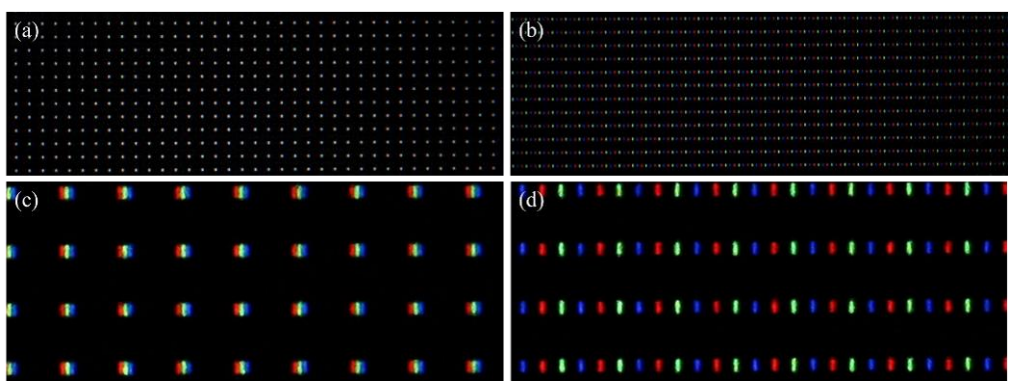

Figure 2.35 Illumination results of pinhole array in conventional method and proposed method: (a) illumination result of conventional pinhole pattern and (b) proposed method, (c) 5 times magnified point light source in conventional method and (d) proposed method.

Figure 2.36 shows the elemental image sets of 3 white letters S, N and U on different depth plane 30 mm, -20 mm and 10 mm from the display panel. As shown in Figure 2.36(c) and (d), the sampled elemental image of conventional method is separated by pinhole interval while the elemental images of color filter pinhole array are freely intrude each elemental image region. Figure 2.37 shows the magnified elemental image of high resolution objects of two-fish on different depth plane 30 mm in front of and behind of

pinhole array.

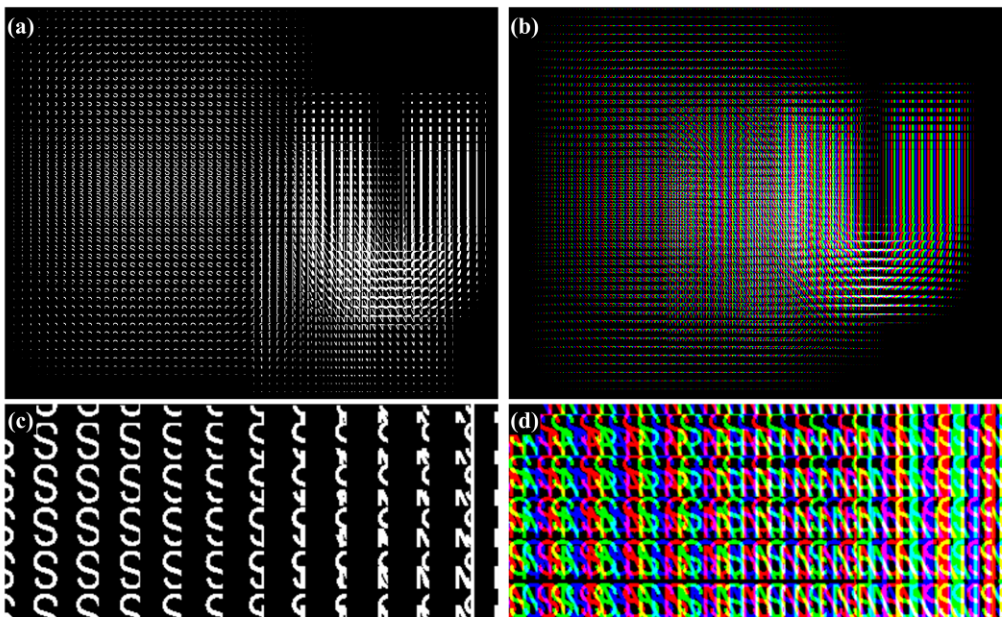

Figure 2.36 Elemental image of 3 letters in different depths for conventional method and proposed method: (a) elemental image for conventional method and (b) proposed method, (c) magnified elemental image for conventional method and (d) proposed method.

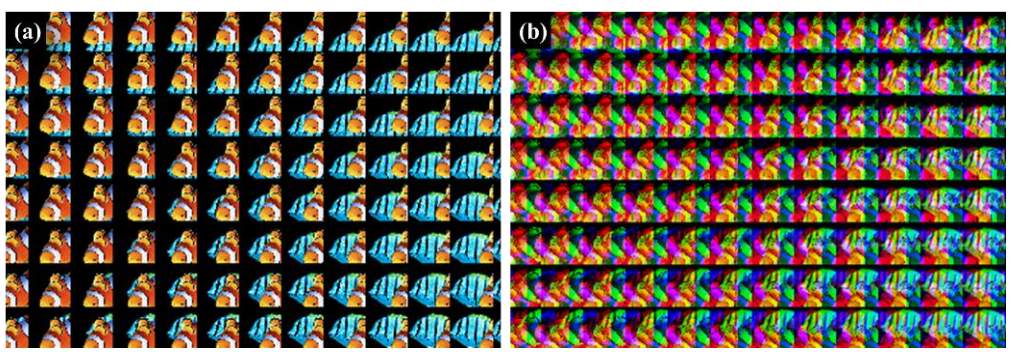

Figure 2.37 Magnified elemental image of high resolution objects for conventional method and proposed method: (a) magnified elemental image for conventional method and (b) proposed method

2.3.3.2 **Experimental result**

The conventional experiments of pinhole-type integral imaging are performed only with 3D letter objects in the dark room because of low spatial resolution and brightness [15–20,

30, 43, 44]. In the experiments of the proposed method, I took pictures and watched the reconstructed 3D object in the bright room to show off the advantages which are high brightness and high resolution.

Figure 2.38 shows the experimental result of 3 white letters in the conventional method and proposed method. The experimental results show the different voxel separation and fill-factors in center view of reconstructed 3D image. In the conventional method, the pinhole can express whole color information with interval of pixel size and the color ununiformity problem. However, the proposed method reconstructs 3D image with red, green and blue sub-voxels which are separated in interval of sub-pixel size without color ununiformity problem and fill-factor of proposed method is higher than the case of conventional method.

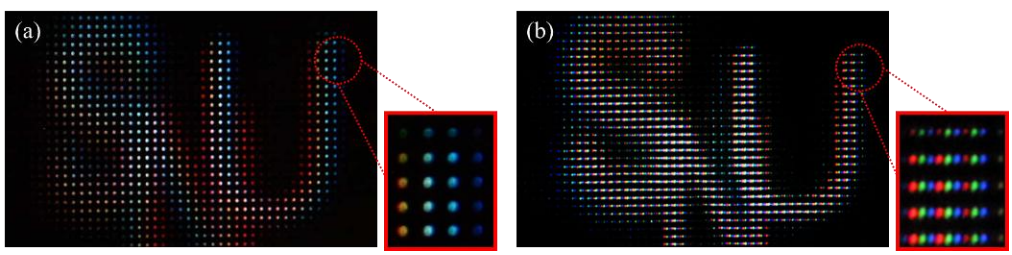

Figure 2.38 Experimental result of 3 white letters in conventional method and proposed method: (a) center view image and magnified voxels of conventional method and (b) proposed method

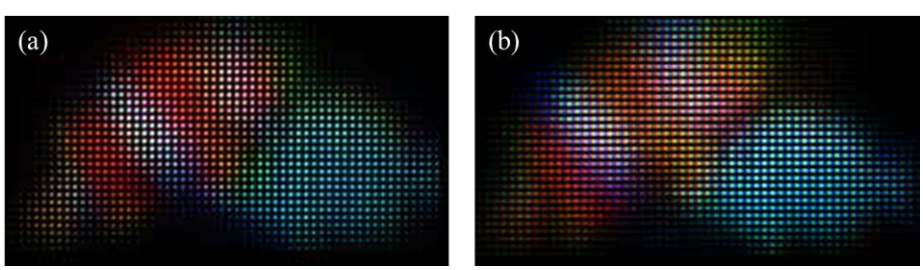

Figure 2.39 Experimental result of high resolution fish objects in conventional method and proposed method: (a) center view image of conventional method and (b) proposed method

Figure 2.39 shows the reconstructed 3D images of high resolution two fishes in the

conventional method and proposed method. The conventional method reconstructs high resolution 3D images using separated voxels whereas the proposed method reconstructs 3D images using red, green and blue sub-voxels with sub-voxel sampling and high fill-factor.

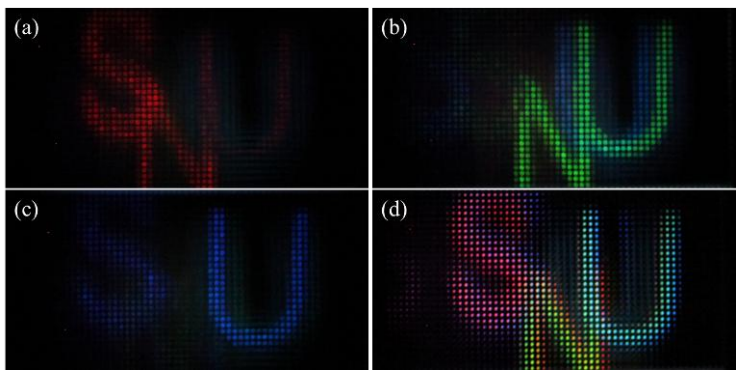

Figure 2.40 Experimental result of proposed method in each color filter pinhole array: (a) Center view image of 3 letters with pink (255, 85, 170), spring grass (170, 255, 85) and sky-blue (85, 170, 255) colors in red color filter pinhole array, (b) green color filter pinhole array, (c) blue color filter pinhole array and (d) all channels of color filter pinhole array

To verify the color filtering of the proposed method, I performed the experiment with pink, spring grass and sky-blue color 3 letters in different depth planes, 30 mm, -20 mm and 10 mm from the color filter pinhole array. The pink color is generated by different 8 bit intensity values, 255 in red channel, 85 in green channel and 170 in blue channel, spring grass color is mixed by 170, 255 and 85 and sky-blue is mixed by 85, 170 and 255. As shown in Figure 2.40, the resolution of reconstructed 3D object in different color channel is the same as the conventional method, whereas the resolution of reconstructed 3D object using all channels of color filter pinhole array is enhanced by 3 times.

The viewing angle of pinhole-type integral imaging is limited by the pinhole specification, whereas the proposed method has additional factor of limitation which is the viewing angle of LCD panel because of the use of color filters and LC layer as pinhole array. To verify the effect of the viewing angle of LCD panel, I used two different types of LCD panels which are TN LCD panel and S-IPS II LCD panel. The viewing

angle of S-IPS II panel is larger than TN LCD panel, 178° by 178° and 120° by 110°. Figure 2.41 shows the experimental results of each panel in different observer positions. As shown in Figure 2.41, the leftmost and rightmost views in S-IPS II panel shows brighter and more vivid 3D images than TN LCD panel case. Therefore, the pinhole type integral imaging based on color filter pinhole array on S-IPS II LCD panel using projection scheme reconstructs the best quality of 3D images in various pinhole-type integral imaging systems. In addition, the proposed method can be easily converted to 2D display with the use of white images on display panel as shown in Figure 2.42.

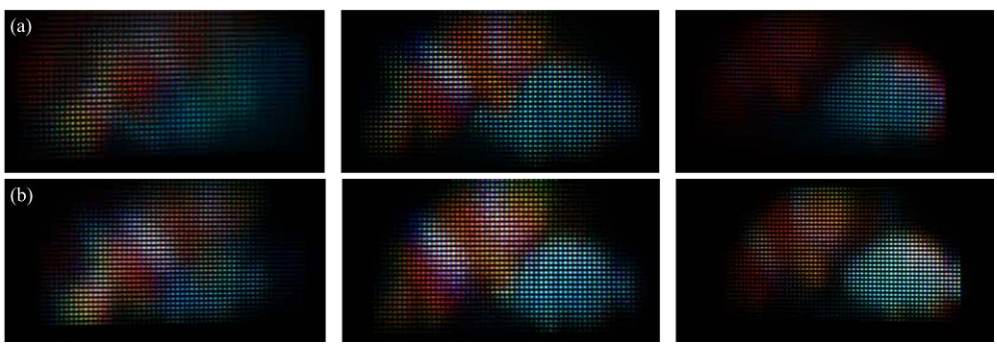

Figure 2.41 Experimental result of comparison of TN LCD and S-IPS II setups at left (-15.45°), center and right (15.45°) view points: (a) perspective view images at different view points on TN LCD setup and (b) S-IPS II LCD setup

Figure 2.42 Experimental result of proposed method in 2D mode

2.3.4 **Conclusion**

I proposed an improvement method of pinhole-type integral imaging using color filter array on display panel and projection scheme. The use of projection scheme leads to the improvement of angular resolution and brightness and the use of color filter pinhole array

on display panel gives the enhancement of spatial resolution, ray density and expressible depth range. To compare with the previous pinhole-type integral imaging systems, the analysis and experiments are performed. The proposed method using S-IPS II panel displays the high quality 3D images in pinhole-type integral imaging in a bright room.

Chapter 3

Analysis and convergence of multi-view display and one-dimensional integral imaging

3.1 Comparison of multi-view display and integral imaging

In 3D display market, autostereoscopic 3D display is regarded as the next-generation display for substituting stereoscopic 3D display without use of glasses. Until recently, many types of autostereoscopic 3D displays have been proposed. Among them, the mainstream of autostereoscopic 3D display is lenticular lens or lens array based method. Multi-view display and integral imaging are almost commercialized autostereocopic 3D display based on lenticular lens and 2D lens array. The components of multi-view display and integral imaging are the display panel for displaying view-images or elemental image and lens array - the same in both systems. However, the sampling methods of each display are different. From the difference of sampling methods, the principles of each display and pickup methods for each method are different, which lead to the different characteristics. In this study, the principles of each methods are presented and the analyses of each display with light field of spatio-angular distribution are performed. In addition, the frequency domain analyses of light field distribution in each display are performed to reveal the relation of two different autostereoscopic displays.

3.1.1 **Principles of multi-view display and one-dimensional integral imaging**

The multi-view display and 1D integral imaging are the leading display technologies in autostereoscopic display and use exactly same optical component for reconstruction of 3D image. Two methods are fundamentally based on the spatial multiplexing of view-images or elemental image on display panel using lens array. However, the principles of two methods have major difference from sampling method in ray space, which brings out different design parameters in same optical components.

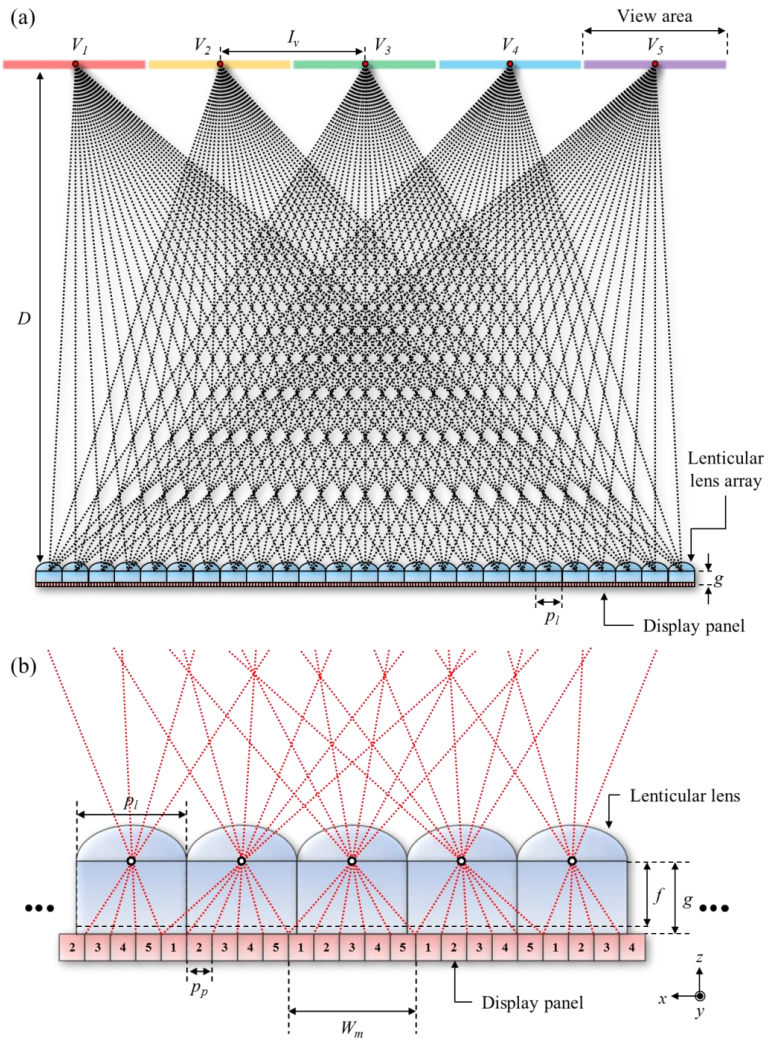

Figure 3.1 Principles of multi-view display in ray distribution: (a) formation of viewpoints in multi-view display and (b) assignment of lenticular lens and view images

In research field in 3D displays, multi-view display is defined as the system in which different view images are converged at finite number of viewpoints as shown in Figure 3.1(a). The number of view images is the same as the number of viewpoints in multi-view display and each view image is spatially multiplexed and converged by lens array from plane of display panel to plane of viewpoints. To converge view image from plane of display panel to viewpoints, the width of view image assigned on each lens W_m has to be larger than pitch of lens p_l as shown in Figure 3.1(b). For example, if multi-view display has 5 viewpoints, each view image is sampled by lenticular lens and separated to the number of lens array pixels which is the resolution of each view, and the portion of interwoven view image on display panel which is assigned at one lenticular lens has 5 pixels as shown in Figure 3.1(b). Therefore, the portion of interwoven view image W_m is the exactly same image which is captured by shift-sensor model camera [12].

To design multi-view display with convergence of viewpoints, two conditions have to be satisfied in the specifications of lens and display panel as shown in Figure 3.2. First, the binocular disparity constraint has to be satisfied by observer distance and display specification as shown in Figure 3.2(a). Each pixel on display panel is magnified to interval of viewpoints by lenticular lens. For the finite viewpoints and uniform arrangement of viewpoints between two eyes, the interval of viewpoint I_v is defined by d_e/k where the interpupillary distance is d_e and the number of views in interpupillary distance is k. From the lens equation and binocular disparity condition, the observer distance and viewpoints are given as

$$\begin{aligned} \frac{1}{f} &= \frac{1}{D} + \frac{1}{g}, \\ \frac{d_e}{kp_p} &= \frac{I_v}{p_p} = \frac{D}{g}, \end{aligned} \tag{3.1}$$

where f is the focal length, g is gap between lens array and display panel, p_p is pixel pitch of display panel and D is observer distance.

The other constraint for designing multi-view display is convergence of viewpoints as shown in Figure 3.2(b). The principal rays of each lens have to be converged at each viewpoints, which are from pixels on interwoven image with fixed interval Np_p. From the

constraint, the relation between *N*-view pixels and lens pitch p_l is derived as follows:

$$\frac{p_l}{Np_p} = \frac{D}{D+g}. \tag{3.2}$$

From Eqs. (3.1) and (3.2), the observer distance and viewpoints are limited by the lens and display specifications as follows:

$$D = \frac{fNp_p}{Np_p - p_l} = \frac{f(I_v + p_p)}{p_p}. \tag{3.3}$$

In multi-view display, the observer distance and viewpoints are fixed and all rays from the display panel are converged to each viewpoint as shown in Eq. (3.3). Therefore, the viewpoints of multi-view display have finite number and fixed position with high resolution and ray density.

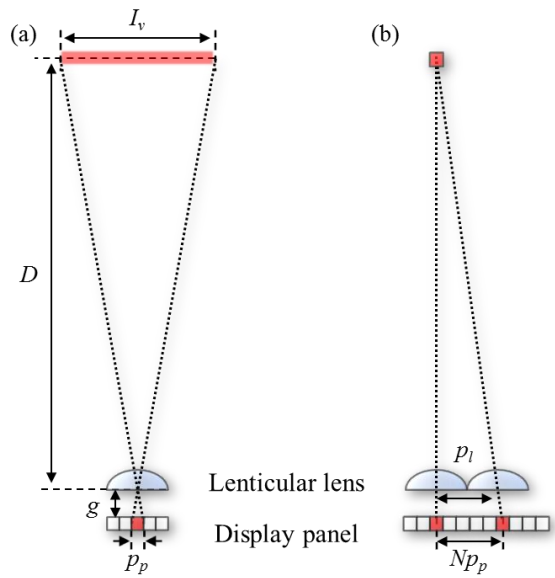

Figure 3.2 Design constraints of multi-view display for fixed viewpoints: (a) constraint between pixel pitch and interval of viewpoints, (b) constraint between *N*-view pixels and lens pitch

On the other hand, 1D integral imaging has different distribution of viewpoints and design parameters as shown in Figure 3.3. Unlike the multi-view display, the rays from

pixels behind the lens array are diverged in viewing angle symmetrically, which is similar to the symmetric-parallel camera model. From the difference of sampling method, integral imaging can form the quasi-continuous viewpoints within viewing angle which depends on observer position. The viewpoint of integral imaging can be reproduced by the observer position and the observer can see the 3D object within viewing angle regardless of observer distance unlike multi-view display. For the symmetric diverging rays in integral imaging, the width of one elemental image region behind one lens array is the same as the width of lens array as shown in Figure 3.3(b). Therefore, the plane of display is magnified and imaged to the central depth plane *D* which is determined by the lens equation as follows:

$$D = \frac{fg}{g - f}. \tag{3.4}$$

The expressible depth range of integral imaging is limited by near the central depth plane *D* within marginal depth plane Δz as follows [10, 81]:

$$\Delta z = \frac{D^2 p_p}{g p_l}. \tag{3.5}$$

From Eqs. (3.4) and (3.5), the expressible depth range in integral imaging has widest range when the gap between lens array and display panel is approximately same as the focal length. In this case of focused mode integral imaging, the resolution of 3D object has lowest quality with the number of lens array. Therefore, integral imaging in focused mode has uniform ray density and quasi-continuous and relatively large numbers of viewpoints within viewing angle.

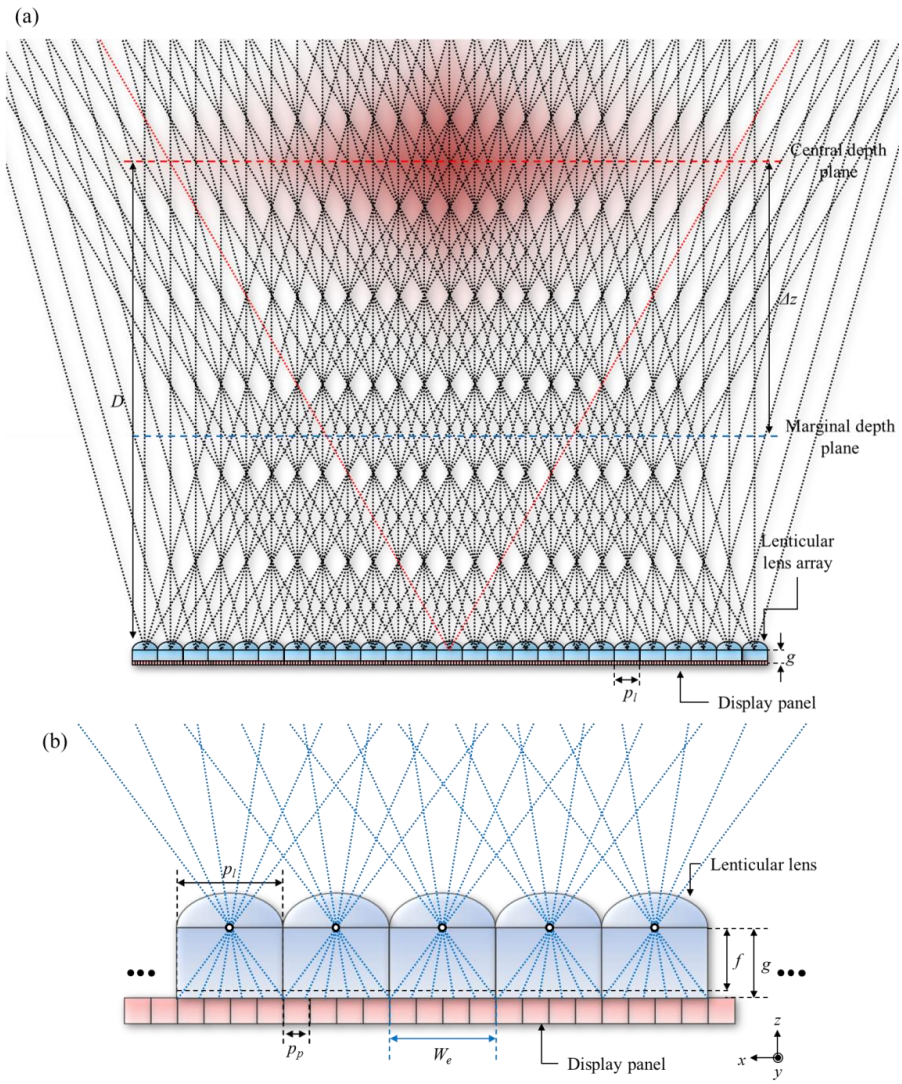

Figure 3.3 Principles of integral imaging in ray distribution: (a) formation of viewpoints in multi-view display and (b) assignment of lenticular lens and elemental image

3.1.2 **Principles of multi-view display and integral imaging in pickup methods**

For autostereoscopic 3D display, the pickup of 3D object process is performed by using multi camera array in perspective view geometry. Generally, the arrangement of multi cameras is classified by 3 types as shown in Figure 3.4 [12]. Figure 3.4(a) shows asymmetric and parallel multi-camera model where each camera is not a normal

perspective view camera but shift sensor model camera. The principal rays are shifted from the center of CCD position and converge to the convergence point of multiple cameras. For multi-view display, 3D objects located between near depth plane D_N and far depth plane D_F are acquired by multiple shift sensor cameras. From the convergence point and depth D_c, the acquired 3D objects will be reconstructed in real and virtual 3D images.

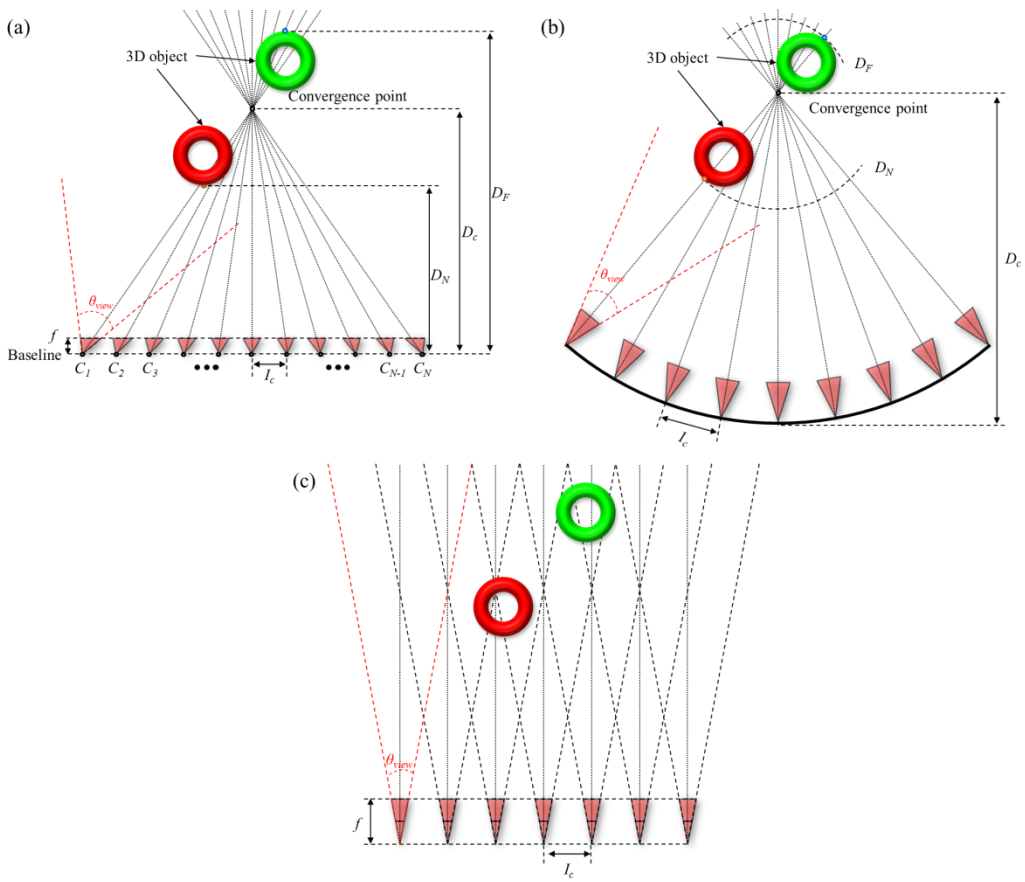

Figure 3.4 Principles of pickup methods in different camera alignments: (a) pickup method of multi-view display, (b) cylindrical display system and (c) integral imaging

Figure 3.4(b) shows the symmetric and circular multi-camera model with near and far depth planes. Each camera is arranged by interval I_c and converged at the center of circle of baselines. This camera model can pickup in circular image plane for cylindrical display model such as 360-degree viewable cylindrical integral imaging system [50, 75,

77]. Figure 3.4(c) shows the symmetric and parallel multi-camera model which enumerate perspective cameras in finite interval I_c with D_N and D_F. This camera model uses same principle of integral imaging.

The pickup and generation of multiple view image are classified to the display device side and viewpoint side by the shooting direction of multiple camera. In pickup process, multi-view display is based on asymmetric-parallel camera model and integral imaging uses symmetric-parallel camera model. Although two display methods use different camera model, shooting direction and baseline of multiple camera can be selected to both viewpoint side and display side.

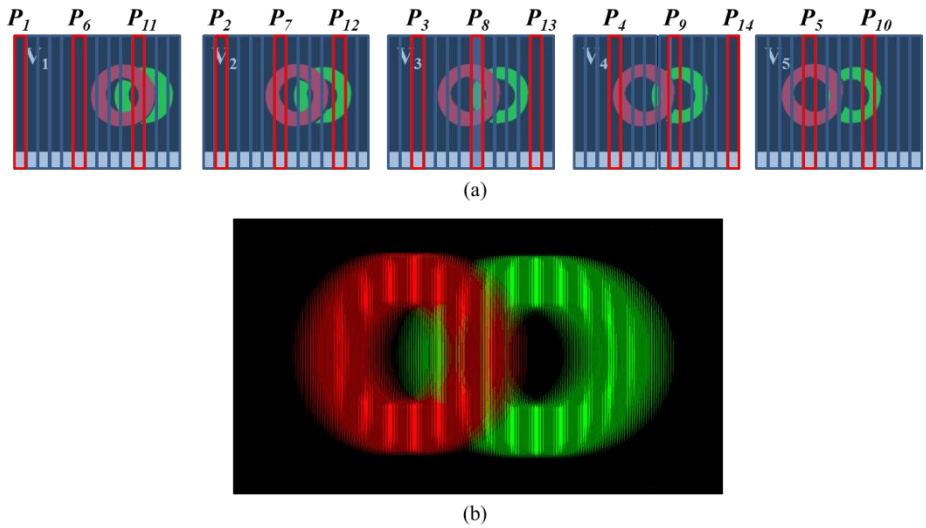

Figure 3.5 Principle of interweaving process of view images in multi-view display: (a) interweaving process in 5-view multi-view display, (b) interwoven view image

In multi-view display, the pickup process is performed in viewpoint side and multiple cameras acquire 3D objects from viewpoints to display panel direction, generally. The baseline of multiple camera is located at the plane of viewpoints and the acquisition is performed to display direction. The number of pickup cameras is the same as the number of viewpoints in multi-view display and each camera is shift-sensor model camera with the resolution of the number for lenses in the lens array. After acquisition to multiple images, the multi-view images are interwoven as shown in Figure 3.5. In the pickup with viewpoint to display panel direction, the acquired 3D information and

observed 3D information are the same direction, which prevents the pseudoscopic problem because of the same shooting direction of pickup and display.

In rare case, the pickup of 3D object in multi-view display can be performed with display to viewpoint direction. In this case of pickup, the baseline of multiple cameras is located at the plane of display panel, and the number of multiple cameras is the same as the number of lenses in an array and the resolution of acquired image is the same as the number of viewpoints. The pseudoscopic problem also occurs from different direction between shooting and display. Therefore, 3D objects are easily captured by lens array and one CCD with shift sensor model although the pseudoscopic problem occurs in the acquisition with display to viewpoint direction.

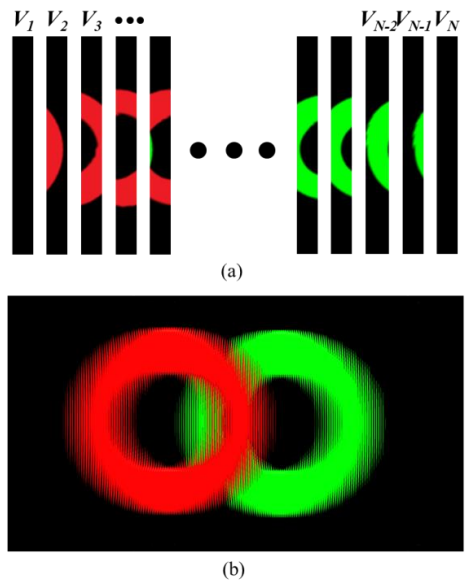

Figure 3.6 Principle of pickup images and elemental image: (a) each view image from lens, (b) elemental image

In integral imaging, the 3D object is generally acquired from display panel to viewpoint direction with symmetric-parallel model. The baseline of multiple cameras is located at the plane of display panel and the shooting is performed to viewpoint direction. In this case of pickup, the number of lenses in an array is the same as the number of multiple cameras and the resolution of elemental image determines the viewing angle of integral imaging. To simplify the pickup process, the lens array and CCD model are used

for pickup process instead of multiple cameras. However, the pseudoscopic problem is inevitable in this case of pickup. As shown in Figure 3.6, the multiple cameras with symmetric-parallel arrangement capture the 3D objects in perspective view geometry, and the array of captured perspective views is elemental image in integral imaging.

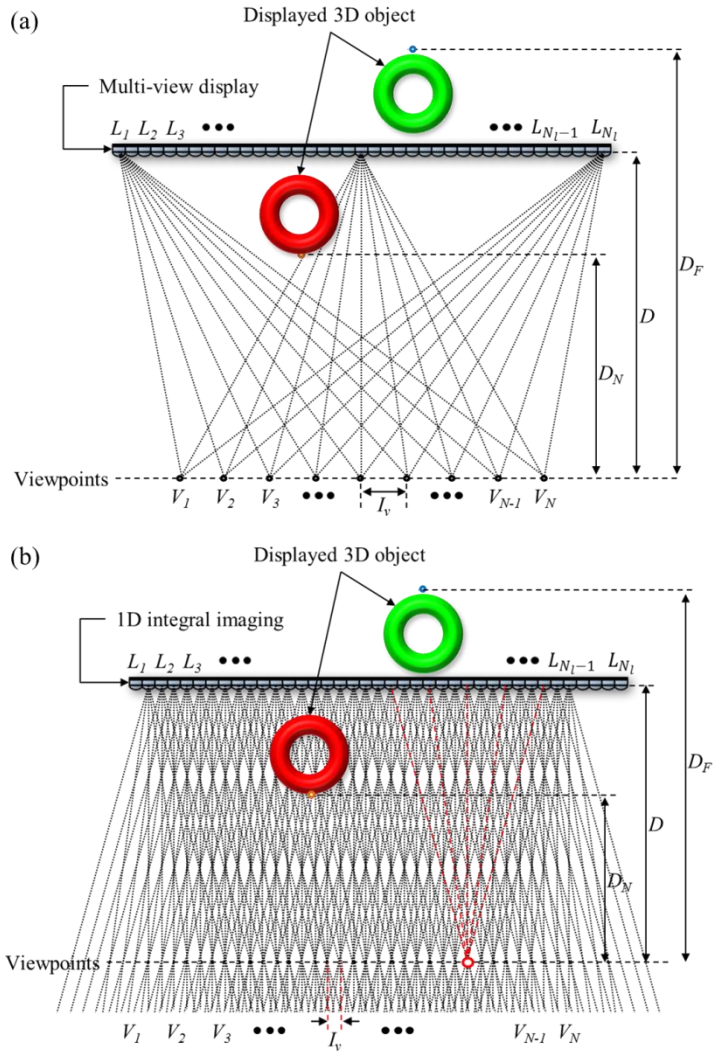

Figure 3.7 Formation of viewpoint in integral imaging and multi-view display: (a) multi-view display and (b) integral imaging

As the above-mentioned multi-view display, the pickup process in integral imaging is also performed in the opposite direction and location of baseline of multiple cameras.

The pickup of 3D objects using multiple cameras at the baseline of viewpoint plane is more complicated than the case of pickup in multi-view display from viewpoint plane to display plane.

Figure 3.7 shows the difference between pickup process of multi-view display and integral imaging using multiple cameras located in the plane of viewpoints. From the multiplexing of lens array, the acquired view images have to be subject to interweaving process in the pickup from the plane of viewpoints to display panel. Although this case of pick up needs additional interweaving process, this case of pickup can prevent the pseudoscopic problem in both multi-view display and integral imaging. In the case of multi-view display, the multi-view images of finite number are interwoven to whole plane of display panel. However, the case of integral imaging is more complicated than multi-view case because of limited viewing angle and quasi-infinite viewpoints.

As shown in Figure 3.7(b), the nearest convergence points in front of lens array is limited by the viewing angle of lens array. The depth plane limited by the viewing angle is formed with quantization number k as follows:

$$D_k = kfn_e, \tag{3.6}$$

where the focal length is f and the number of pixels in one elemental image region is n_e.

The number of viewpoints in each quantized depth plane N_k in N_l lens array is derived as follows:

$$N_k = N_l - 2k\lfloor n_e / 2 \rfloor, \tag{3.7}$$

where $\lfloor x \rfloor$ is floor function of x. As shown in Figure 3.7(b), the pickup at k-th depth plane using N_k cameras is performed and then the interweaving process should be operated. However, the interweaving process for integral imaging is different from the case of multi-view display, which has to be interweaved in limited range of lens array as follows:

$$n - k\lfloor n_e / 2 \rfloor \le n \le n + k\lfloor n_e / 2 \rfloor, \tag{3.8}$$

where the pickup is performed in k-th depth plane and n-th camera and the interweaving

processing is performed with interval *k*.

3.1.3 **Analysis of multi-view display and integral imaging in light filed**

From the above-sections, the multi-view display and integral imaging have various differences in display and pickup principles. To reveal the difference in view of spatio-angular distribution, the light field analysis is performed in this section. For a scene composed of structures significantly larger than the shortest wavelength of illumination, the distribution of light can be well-characterized by measuring the intensity of every optical ray within a 3D volume [80]. The radiance of every ray passing through any point within a 3D volume is quantified by the 5D plenoptic function [36, 82–84]. When the observer is ristricted to move outside the convex hull of an object, the 5D plenoptic function is reduced to 4D plenoptic function (*u*, *v*, *s*, *t*). The 4D light field is composed of position parameter (*u*, *v*) and direction parameters (*s*, *t*).

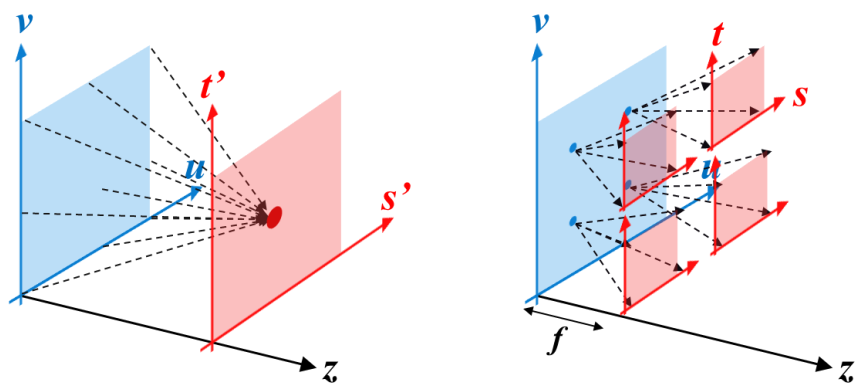

(a) (b)

Figure 3.8 Ray space analysis based on light filed: (a) ray space analysis of two-plane parameterization and (b) plane and direction parameterization

Figure 3.8 shows the two different kinds of parameterization of 4D light field [85, 86]. As shown in Figure 3.8(a), two plane parameterization is based on two different planes with the initial ray position on *uv*-plane and destination ray position on s′*t*′-plane. On the other hand, the plane and direction parameterization represents light field to initial position and relative position from initial position which can be depicted by angular

direction with paraxial approximation in unit distance. As shown in Figure 3.9, two different parameterizations are converted each other in following relation.

$$
\begin{aligned}
s' &= u + \frac{zs}{f}, \\
t' &= v + \frac{zt}{f}, \\
s &= f \tan\theta.
\end{aligned}
\tag{3.9}
$$

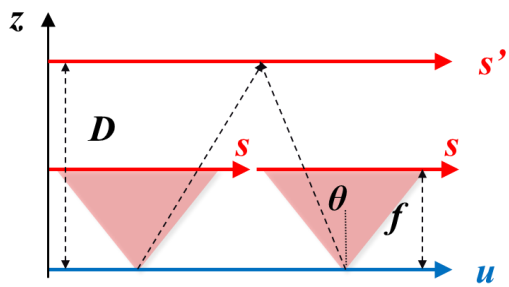

Figure 3.9 Relation between plane and direction parameterization and two plane parameterization

Table 3.1 Specification of simulation setup

Setup	Specification	Characteristic
Object 1	Size	200 by 100
	Depth	10 mm
	Pixel pitch	0.13 mm
Object 2	Size	200 by 100
	Resolution	50 mm
	Pixel pitch	0.13 mm
Multi-view display	Lens pitch	1 mm
	Focal length	3.8 mm
	Number of lens	400
	Number of views	8
	View interval	3.25 mm
	Viewing distance	98.8 mm
1D integral imaging	Lens pitch	1 mm
	Focal length	3.8 mm
	Number of lens	400

To analyze the multi-view display and integral imaging, the light field distributions of multi-view display and integral imaging are performed in plane and direction parameterization for spatio-angular distribution. Figure 3.10 shows the experimental setups for light field analysis in multi-view display and integral imaging. The two textured box objects are located at different depth planes d_1 and d_2 with u directional offset. Table 3.1 shows the specification of simulation setup. In this simulation, the analyses are based on the different sampling method of multi-view display and integral imaging.

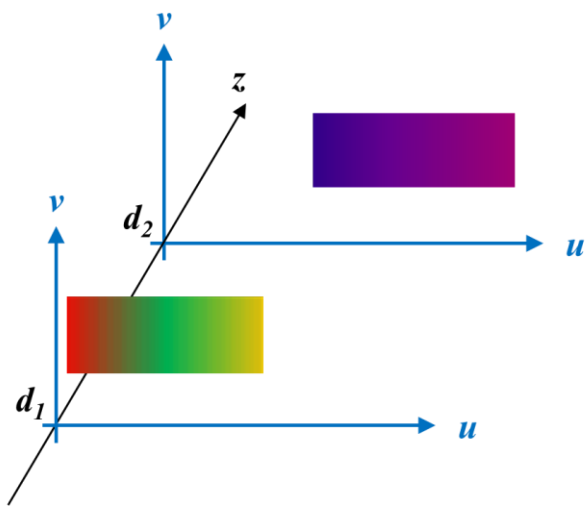

Figure 3.10 Simulation setup for light field distributions of multi-view and integral imaging

As shown in Figure 3.11, the light filed distributions of multi-view display and integral imaging are represented by the initial points of rays on u axis and directions on the focal plane of lens array. In the case of multi-view display, the direction of rays is gradually changed from positive to negative values as shown in Figure 3.11(a). On the other hand, the direction of rays in integral imaging is fixed to the viewing angle of lens array as shown in Figure 3.11(b). To compare the difference of light field in each method, spatio-angular distribution is represented with initial point on u axis and diverging angle on focal plane θ as shown in Figure 3.12.

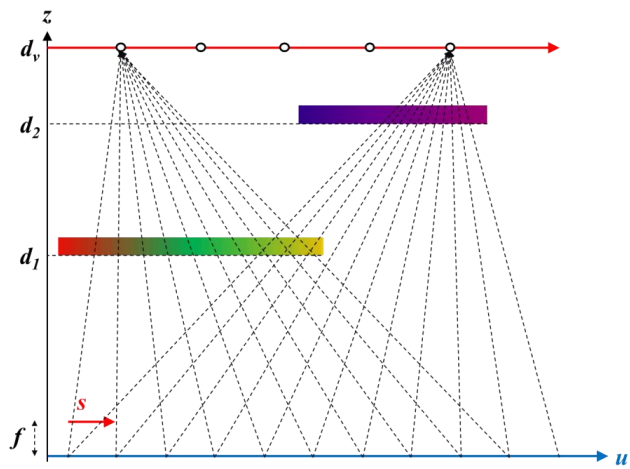

(a)

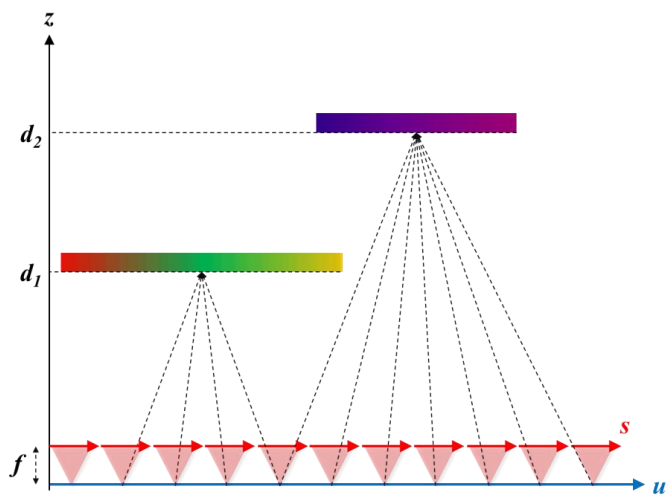

(b)

Figure 3.11 Sampling principles in multi-view display and integral imaging: (a) light field distribution of multi-view display and (b) integral imaging

If the number of viewpoints is plenty big enough to sample 3D object in wide-viewing angle, the distribution of light fields can express the relation between the angular and spatial ray distributions all over the ranges of 3D object. As shown in Figure 3.12(a), the radiance of 3D objects located in different depth planes is distributed to spatio-angular space with different slopes. The slopes of distribution in object side is the same as the

inverse of depth of object. In addition, the slope of upper boundary black dashed line is the same as the shift angle of multi-view display following lens position. In actual multi-view display system, 3D objects are sampled by interval of lens pitch in *u* direction and the distribution is cut in small pieces as shown in Figure 3.12(b).

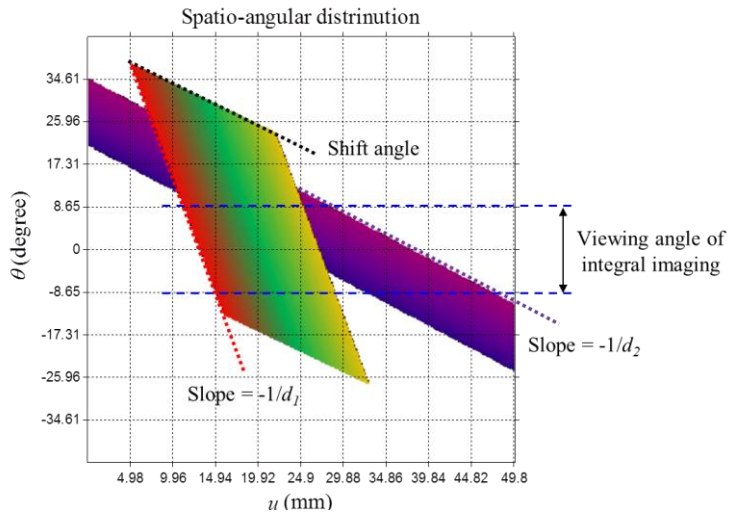

(a)

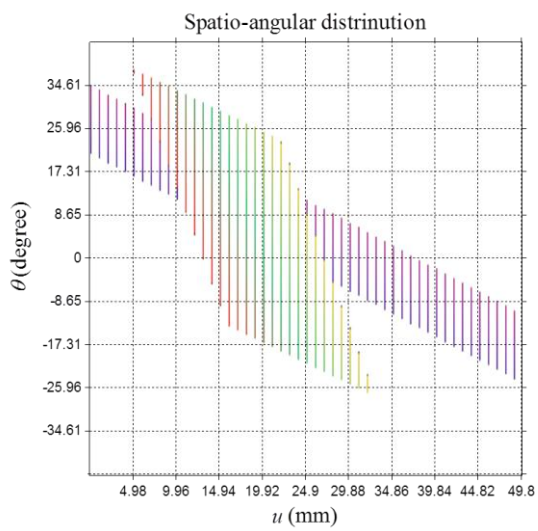

(b)

Figure 3.12 Light field distribution of multi-view display: (a) spatio-angular distribution of multi-view display with infinite sampling frequency and (b) with sampling in 1 mm lens array

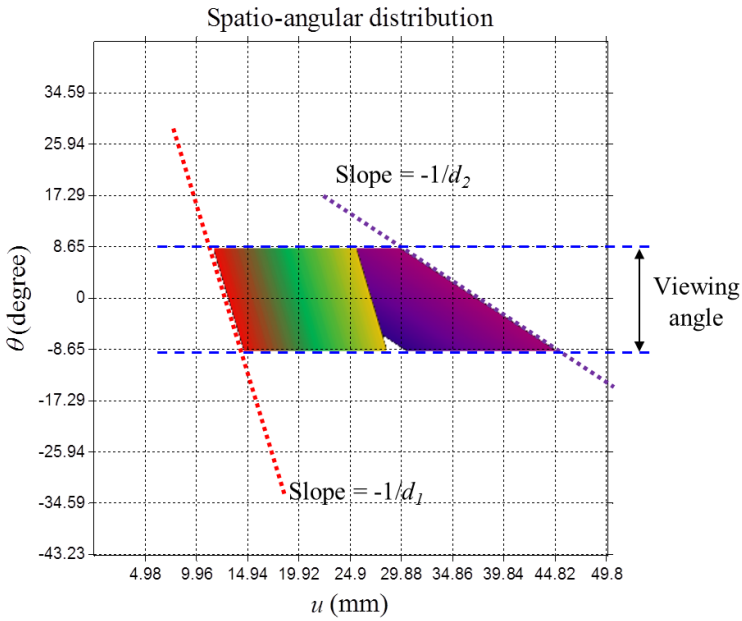

(a)

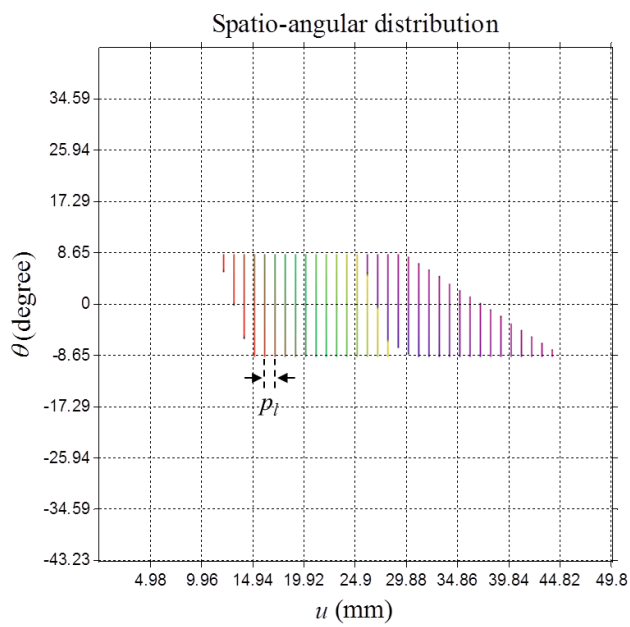

(b)

Figure 3.13 Light field distribution of integral imaging: (a) spatio-angular distribution of integral imaging with infinite sampling frequency and (b) with sampling in 1 mm lens array

In the distribution of multi-view display, the distribution of integral imaging can be expressed by limited viewing angle of integral imaging as shown in Figure 3.13. Integral imaging has the same range of diverging angle in different u position. Therefore, the slope of shift angle is parallel, which means the principle of integral imaging is symmetry-parallel mode. The sampling result of integral imaging with 1 mm lens array is shown in Figure 3.13(b).

From the spatio-angular distribution of multi-view display and integral imaging, the depth of 3D objects, shift angle and display range of 3D display can be analyzed as shown in Figure 3.12 and Figure 3.13. The analysis of spatio-angular distribution in multi-view display and integral imaging is performed to reveal the difference of each display. Figure 3.14 shows the result of Fourier transform of spatio-angular distribution. In the case of multi-view display, the magnitude of 2D Fourier transform is concentrated in two 3D objects as shown in Figure 3.14(a). However, the limitation of viewing angle in integral imaging gives high magnitude of perpendicular components. In addition, the magnitude of spectrum of 3D object located in far plane is relatively low in integral imaging as shown in Figure 3.14(b).

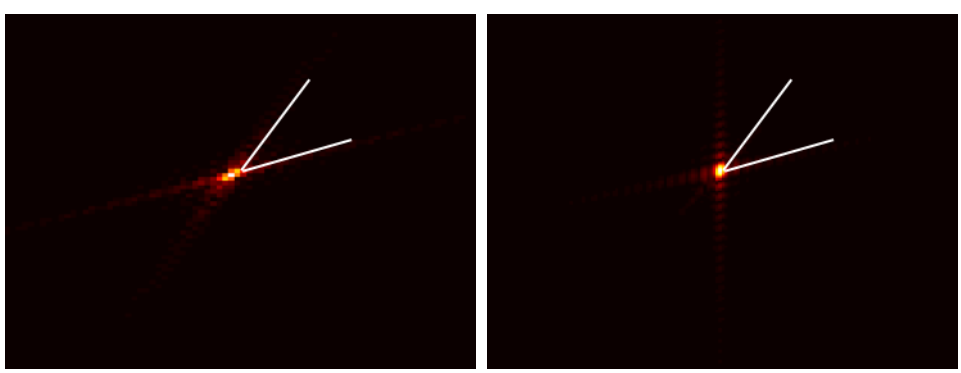

(a) (b)

Figure 3.14 Frequency domain analysis of multi-view display and integral imaging: (a) multi-view display and (b) integral imaging

3.2 Computational reacquisition of a real three-dimensional object for integral imaging without matching of pickup and display lens array

Computational reacquisition for real 3D object in integral imaging is proposed. The pseudoscopic problem and matching of lens array in pickup and display are fundamental problems for real-time broadcasting based on integral imaging. I propose the reconstruction method of real 3D object and computational reacquisition method without matching of pickup and display lens array. In reconstruction, the real 3D object is reconstructed with volumetric information using depth extraction and triangular mesh, which can be rotated and translated in orthoscopic geometry. In reacquisition, the virtual lens array can generate the elemental image without matching of pickup lens array using OpenGL.

3.2.1 Introduction

The research field of 3D technologies is considerably widened from 3D display to various applications. Among them, integral imaging and its applications are remarkable methods to acquire and display a volumetric 3D object with full parallax [21, 26, 35, 38]. However, integral imaging has fundamental issues between acquisition and display phase, which are the pseudoscopic problem and matching of lens specification in pickup and display phase [26]. The depth information of real object is reversed between pickup and display phase because of the direction of rays in acquisition and display phase. It is called the pseudoscopic problem. In addition, the lens array used in display phase has to be matched with pickup lens array for reconstructing 3D object without flipping.

In this study, I propose the computational reacquisition method to overcome the pseudoscopic and matching problem between acquisition and display phase. First, the depth information of real object is extracted with high precision using optical flows of sub-images. To reconstruct the volumetric 3D object with reversal of depth information, I adopt the triangular mesh reconstruction between point clouds in virtual space. After reconstruction, the real 3D object can be captured in orthoscopic geometry using OpenGL, which can be rotated and translated in reacquisition process. Furthermore, the

reacquisition process can generate the elemental image without matching of pickup lens array. In this study, I present the experimental results of pickup, reconstruction, reacquisition, and display with various specification of lens array. The proposed method can help to broadcast 3D contents using integral imaging.

3.2.2 Depth extraction and triangular mesh reconstruction from sub-images using optical flow

In integral imaging, the conversion of pseudoscopic to orthoscopic image and accurate depth extraction are crucial issues [21, 26, 35]. Many research groups have proposed conversion and extraction methods based on the all optical principles or optical information processing algorithms [26, 35]. In this study, I focus on the optical information processing method for depth extraction and reconstruction from elemental image of integral imaging. The proposed method is reacquisition of reconstructed 3D object which is depth-reversed after the depth extraction process to avoid the pseudoscopic problem. Figure 3.15 shows the whole process of the proposed method.

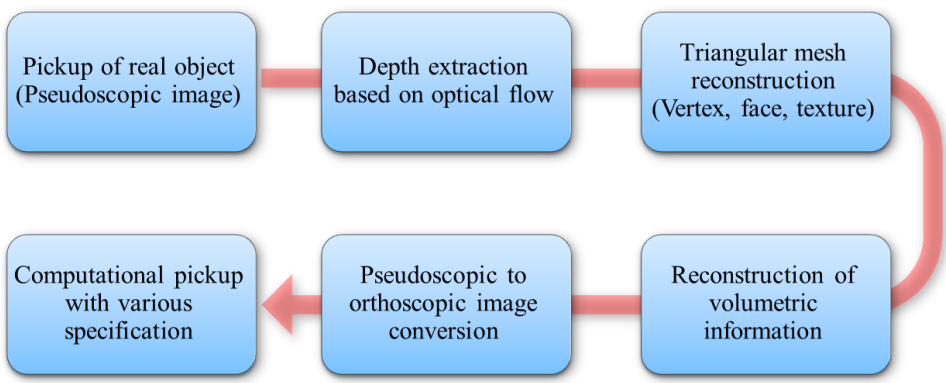

Figure 3.15. Procedure of the proposed method

First, elemental image of real 3D object is generated by capturing 3D information using a CCD or other optical pickup devices with p_p pixel pitch and a lens array with focal length f and lens pitch p_l as shown in Figure 3.16. After acquisition of 3D information, the elemental image has to be rectified with rectification algorithm to reduce distortion from geometry and aberration [38]. To reverse the acquired 3D information, I

extract the accurate depth information from rectified elemental image using optical flow [21]. Optical flow between sub-images which are generated by the pixel remapping of elemental image can extract the depth information with sub-image resolution.

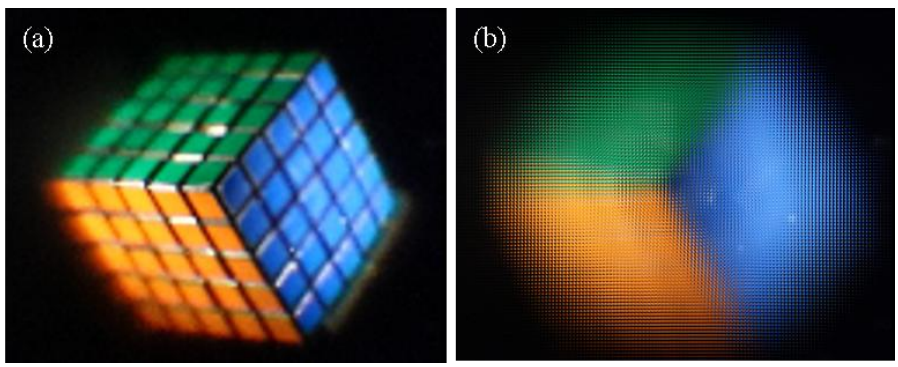

Figure 3.16 Acquisition of real 3D object: (a) real object, (b) captured elemental image with rectification algorithm

After calculation of optical flow between sub-images, the depth map of center sub-image is defined by the average of optical flows from sub-images in horizontal and vertical directions. The extracted depth of pixel (x, y) is defined by

$$D_{OF(p_c,q_c)}(x,y) = \frac{fp_l}{2p_p}\left[\frac{1}{n_x-1}\sum_{p=1}^{n_x}\left|\frac{u_{(p_c,q_c),(p,q_c)}(x,y)}{p_c-p}\right|+\frac{1}{n_y-1}\sum_{q=1}^{n_y}\left|\frac{v_{(p_c,q_c),(p_c,q)}(x,y)}{q_c-q}\right|\right], \quad (3.10)$$

where $u_{(p_1,q_1),(p_2,q_2)}(x,y)$ and $v_{(p_1,q_1),(p_2,q_2)}(x,y)$ denote the horizontal and vertical components of optical flow between (p_1, q_1)th and (p_2, q_2)th sub-images at pixel (x, y), and (p_c, q_c)th sub-image is the center sub-image in n_x by n_y sub-image array. To enhance the resolution of extracted depth map, the calculation of optical flows in different viewpoints is performed and averaged on center viewpoint. Figure 3.17 shows the extracted depth map using optical flows between sub-images and point cloud information from extracted depth map. The extracted depth map is generated by the projection of extracted depth map from viewpoints different from center viewpoint. Therefore, each depth information consists of point cloud information which has coordinates of point and color information with red, green and blue channels.

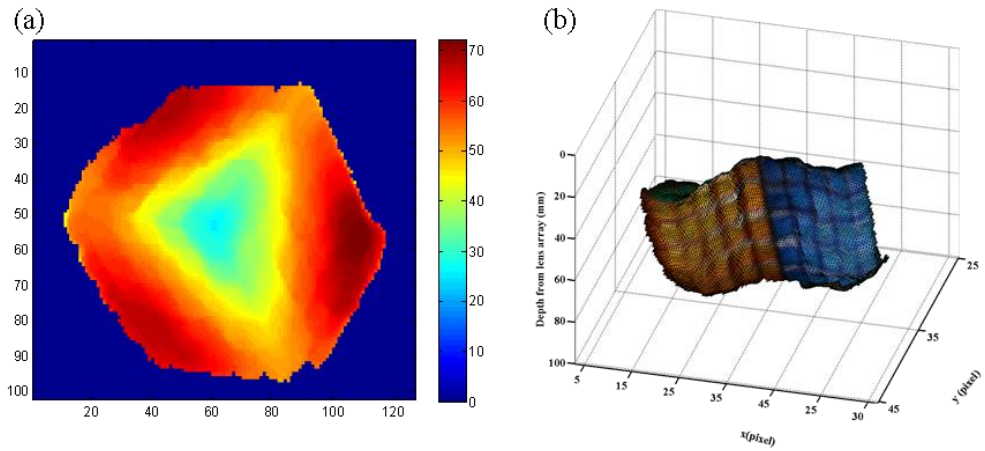

Figure 3.17 Depth extraction from sub-images using optical flow: (a) extracted depth map, (b) point clouds reconstruction of real 3D object

3.2.3 **Conversion from point cloud to face texture information**

The extracted depth information from sub-image array has coordinates of point and color information in point clouds format. To resolve the pseudoscopic problem between pickup and display process, the extracted depth is reversed from the object-to-lens direction to the lens-to-object direction. After depth reverse process, the point cloud information of 3D object is converted to face texture information for computational reacquisition as shown in Figure 3.18.

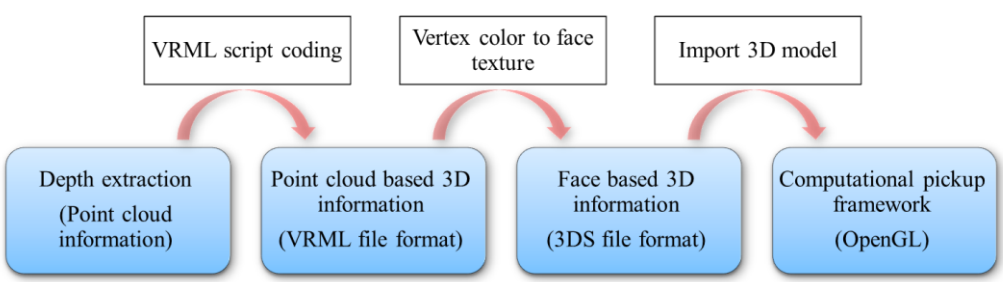

Figure 3.18 Preprocessing of reacquisition of reconstructed 3D object

For computational reacquisition, I reconstruct the 3D object using the triangular mesh reconstruction which consists of vertices, edges and face color as shown in Figure 3.19. In this study, I construct the computational pickup framework using OpenGL, which can import the face based 3D information. Therefore, the point cloud based 3D

information has to be converted to face based 3D information. The point cloud based 3D information is coded by virtual reality modeling language (VRML) which consists of vertices, edges and point color.

The vertex of triangular mesh representation is coordinates of point clouds (x, y, z) and edge is determined by the linked line between two different vertices. The face of triangular mesh representation is index of three vertices for one triangle. For example, the vertices of reconstructed 3D object are 1 to 6 point clouds, which make 4 different faces *a*, *b*, *c* and *d* as shown in Figure 3.19(a). In VRML script, the color information is the same as the red, green and blue channels of each position of point clouds. However, the color information of face based 3D format is represented by the face color which is determined by colors of three vertices in face triangle. In this study, I convert VRML script to 3DS file format for representing 3D object with face based information. Figure 3.19(b) shows the result of converted face based 3D information.

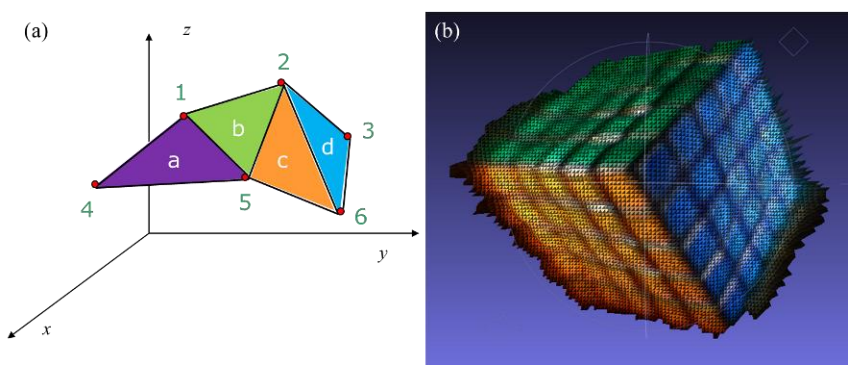

Figure 3.19 Triangular mesh representation: (a) concept of triangular mesh representation, (b) face based triangular mesh representation

After reconstruction of real 3D object with face based 3D information, computational reacquisition framework using OpenGL captures the orthographic model of real 3D object which is imported from triangular mesh representation with face based model to elemental image with different pickup specification. Figure 3.20 shows the computational pickup framework for reacquisition of 3D object using OpenGL which shows the reconstructed 3D model and generates the elemental image. The reconstructed 3D object can be rescaled and shifted by computational pickup framework. In addition, the specification of pixel pitch, focal length and lens pitch can be easily changed.

Therefore, the proposed method can generate the orthoscopic elemental image of real 3D object without limitation of pickup and display specification.

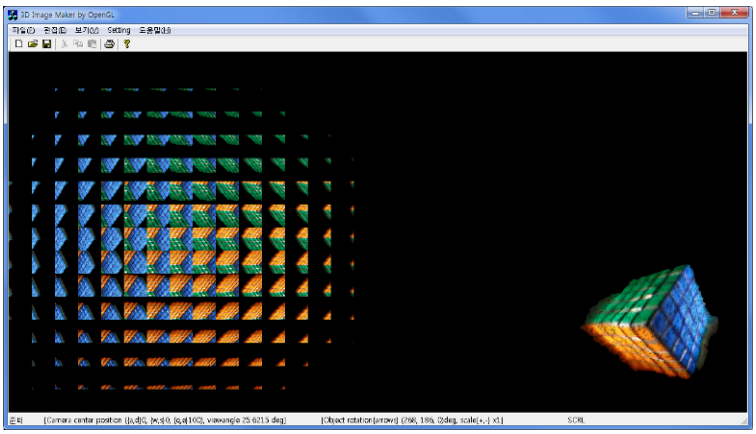

Figure 3.20 Computational pickup framework for reacquisition of 3D object using OpenGL

3.2.4 **Experimental result**

To verify the feasibility of proposed method, I performed experiments with real 3D pickup framework. I used Canon 5D Mark II digital single-lens reflex camera with 28-135 mm lens as pickup device. The experiments are performed with different pickup and display lens specifications. In pickup process, the lens array with 1 mm by 1mm lens pitch and 3.3 mm focal length is used for acquiring the elemental image. The 5 by 5 cube is used for target 3D object which has 80 mm by 80 mm size and is located 30 mm in front of lens array. After pickup scheme, the elemental image is rectified and the depth information is extracted by using optical flow algorithm as shown in Figure 3.21(a) and (b). Figure 3.21(c) shows the reconstructed 3D object with face based triangular mesh representation which is imported to the computational reacquisition framework.

To verify the advantage of reacquisition process, I generate the orthoscopic elemental image based on the reconstructed 3D object with different lens specification and central depth plane (CDP). I set the lens pitch of display phase to 10 mm by 10 mm with 22 mm focal length and CDP is set to 80 mm for real mode and -80 mm for virtual mode. As shown in Figure 3.22, the elemental image of reconstructed 3D object is generated and the 3D images are displayed by using the proposed method with different

specification of lens array.

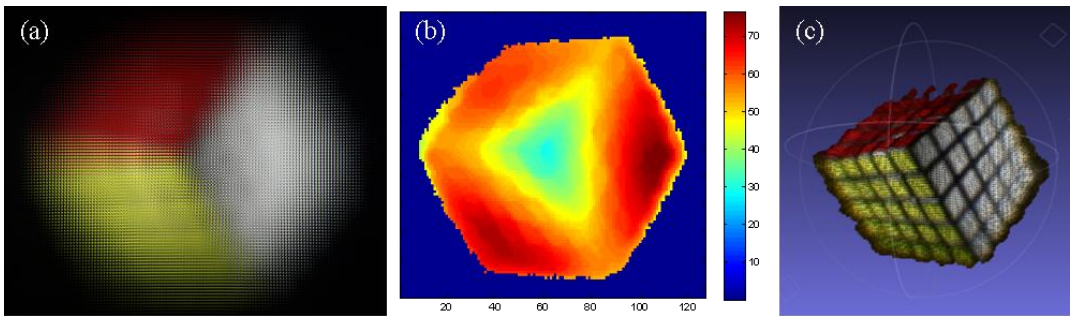

Figure 3.21 Experimental result of depth extraction and triangular mesh reconstruction: (a) captured real 3D object, (b) extracted depth map, (c) reconstructed 3D object using triangular mesh reconstruction

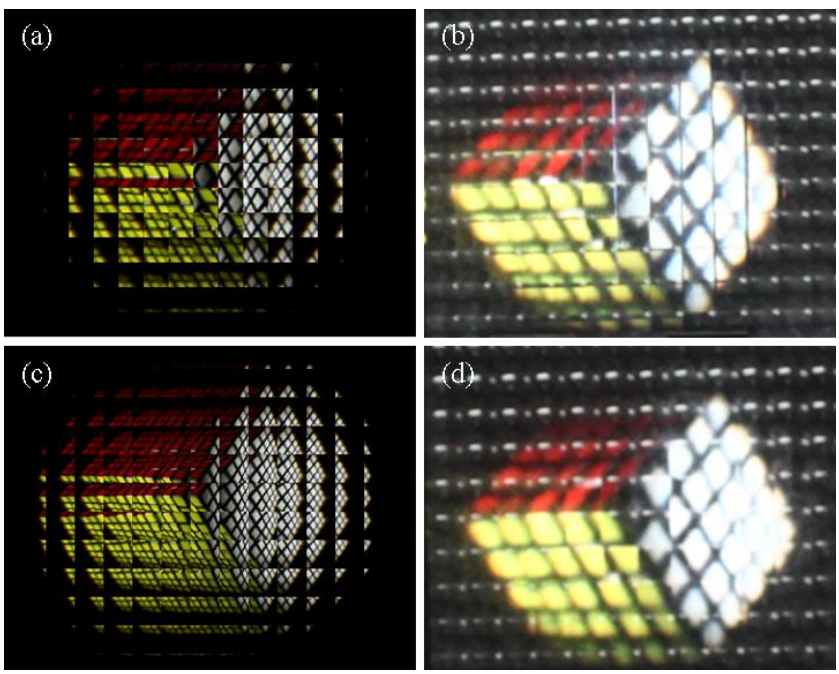

Figure 3.22 Experimental results of reacquisition with different CDPs (10 mm by 10 mm lens, f = 22 mm): (a) elemental image with 80 mm CDP, (b) reconstructed 3D object with real mode, (c) elemental image with -80 mm CDP, (d) reconstructed 3D object with virtual mode

In addition, I generate the elemental image with different scale of real 3D object

using the proposed method. For experiments for different object scale, I set the lens pitch of display phase to 5 mm by 5 mm with 30 mm focal length and change the scale of 3D object from 1 to 1/2. Figure 3.23 shows the generated elemental image and experimental result with different object scale. In conventional method, the 3D object scale cannot be changed and shifted. Therefore, the advantages of the proposed method are verified by the experiments with different lens specification, CDP and object scale.

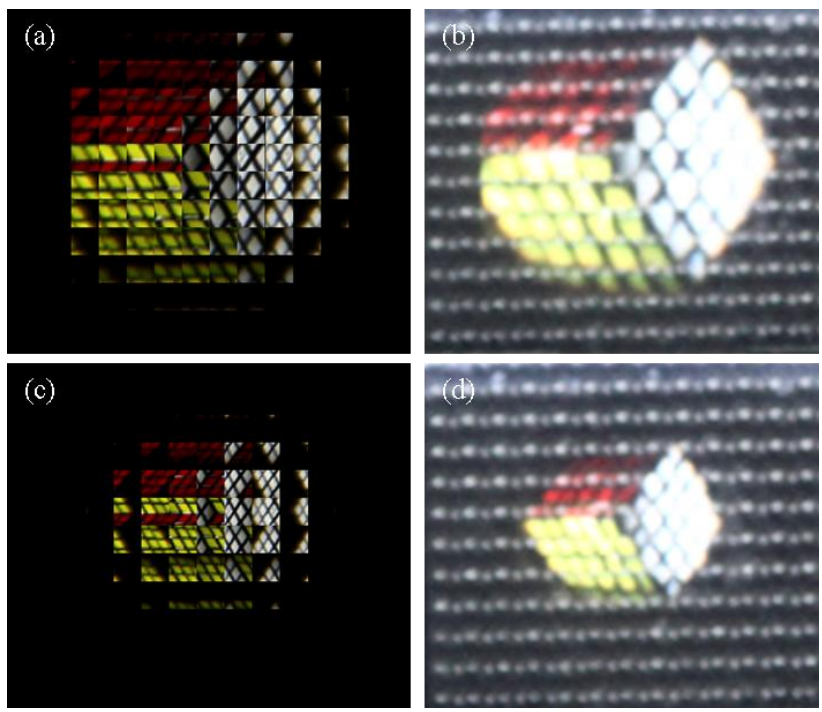

Figure 3.23 Experimental results of reacquisition with different object scale (5 mm by 5 mm lens, f = 30 mm, CDP = 80 mm): (a) elemental image with initial scale, (b) reconstructed 3D object, (c) elemental image with 1/2 scale, (d) reconstructed 3D object with 1/2 scale

3.2.5 **Conclusion**

In this study, I propose the computational reacquisition method of a real 3D object for integral imaging without matching of pickup and display lens array. The conventional pickup and display method in integral imaging has the pseudoscopic problem and the limitation of lens specification for matching display and pickup phase. The proposed

method can generate the orthoscopic elemental image without matching of pickup and display lens array using the depth extraction, triangular mesh representation and computational reacquisition framework. In addition, the proposed method can generate the orthographic elemental image without the limitation of object scale and position.

3.3 Time-multiplexing and sub-pixel mapping of multi-view display and integral imaging

In recent years, autostereoscopic type 3D display has been researched as advanced 3D display instead of stereoscopic type 3D display [8]. Autostereoscopic type 3D display is categorized to the multi-view display and integral imaging by the sampling method in ray space. Generally, the multi-view display is composed of lenticular lens array and display panel for generating the horizontal parallax. The 3D object reconstructed by the multi-view display can be observed at the fixed viewpoints with high ray density.

The other autostereoscopic type 3D display is integral imaging which was invented by Lippmann in 1908 [4]. The component of integral imaging is the same as the multi-view display except the 2D lens array. From the use of 2D lens array, integral imaging can reconstruct the 3D object with full parallax. Nowadays, 1D integral imaging, the simplified scheme of integral imaging using lenticular lens, is researched by many groups with horizontal parallax only mode.

The multi-view display and 1D integral imaging use the same optical devices for reconstructing 3D object except the sampling of 3D images in ray space. The reconstructed 3D object in multi-view display is generated at the viewpoint based on the observer position, whereas integral imaging is based on the 3D object position. From the difference of sampling methods, the multi-view display has fixed and finite viewpoints while integral imaging has quasi-continuous viewpoints. On the other hand, the quality of reconstructed 3D object in multi-view display is better than integral imaging.

To combine the advantage of multi-view display and integral imaging, I propose the convergence type of 3D display based on multi-view display and 1D integral imaging. The multi-view display and 1D integral imaging use the same optical components except the method of ray sampling. The ray density of multi-view display is non-uniform and focused on each viewpoint, whereas the 1D integral imaging has uniform ray density. To enhance the quality of reconstructed 3D image, the principles of multi-view display and 1D integral imaging are analyzed by quality function and combined using time-multiplexing technique in fast response display panel and sub-pixel mapping methods in high resolution display panel.

3.3.1 **Design parameters of multi-view display and integral imaging**

Figure 3.24 shows the principle of the multi-view display and 1D integral imaging in ray space. Two methods share the lenticular lens and display panel with gap t close to the focal length. However, two methods use different ray sampling criteria that the multi-view display sets the viewpoints from the specification lens and pixel pitch of display panel and integral imaging samples the rays uniformly. To determine the optimized observer distance D and gap g, the parameters of the multi-view display are derived as follows:

$$D = \frac{fNp_p}{Np_p - p_l}, \quad I_v = \frac{p_p(D-f)}{f}, \quad g = \frac{Dp_p}{I_v}, \tag{3.11}$$

where the interval between viewpoints is I_v, lens pitch and pixel pitch are p_l and p_p, the focal length of lens is f and the number of views is N. In the proposed method, the multi-view display and integral imaging share the optical setup with different ray sampling methods in two phases of time-multiplexing technique using high refresh rate display panel. Therefore, the observer distance D and gap g are affected to integral imaging principles. From Eq. (3.11), the gap between lens array and display panel is determined to near the focal length of lens array, and the principle of integral imaging can be assumed to the focal mode integral imaging [11]. Consequently, I combine two types of autostereoscopic 3D display using time-multiplexing in same optical setup.

As shown in Figure 3.24, the elemental image region W_e is the same as the lens pitch p_l in the case of integral imaging, and view-image region has to be larger than lens pitch for converging viewpoints in the case of multi-view display. In the proposed method, the display panel has to show the elemental image set and view-images with different pixel borders. Therefore, the correction method for mismatching error between pixel and lens array is needed using weighted sum of intensities in border pixels [87].

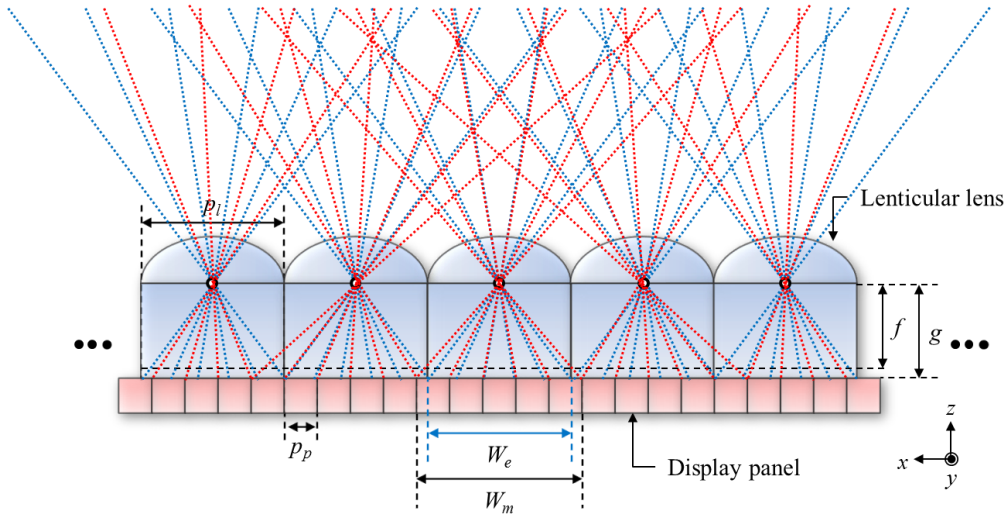

Figure 3.24 Comparison of multi-view display and integral imaging in same optical components

3.3.2 **Convergence type of autostereoscopic display using time-multiplexing or sub-pixel mapping of multi-view display and one-dimensional integral imaging**

To combine different ray sampling method in same optical setup, I use the computational pickup process. In the case of multi-view display, the number of views is the same as the number of pixels behind the lens array and each view-image has perspective views. In the case of integral imaging, each elemental image is perspective view geometry and the number of elemental image is the same as the total pixels per the number of pixels behind lens. These two different multi-view images and elemental image have to display on the same optical devices. To correct the border pixels, I adopt the mismatching error correction method based on the weighted sum algorithm [87]. To multiplex multi-view images and elemental image, the proposed method multiplexes multi-view image and elemental image using high refresh rate panel. Using 120 Hz panel, the multi-view images are displayed at the multi-view phase during 60 Hz and in the integral imaging phase, the 3D object is reconstructed by the elemental image.

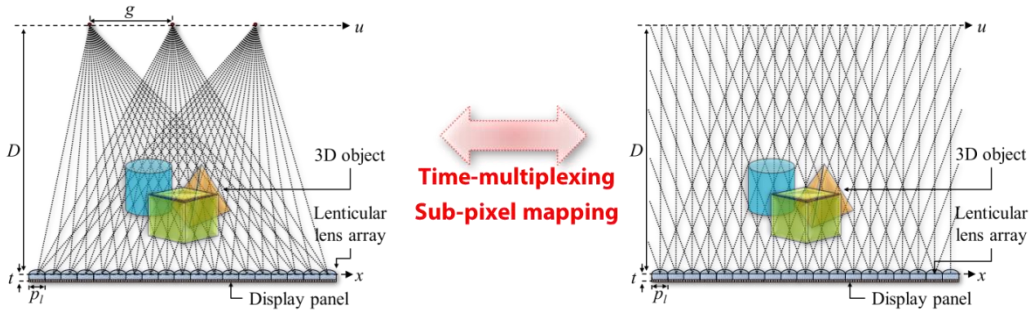

Figure 3.25 Time-multiplexing of multi-view display and integral imaging

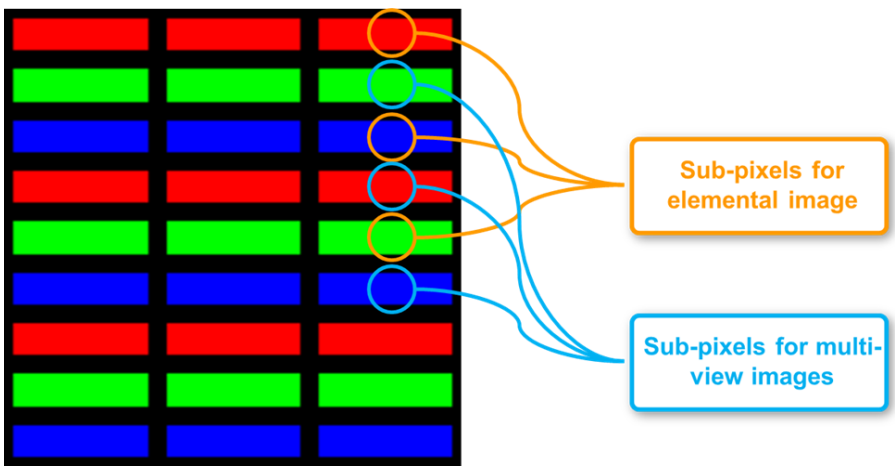

Figure 3.26 Sub-pixel multiplexing method for convergence of multi-view display and integral imaging

The other multiplexing method is interweaving of multi-view image and elemental image with vertical alignment of display panel. The proposed method uses vertical alignment to reduce the moire pattern with the use of lenticular lens array. In the case of time-multiplexing technique, the proposed method uses 120 Hz panel and time-multiplexing of elemental image and multi-view images with two phases. However, 120 Hz panel has limited specification with lenticular lens array. As a countermeasure, the proposed method uses sub-pixel mapping method as shown in Figure 3.26. In the odd lines of sub-pixels express the elemental image and the even lines of sub-pixels show the multi-view images. In spite of the decrease in vertical resolution of 3D object, the quality of 3D object is increased with fusion of multi-view display and integral imaging.

To show the difference between the multi-view and integral imaging in ray space

and the analysis of the quality improvement of the proposed method, I perform the ray space analysis based on the light field [85]. As shown in Figure 3.27(a), multi-view gives the consistent sampling points in s' direction in the case of two-plane parameterization. However, the integral imaging gives inconsistent sampling point in s' direction, which means the multi-view display gives the spatially uniform sampling points. On the other hand, in the case of plane and direction parameterization, multi-view display gives inconsistent sampling points and integral imaging gives consistent sampling points in s direction, and the integral imaging uses the uniform sampling with angular direction as shown in Figure 3.27(b).

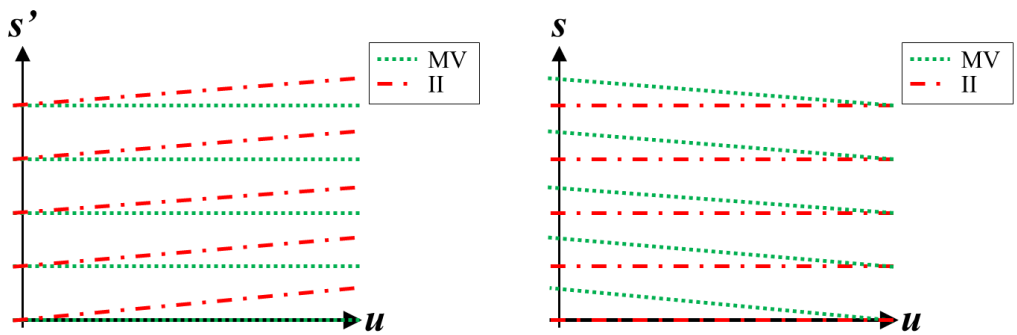

(a) (b)

Figure 3.27 Light field distributions of multi-view display and integral imaging in different parameterizations: (a) two-plane parameterization and (b) plane and direction parameterization

For improvement of the 3D quality of two different autostereoscopic display, I adopt time-multiplexing technique and analyze the 3D quality using the ray sampling quality function of previous research [85]. When Δ is the sampling pitch and (x_i, u_i) is set of all sampling points, the quality function of ray sampling is defined as

$$Q(u,s') = 1 - \frac{2\min_{i \in U}\left(\left\|(u,s') - (u_i', s_i')\right\|\right)}{\Delta}. \tag{3.12}$$

Figure 3.28 shows the difference among the multi-view display, integral imaging, and the proposed method with sampling pattern at the viewpoint and out of viewpoint. As

shown in Figure 3.28(a), the sampling pattern in spatial distribution of multi-view, green line, is uniform and that of integral imaging, red line, is angulary uniform. The quality of 3D object in multi-view display is higher than integral imaging case when the observer is located at the viewpoints as shown in Figure 3.28(b). However, the quality of integral imaging is higher than multi-view case when the observer sees the 3D object at the out of viewpoint as shown in Figure 3.28(c). The proposed method is the average of two methods, and the quality of 3D is increased at the whole viewpoints.

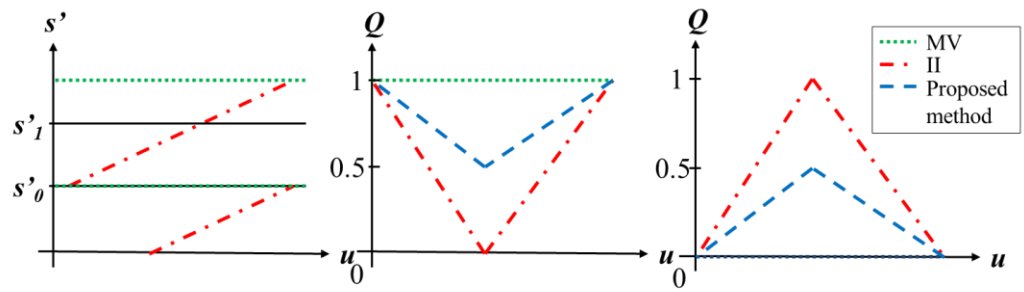

(a) (b) (c)

Figure 3.28 Quality graph at different observer positions: (a) light field distribution of multi-view display and integral imaging in two-plane parameterization, (b) quality graph at viewpoints and (b) out of viewpoint of multi-view display

3.3.3 **Experimental result**

To verify the feasibility of the proposed method, I perform the experiments as shown in Figure 3.29. For the time-multiplexing of multi-view display and integral imaging, I use the 120 Hz panel of Samsung 22-inch monitor 2233RZ model with 1680 by 1050 resolution. The lenticular lens has 2.54 mm pitch and 3.8 mm focal length, and the display panel has 0.282 mm pixel pitch and 120 Hz refresh rate to display multi-view display and integral imaging phase during 1/60 s in each mode. In the case of sub-pixel mapping, WXQUXGA 22-inch high resolution display panel with 3840 by 2400 resolution and 25 LPI lenticular lens with 3.8 mm focal length are used for sub-pixel multiplexing method. The specification of experimental setups is shown in Table 3.2.

Table 3.2 Specification of experimental setups

Setup	Specification	Characteristic
Display panel Samsung 2233rz	Resolution	1680 by 1050
	Size	22 inch
	Pixel pitch	0.285 mm
	Refresh rate	120Hz
Display panel IBM T221	Resolution	3840 by 2400
	Size	22 inch
	Pixel pitch	0.1245 mm
Lenticular Lens (10 LPI)	Size	275 by 300 mm
	Lens pitch	2.54 mm
	Focal length	3.8 mm
Lenticular Lens (25 LPI)	Size	275 by 522 mm
	Lens pitch	1.016 mm
	Focal length	3.8 mm
3D image	Number of views	9
	Viewing distance	878.99 mm
3D object	Depth of letter ‘3’	100 mm
	Depth of letter ‘D’	50 mm

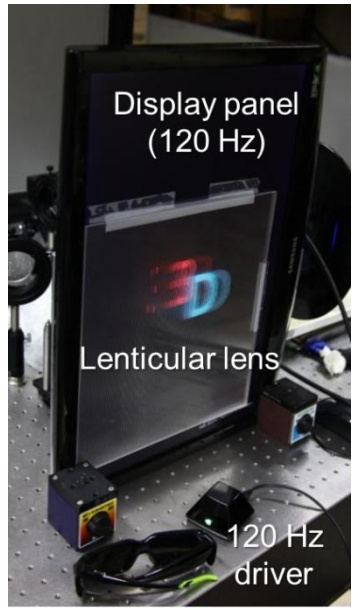

Figure 3.29 Experimental setup

For the multi-view display phase, the proposed method has 3.839 mm gap, 27.34 mm interval of viewpoints and 9.1-view from the mismatch of lens and pixel pitch. The integral imaging phase shares the specifications of optical devices with the multi-view display. From Eq. (3.11), the gap is calculated as 3.839 mm, which is approximately similar to the focal length of lens. Therefore, the integral imaging phase can be assumed to the focal mode. As shown in Figure 3.29, the display panel is rotated to the vertical direction to prevent the moire pattern. The 3D objects for the experiments are generated by the ray tracing method. The letters '3' and 'D' at the different depth plane 100 mm and 50 mm in front of display panel are used for experiment.

Figure 3.30 shows the experimental result of the proposed system in each mode. The proposed method displays the multi-view display and integral imaging phase with time-multiplexing technique. Upper line shows the result of multi-view phase, and second line shows the result of integral imaging, and the last line is the proposed method. Each mode shows the perspectives of reconstructed 3D object with different observer position.

As shown in Figure 3.30, the result of multi-view display shows the quality degradation when the observer position is out of viewpoint in multi-view display. In multi-view display phase, the quality of reconstructed 3D object is better than that in the

integral imaging phase. However, some broken image and omitted image are displayed out of viewpoints as shown in Figure 3.30. On the other hand, the integral imaging phase provides more stable 3D image with different viewpoints and the results show the uniform 3D quality. In the case of proposed method, the reconstructed 3D object is averaged with multi-view display case and integral imaging case. The proposed method display the result of time-multiplexing of multi-view display phase and integral imaging phase. The reconstructed 3D objects in the proposed method have clearer and more stable image quality without omission and crack as shown in Figure 3.30.

To perform the experiment with sub-pixel multiplexing case, the high density WXQUXGA resolution panel with 25 LPI lenticular lens in vertical alignment is used. The 3D objects are 3 letters S, N and U at the 100 mm 60 mm and 30 mm in front of display panel, respectively. Figure 3.31 shows the experimental result in each mode of proposed method. In the case of multi-view display, the discontinuous viewpoint is formed and the ray density is nonuniform. On the other hand, the phase of integral imaging, the 3D object is reconstructed with uniform quality and quasi-continuous viewpoints. To increase the quality of 3D object at out of viewpoints, the proposed method multiplexes the multi-view display and integral imaging using sub-pixel mapping. As shown in Figure 3.31, multi-view display shows ununiform quality of 3D object and the integral imaging shows the uniform quality of 3D images. Therefore, the proposed method shows quality improved results. Although the vertical resolution of 3D object is decreased, no special display panel is needed.

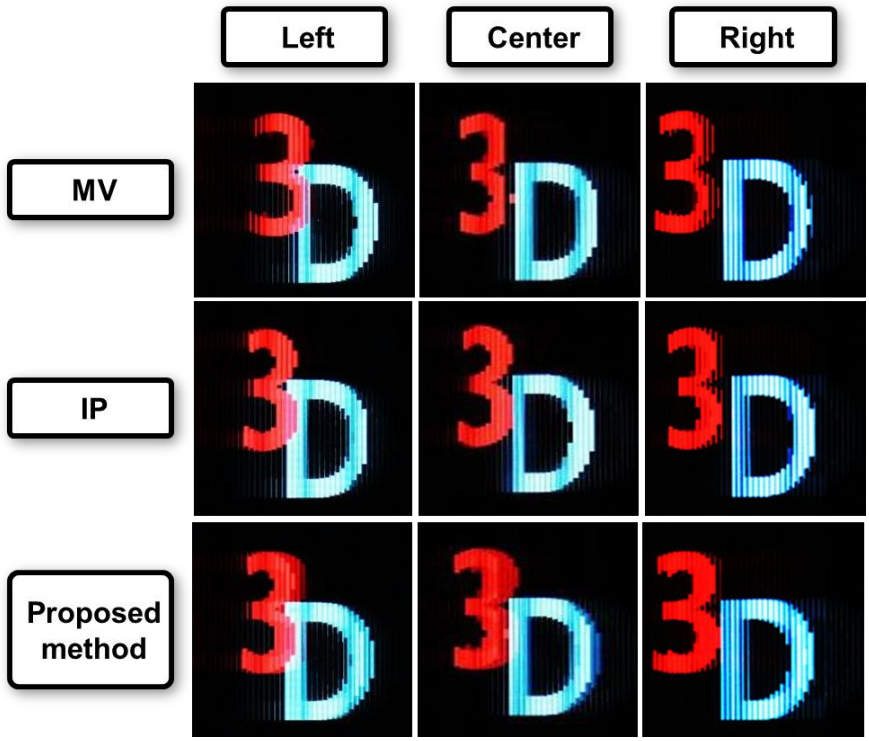

Figure 3.30 Experimental result in proposed method with time-multiplexing method

(a) (b) (c)

Figure 3.31 Experimental result of convergence type of autostereoscopic 3D display using sub-pixel multiplexing: (a) phase of multi-view display, (b) phase of integral imaging and (c) experimental result of proposed method

Chapter 4

Perceived depth resolution and accommodation response of multi-view display and integral imaging

4.1 Effect of fundamental depth resolution and cardboard effect to perceived depth resolution on multi-view display

In three-dimensional television (3D TV) broadcasting, I find the effect of fundamental depth resolution and the cardboard effect to the perceived depth resolution on multi-view display are important. The observer distance and the specification of multi-view display quantize the expressible depth range, which affect the perception of depth resolution of the observer. In addition, the multi-view 3D TV needs the view synthesis process using depth image-based rendering which induces the cardboard effect from the relation among the stereo pickup, the multi-view synthesis and the multi-view display. In this study, I analyze the fundamental depth resolution and the cardboard effect from the synthesis process in the multi-view 3D TV broadcasting. After the analysis, the numerical comparison and subjective tests with 20 participants are performed to find the effect of fundamental depth resolution and the cardboard effect to the perceived depth resolution.

4.1.1 **Introduction**

In recent years, 3D TV broadcasting environment has been constructed with the development of 3D display and digital broadcasting technology by many research groups, broadcasters and equipment manufacturers [8–12]. The system architecture of recently commercialized 3D TV broadcasting is composed of capturing the stereo images of 3D object or the single image with the depth map, transmitting the 3D contents with compression algorithm and displaying them in the commercialized 3D TV set [9–12].

Although the stereoscopic technique based 3D TV broadcasting is central to the mainstream technology, the autostereoscopic multi-view display will be developed as the next-generation 3D TV for overcoming the limitation of the number of views and the use of glasses [13–17]. For the compatibility between stereoscopic and multi-view 3D TV broadcasting, the contents format for multi-view display has to keep the stereo images and the additional depth map information. In multi-view 3D TV broadcasting, the view synthesis process is needed to generate the multi-view images from the stereo images and the depth map information. In the synthesizing process, the accuracy and quality of synthesized view image depend on the synthesizing algorithm and the depth resolution of depth map [18–22]. However, the depth map with high depth resolution needs the wide bandwidth in the transmission process, which leads to the high costs of all broadcasting systems.

The commercialized multi-view display for 3D TV broadcasting is mostly the slanted lenticular display technology, which has the limitation of expressible depth resolution fundamentally [85, 88]. Therefore, the transmitted depth resolution of 3D TV will be limited by the fundamental depth resolution of slanted lenticular system. Even if the depth resolution of depth map in the transmitted contents format is higher than the fundamental depth resolution of the multi-view system, the information will be wasted and inexpressible.

In addition, the depth perception of human visual system (HVS) is decreased by the distance from observer to 3D object. The observer distance of the slanted lenticular multi-view display and the perceived depth resolution are both fixed, which affects to the depth resolution of 3D contents format. Additionally, the cardboard effect is one of the key factors to decrease the perceived depth resolution in the multi-view display [89–91].

From the fundamental depth resolution of multi-view display and the depth perception of HVS, I can assume the saturated value in perceived depth resolution exists in the multi-view 3D broadcasting. This research finds and analyzes the threshold of perceived depth resolution based on the technical factors from the specification of multi-view display and broadcasting process. The evaluation of saturation value of depth resolution in the perceived depth resolution will provide the guideline for the manufacturer of the multi-view display and the 3D TV broadcasting systems.

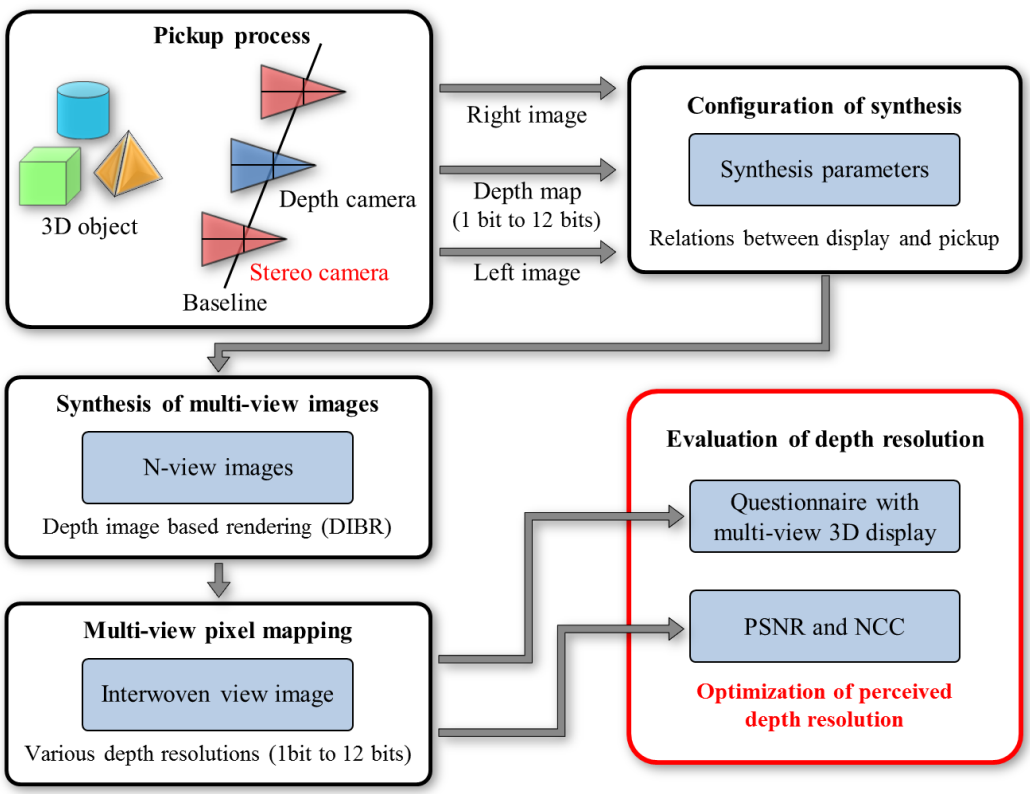

Figure 4.1 Evaluation process of perceived depth resolution in multi-view display

Figure 4.1 shows the detailed process for the evaluation of perceived depth resolution. First, I capture the stereo images and the depth map of 3D object with the variation of depth resolution from 1 bit to 12 bits. The 3D object and the stereo pickup specification are founded by the computational pickup scheme using OpenGL to easily change the parameters of pickup and depth information. To reduce the cardboard effect, I analyze the relation of parameters between the pickup and the synthesis. After capturing,

the multi-view images are synthesized from the stereo images and the depth map with varying the depth resolution using depth image based rendering (DIBR) [18–22]. With varying the depth resolution, the synthesized multi-view images are compared with the ground truth view image in the peak signal-to-noise ratio (PSNR) and the normalized cross-correlation (NCC) to find the threshold of depth resolution numerically. In the interweaving process, the synthesized multi-view images with the different depth resolutions are mapped to the interwoven image for displaying the multi-view images on the slanted lenticular display [14]. The subjective test is performed with the reconstructed 3D images using the 9-view slanted lenticular display. The experimental results are presented and analyzed in this study.

4.1.2 Fundamental depth resolution from specification of slanted lenticular display

In HVS, the observer perceives the depth resolution sensitively nearby the reconstructed 3D object. The sensitivity of perception is inversely proportional to the distance from observer to 3D display. Therefore, the observer distance is the most important specification in the evaluation process. To evaluate the perceived depth resolution in HVS, the optimized observer distance has to be decided by the multi-view display parameters. This study analyzes the perceived depth resolution with the fixation of observer distance from the multi-view display specification.

In these days, most of commercialized multi-view display systems adopt the slanted lenticular display which is proposed by Philips Research Laboratories in 1997 [13–17]. According to them, the number of views per the slanted lens in the horizontal direction X_h and the vertical direction X_v in N-view display using slanted lenticular lens array are given as

$$X_h = \frac{N}{X_v} = \frac{tp_l}{fp_{sp}\cos\alpha}, \tag{4.1}$$

where p_l is the lens pitch, f the focal length, p_{sp} the sub-pixel pitch, α the slant angle, and t the gap between lens and display panel. As shown in Figure 4.2, the effective pixel pitch p_{eff} in the slanted lenticular display is the same as the half of sub-pixel pitch p_{sp}. The

observer distance from lens array D is determined from the relation between the interpupillary distance d_e and the magnified pixel pitch of display. The number of views per the interpupillary distance k is determined to the integer values for showing the stereoscopic images at the whole multi-view positions. Therefore, the distance between each viewpoint g is defined as d_e/k.

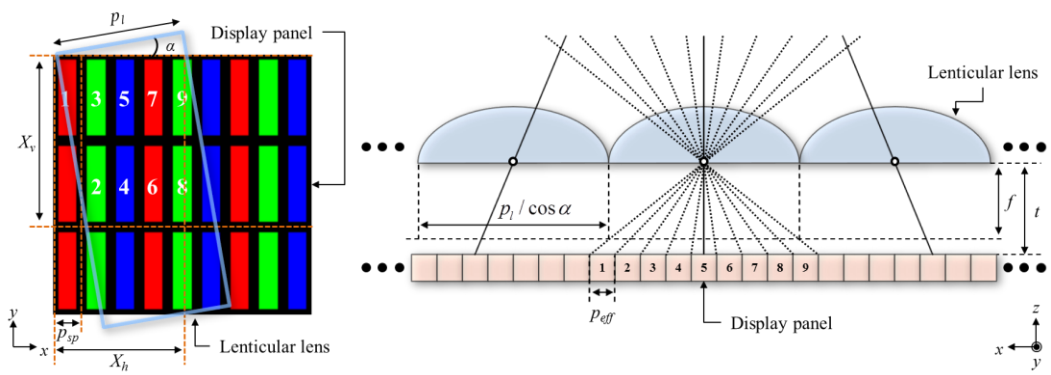

(a) (b)

Figure 4.2 Multi-view 3D display based on slanted lenticular lens: parameters of slanted lenticular system (a) in front view and (b) in upper view

The observer distance is derived from the ratio of g and p_{eff}, which also follows the ratio of slanted lens pitch and width of the N-view area pixels as shown in Eq. (4.2).

$$D = \frac{td_e}{kp_{eff}} = \frac{tp_l}{Np_{eff}\cos\alpha - p_l}. \tag{4.2}$$

From Eqs. (4.1) and (4.2), the lens pitch p_l is determined by the relation between interpupillary distance d_e and effective pixel pitch p_{eff} as follows:

$$p_l = \frac{Np_{eff}d_e\cos\alpha}{kp_{eff} + d_e}, \tag{4.3}$$

$$t = \frac{Nfp_{eff}\cos\alpha}{p_l}. \tag{4.4}$$

Equation (4.4) determines the gap between display panel and lenticular lens t from Eqs.

(4.2) and (4.3). The observer distance D is determined from Eq. (4.2) with the calculated p_l and t from Eqs. (4.3) and (4.4). To evaluate the perceived depth resolution, the observer position is fixed at the observer distance from Eqs. (4.2) – (4.4).

From the specification of multi-view display, the expressible depth planes and range are limited between the near depth plane D_N and the far depth plane D_F [17]. In the general case of stereoscopic display or multi-view display, the feasible range of disparity is limited from 1% to 5% of the width of display resolution, which is more decreased and limited than D_N and D_F by the crosstalk because of the color dispersion, the lens distortion and the misalignment [13–17].

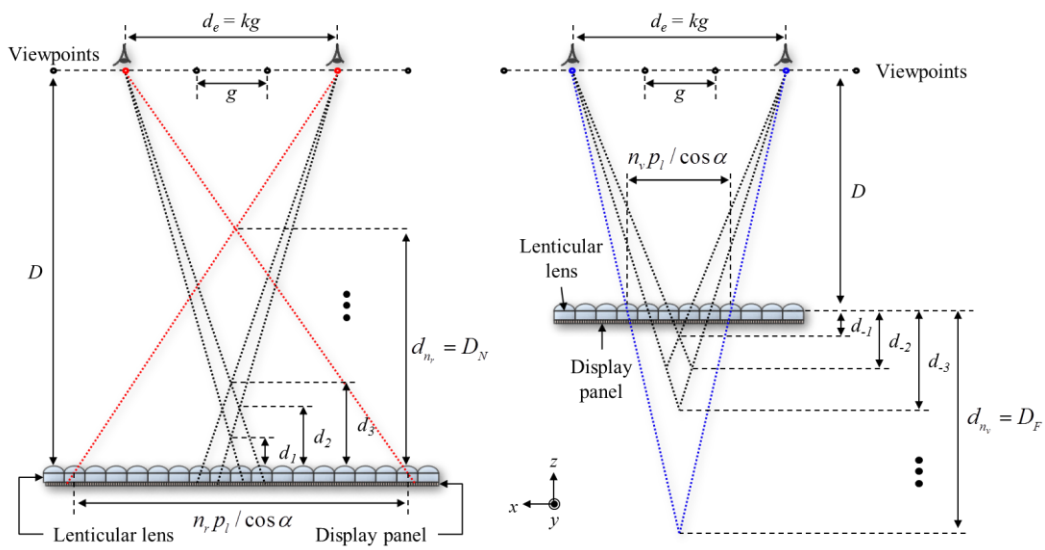

(a) (b)

Figure 4.3 Expressible depth planes in (a) real and (b) virtual mode of multi-view display (k = 3)

The principle of multi-view display for representing 3D object is the same as the method of stereoscopic display in the fixed viewpoint, even though the number of viewpoints is N. The expressible depth planes are quantized with the finite lens disparity as shown in Figure 4.3. Equation (4.5) shows the depth plane determined by the n-th lens disparity d_n.

$$d_n = \frac{np_l D}{kg\cos\alpha + np_l}. \tag{4.5}$$

As shown in Figure 4.3(a), the cross point of two different rays from left and right lenses is located in front of the display panel when the 3D object is reconstructed in the real mode. The lens disparity n is the positive integer value in the real mode and the nearest depth plane D_N is formed from the maximum lens disparity in the real mode n_r. Furthermore, the 3D object in the virtual mode is reconstructed at the rear of display panel with the lens disparity of the negative integer value as shown in Figure 4.3(b). The smallest lens disparity n_v forms the farthest depth plane D_F and the interval of depth planes in the virtual mode is larger than the real mode. The maximum lens disparity n_r and the minimum lens disparity n_v are derived as follows:

$$n_r = \frac{D_N kg\cos\alpha}{(D - D_N)p_l}, \quad n_v = \frac{D_F kg\cos\alpha}{(D - D_F)p_l}. \tag{4.6}$$

From the multi-view display specification, the expressible depth level of display, which is the same as the fundamental depth resolution n_d, is determined by the difference of maximum lens disparity and minimum lens disparity as follows:

$$n_d = n_r - n_v = \frac{kg\cos\alpha}{p_l}\left(\frac{D_N}{D - D_N} - \frac{D_F}{D - D_F}\right). \tag{4.7}$$

If the capturing and transmitting processes provide the depth map with lower depth resolution than the expressible depth level of display, the multi-view display represents the 3D object with quantization and cracking in the depth direction. On the other hand, the depth resolution of reconstructed 3D object is limited by the expressible depth resolution of display even though the depth resolution of depth map is higher than the expressible depth level. However, the assumption of depth resolution limitation is considered except the characteristics of perception in HVS.

4.1.3 View synthesis parameters from specification of stereo pickup and multi-view display

In the multi-view 3D broadcasting, the relation among the stereo pickup specifications,

the multi-view synthesis parameters and the display specification affect the perception of depth resolution of reconstructed 3D object. The 3D display has not only the planar resolution, but also the resolution of depth direction to display the 3D volume object. However, the observer perceives the depth resolution of reconstructed 3D object differently because of the various cues and effects in HVS. One of the depth perception effects in HVS is the cardboard effect [89–91].

The cardboard effect refers to a phenomenon where the 3D objects represented at different depth planes appear as flat layers to observers. If the spatial thicknesses of represented 3D object and acquired 3D object are different, the reconstructed 3D object is perceived to the observer as the planar images with the cardboard effect. To analyze the occurrence condition of cardboard effect, the specification of stereo pickup and the relation between multi-view synthesis and display are shown as Figure 4.4. In the multi-view 3DTV broadcasting, the first step is capturing the stereo images and the depth information using shift sensor configuration as shown in Figure 4.4(a). As shown in Figure 4.2, the principal point of lenticular lens is shifted from the view images at the observer distance D because N-pixel behind one lenticular lens is larger than lens pitch p_l. Therefore, the configuration of shift sensor model uses the same principle as the multi-view display, and the plane of convergence is established by a small shift h of the sensor targets as shown in Figure 4.4(a) [12, 18]. For generating depth map, the near depth plane D_{NS} and far depth plane D_{FS} of 3D objects are set around the convergence distance D_S.

After acquiring the stereo images and depth map, N-view images are synthesized by the recapturing of the reconstructed 3D object in virtual space using DIBR as shown in Figure 4.4(b). The coordinate of stereo pickup is scaled with the magnification factor r which is defined as D/D_S. In the DIBR process, N virtual cameras capture the reconstructed 3D object which is reconstructed from the depth map and the stereo images, considering the specification of multi-view display [18–22]. The distance from reconstructed 3D object to multi-view cameras is equal to the observer distance D. The multi-view cameras from C_1 to C_N and the scaled stereo camera C_L' and C_R' are located at the same baseline and aligned in the scaled interaxial distance of stereo camera rg_s.

In this situation, the interaxial distance of multi-view cameras g_c is set with consideration of the specification of multi-view display. Although the convergence

distance of multi-view cameras is the same as the observer distance D, the near and far depth planes of display D_N and D_F are different from the near and far depth planes of reconstructed 3D object rD_{NS} and rD_{FS}. If rD_{NS} and rD_{FS} are smaller than D_F and D_N, the multi-view display can show the 3D object in the expressible depth range without flipping and cracking. Therefore, g_c is determined to be the same as g, and the observer can watch the 3D object without the cardboard effect.

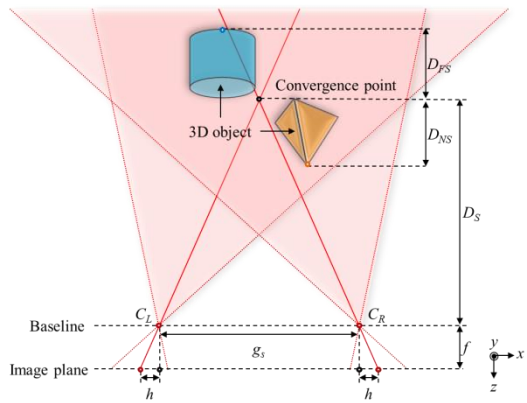

(a)

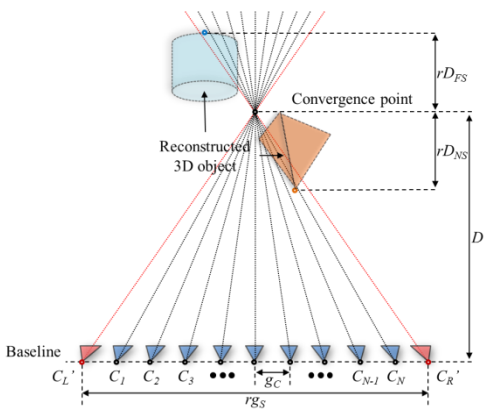

(b)

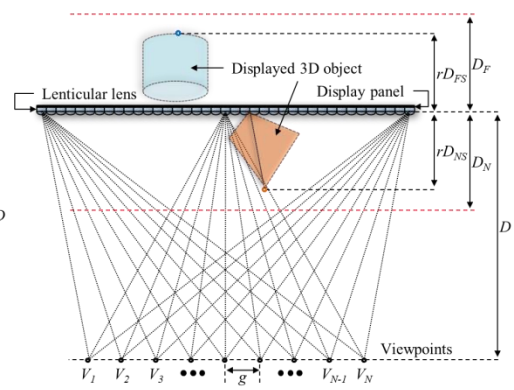

(c)

Figure 4.4 Parameters of stereo to multi-view camera configuration and display: (a) stereo pickup, (b) multi-view pickup, and (c) multi-view display

On the other hand, the multi-view display cannot express the exact 3D object when the depth range of reconstructed 3D object in virtual space exceeds the expressible depth

range. To prevent the excess of expressible depth range in the multi-view display, the spatial thickness of reconstructed 3D object has to be magnified with the adjustment of interaxial distance of multi-view camera g_c. The interaxial distance g_c with consideration of the depth range in multi-view display is derived as shown in Eq. (4.8), where the rD_{NS} and rD_{FS} are larger than D_N and D_F.

$$g_c = \begin{cases} \dfrac{gD_N}{D-D_N} \cdot \dfrac{D-rD_{NS}}{rD_{NS}}, & D_{NS} \geq -D_{FS} \\ \dfrac{gD_F}{D-D_F} \cdot \dfrac{D-rD_{FS}}{rD_{FS}}, & D_{NS} < -D_{FS}. \end{cases} \tag{4.8}$$

From the relation between the parameters of multi-view synthesis and display, the ratio of spatial thickness between pickup and display configuration E_c is determined as follows:

$$E_c = \frac{D}{g} \cdot \frac{g_c}{D_c}. \tag{4.9}$$

In previous researches, the cardboard effect is vanished when the ratio of spatial thickness E_c is kept as 1 [89–91]. In addition to the ratio of spatial thickness, the light source of 3D object and background affect the cardboard effect. The use of the flat light source instead of the point light source and the case of 3D image without background can reduce the cardboard effect. For reducing the cardboard effect in pickup and synthesizing process, the ratio of observer distance to viewpoint distance in the display and the ratio of convergence distance and camera interval in the synthesis process have to be kept by the synthesis parameters.

However, the depth camera acquires the depth information between D_{NS} and D_{FS} regardless of the expressible depth range of multi-view display from D_N to D_F because the specifications of each multi-view display are different in the multi-view 3D broadcasting. Therefore, the parameters of synthesis are defined by the specification of multi-view display, and occurring of the cardboard effect is an inevitable phenomenon in the multi-view 3D broadcasting. From the result of cardboard effect in the display, I can assume the perceived depth resolution is decreased and the saturation of perceived depth resolution exists in the multi-view 3D broadcasting.

4.1.4 Stereo pickup and multi-view synthesis of 3D object with varying depth resolution

In the previous section, I discussed the fundamental depth resolution and the synthesis parameters with considering the cardboard effect, which are the factors to affect the perceived depth resolution. With consideration of the fundamental depth resolution and the cardboard effect, I perform the evaluation process of the perceived depth resolution as shown in Figure 4.1. To evaluate the saturation bits of perceived depth resolution, I first acquire the stereo images and the depth information of 3D object with varying the depth resolution from 1 bit to 12 bits. The pickup process uses the computational pickup framework using OpenGL to secure the ground truth of depth map and change the depth map resolution easily.

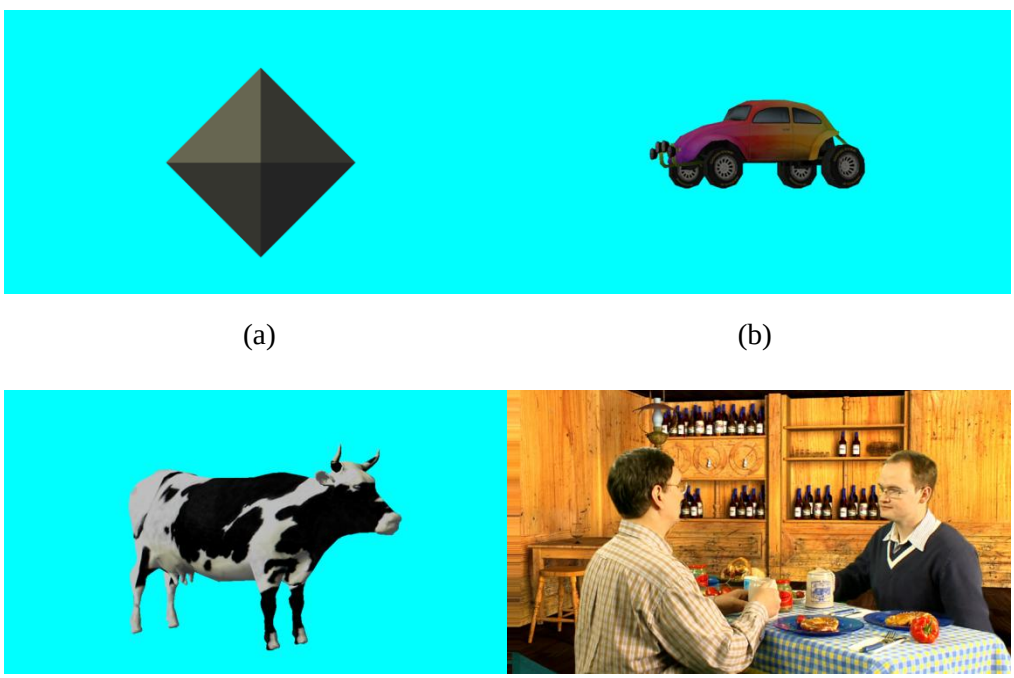

(a) (b)

(c) (d)

Figure 4.5 Contents for evaluation process of perceived depth resolution: (a) pyramid, (b) car, (c) cow, and (d) beergarden

To reduce the cardboard effect, I use the flat light source and the 3D object without background. The evaluation process is applied to the 3 kinds of computer graphic (CG)

contents and the contents of actual beergarden objects which are captured by the 3D4YOU consortium [92] as shown in Figure 4.5. The beergarden content involves the additional cues such as occlusions, perspective and shades in the background of objects. In the case of real 3D contents, the background condition, lighting condition and spatial distortion are inevitable condition in acquiring process. Therefore, I perform the evaluation process with CG contents and beergarden content to compare the condition of cardboard effect. In consideration of the recent broadcasting environment, the resolution of stereo image is set to the full HD resolution (1920 by 1080).

Before the acquiring stereo images and depth map, I set the position of 3D object from the convergence distance D_S differently for three modes such as the real, the virtual and the real-and-virtual mode. I use the three modes of contents in the evaluation process so as to find the effect of the distance from 3D object to observer because the observer distance of multi-view display is fixed. In the real mode, the whole volume of 3D object is located in front of the convergence point, and the 3D object in the virtual mode is located at the behind of convergence point. In the real-and-virtual mode, the center position of 3D object is the same as D_S to generate both the real and the virtual 3D images.

In this study, I assume the expressible depth range of multi-view display is set to ±150 mm and the observer distance is 1175 mm in front of the display panel. Table 4.1 shows the specification of stereo pickup and the positions of 3D object in the different modes. In CG contents, the pickup parameters D_S and g_s are set to the same as D and Ng of multi-view display to avoid the cardboard effect. On the other hand, the beergarden content which has 1897 mm D_{NS} and -1897 mm D_{FS} is captured without considering the expressible depth range of multi-view display. To generate the three modes of beergarden content, I adjust the convergence point of the beergarden content with different g_s. From the setting of near depth plane D_{NS} and far depth plane D_{FS}, the depth map is acquired with varying the depth resolution from 1 bit to 12 bits as shown in Figure 4.6. In the CG contents, the depth map can be acquired with varying the depth resolution. However, the depth resolution of beergarden is fixed to 8 bits. To generate the depth map of beergarden content with 1 bit to 13 bits depth resolutions, the depth information of beergarden contents is converted from intensity of 8 bit gray level values to real distance [18]. After the conversion, the depth information is quantized with nonlinear quantization equation

as follows:

$$I = \left(2^k - 1\right)\left[\frac{D_{NS}\left(D_{FS} - D\right)}{D\left(D_{FS} - D_{NS}\right)}\right], \tag{4.10}$$

where I specifies the respective intensity of k bits depth map. Each depth map with different depth resolution is generated by the different quantization levels with bicubic interpolation method.

Table 4.1 Stereo pickup specification of contents for evaluation of perceived depth resolution

Mode	Position of object (mm)		D_S (mm)		g_s (mm)	
	CG	Beergarden	CG	Beergarden	CG	Beergarden
Real	0 ~ 150	0 ~ 3794	1175	4742	325	318
Virtual	-150 ~ 0	-3794 ~ 0	1175	948	325	63
Real & virtual	-150 ~ 150	-1897 ~ 1897	1175	2845	325	191

After the pickup process, the synthesis parameters for multi-view image are determined by the pickup and the multi-view display specifications. The view images are synthesized by DIBR. The DIBR methods are researched and proposed by the many groups in computer vision and image processing field [18–22]. For the reasonable evaluation of the perceived depth resolution, I try to reduce the influence of DIBR process, therefore the view synthesis reference software (VSRS) of MPEG is used as the reference method [22].

In the CG contents, the synthesis parameters are set to the same as parameters of the multi-view display because D_{NS} and D_{FS} are equal to D_F and D_N. However, the depth range of beergarden content exceeds to the expressible depth range of the multi-view display of experimental setup. Therefore, the cardboard effect occurs and the spatial thickness is reduced as shown in Table 4.2.

(a) (b)

(c) (d)

Figure 4.6 Acquired depth maps of 4 contents with varying depth resolution from 1 bit to 12 bits: (a) pyramid, (b) car, (c) cow, and (d) beergarden

Table 4.2 Multi-view pickup specification of beergarden contents

Mode	R	E_c	g_c (mm)
Real	0.2478	0.0366	1.2
Virtual	1.2392	0.1415	4.60
Real & virtual	0.4131	0.0731	2.4

The synthesized N-view images with different depth resolutions and modes are interwoven to each interwoven images for the multi-view display. Therefore, the interwoven images with different depth resolutions are displayed to the evaluation of perceived depth resolution with the subjective test.

4.1.5 Numerical comparison of synthesized view images in PSNR and NCC with varying depth resolution

Before the subjective test, the numerical comparison of synthesized view image is performed by PSNR and NCC. The ground truth image of pickup process with CG in 5th view image position is captured by the CG pickup framework, which is set to the reference image of PSNR and NCC calculation. I calculate the PSNR and NCC value between the synthesized 5th view image with varying depth resolutions and ground truth image in different modes as shown in Figure 4.7.

As shown in Figure 4.7, PSNR and NCC values with higher depth resolution are higher than lower depth resolution case although some fluctuations of PSNR and NCC values occur from the hole-filling of DIBR process. The PSNR and NCC values have the saturation of depth resolution between 5 bits and 7 bits in the CG contents. In the beergarden content, the depth information is captured by the time-of-flight camera with 8 bits depth resolution, and the maximum depth resolution of content is increased to 13 bits by image processing technique. Nevertheless, the PSNR and NCC values are saturated around 5 to 7 bits as shown in Figure 4.7(d). Therefore, the numerical comparison shows the existence of saturation of depth resolution in the synthesis process, and the saturation values are 7 bits or under. From the numerical comparison, the depth resolution in the synthesis process can be reduced to the saturated depth resolution which is less than 8 bits in the conventional system.

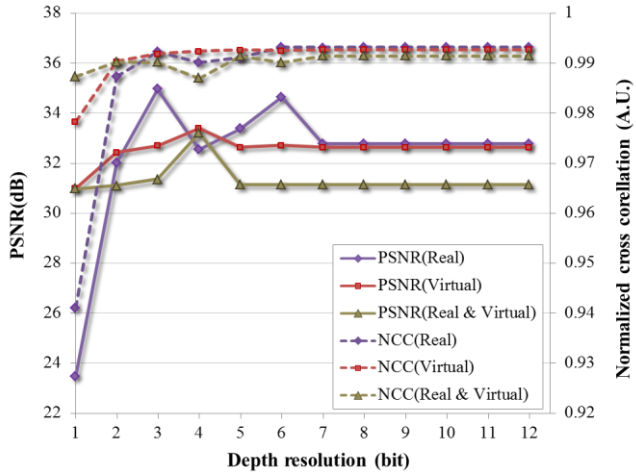
PSNR(dB)
Normalized cross corellation (A.U.)
Depth resolution (bit)
PSNR(Real)
PSNR(Virtual)
PSNR(Real & Virtual)
NCC(Real)
NCC(Virtual)
NCC(Real & Virtual)

(a)

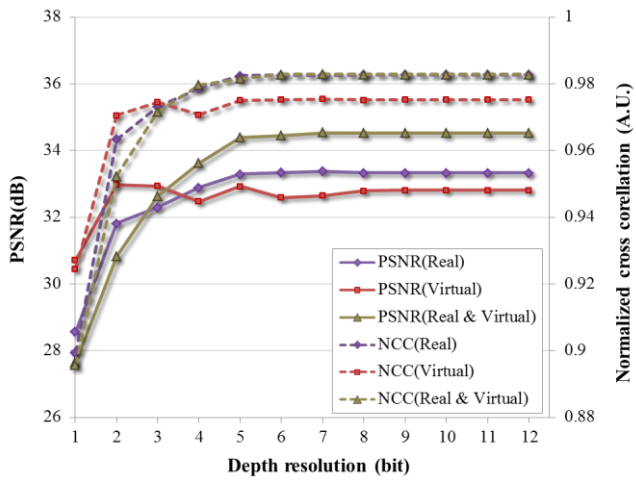
PSNR(dB)
Normalized cross corellation (A.U.)
Depth resolution (bit)
PSNR(Real)
PSNR(Virtual)
PSNR(Real & Virtual)
NCC(Real)
NCC(Virtual)
NCC(Real & Virtual)

(b)

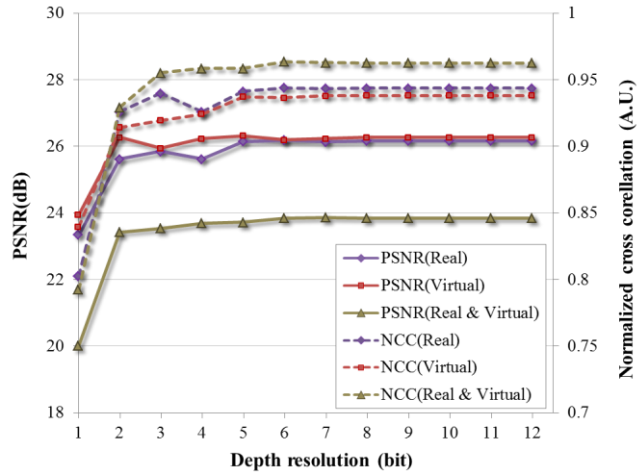

(c)

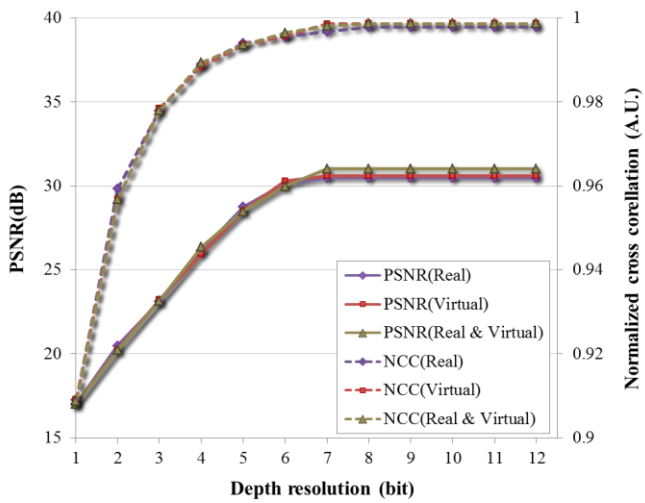

(d)

Figure 4.7 Numerical comparison of synthesized view image and ground truth image in PSNR and NCC with varying depth resolution: (a) pyramid, (b) car, (c) cow, (d) beergarden

4.1.6 **Subjective test for limitation of perceived depth resolution in multi-view display**

To find the effect of fundamental depth resolution in multi-view display and the

cardboard effect to limitation of perceived depth resolution, I performed the subjective test with participants using the multi-view display. The process before the subjective test is the same as the evaluation process of the numerical comparison. In subjective test, I show the interwoven image with the different depth resolutions to the observer using the 9-view slanted lenticular monitor. The 9-view slanted lenticular monitor is composed of the display panel with high resolution and the slanted lenticular lens as shown in Table 4.3. The observer distance is determined from the specification of display panel and lens using Eq. (4.2).

Table 4.3 Specification of the experimental setup

Setup	Specification	Characteristic
Display panel	Resolution	3840 by 2400
	Size	22 inch
	Pixel pitch (p_p)	0.1245 mm
Lenticular lens	Lens pitch (p_l)	0.1845 mm
	Focal length (f)	0.75 mm
	Slant angle (α)	9.4623 degree
Multi-view display	Observer distance (D)	1175 mm
	Number of views (N)	9
	Interval of viewpoints (g)	32.5 mm
	The number of views per interpupillary distance (k)	2
	Near depth plane (D_N)	150 mm
	Far depth plane (D_F)	-150 mm
	Resolution of 3D image	1280 by 800

Figure 4.8 shows the experimental setup of subjective test. To evaluate the saturation of perceived depth resolution, I perform the experiments that the observers watch the reconstructed 3D object using the 9-view slanted lenticular display with the 4 different contents with varying the depth resolution from 1 bit to 12 bits which have three modes with different object positions. The expressible depth range of multi-view display panel is from 150 mm to -150 mm and the depth range of content cannot exceed this limitation to

avoid the flipping image. Figure 4.9 shows the perspectives of 4 contents for the evaluation process at different viewpoints.

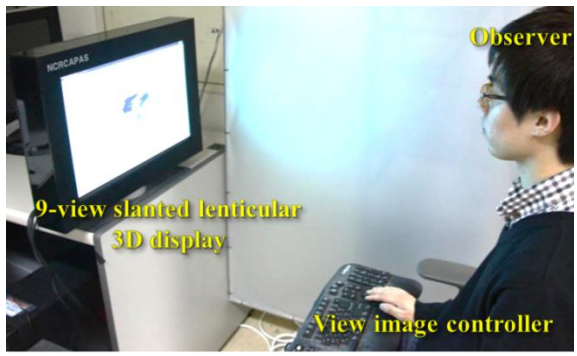

Figure 4.8 Experimental setup of subjective test for perceived depth resolution

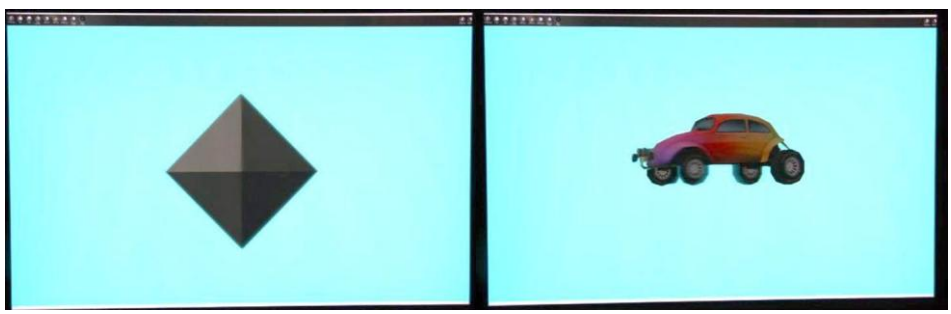

(a) (b)

(c) (d)

Figure 4.9 Represented 3D objects in 4 contents using 9-view slanted lenticular monitor: (a) pyramid, (b) car, (c) cow, and (d) beergarden

Before the evaluation process, the observer should adjust the offset of interwoven

image because the alignment process is affected to the perception of depth in the multi-view display. The observer sits 1.2 m in front of multi-view display and adjusts the offset using the view image controller. The observer finds the acceptable viewpoint of different contents. After the alignment process, the 9-view monitor reconstructs the 3D contents with varying the depth resolution from 1 bit to 12 bits. If the observer can feel a 3D effect and find the difference between 3D images with low depth resolution and high depth resolution, the depth resolution of reconstructed 3D object is increased. After the increment of depth resolution, if the observer cannot find the difference between reconstructed 3D objects from high and low depth resolution, the saturated depth resolution in this situation is determined.

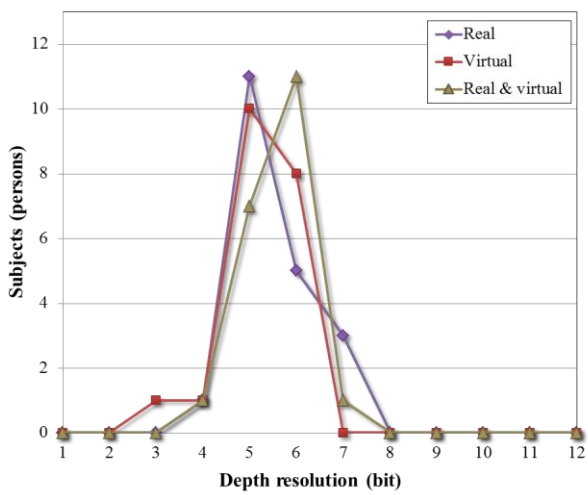

(a)

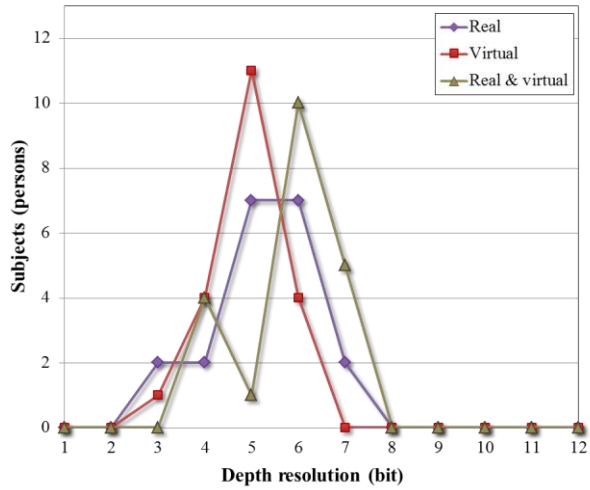
Real
Virtual
Real & virtual
Subjects (persons)
Depth resolution (bit)
0
2
4
6
8
10
12
1
2
3
4
5
6
7
8
9
10
11
12

(b)

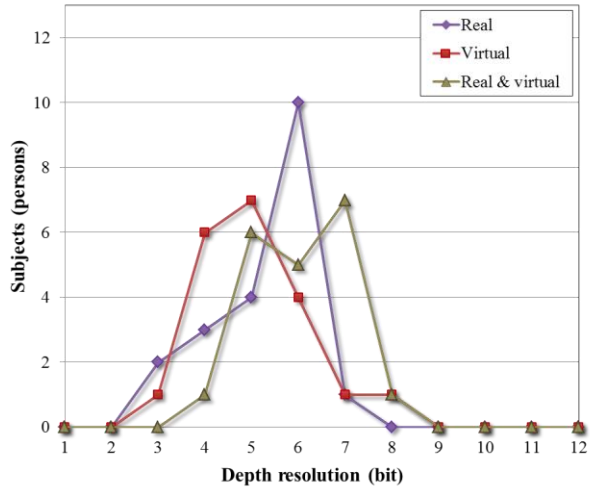
Real
Virtual
Real & virtual
Subjects (persons)
Depth resolution (bit)
0
2
4
6
8
10
12
1
2
3
4
5
6
7
8
9
10
11
12

(c)

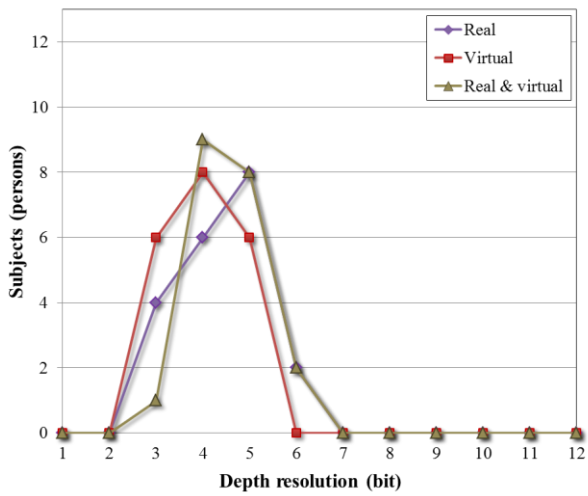

(d)

Figure 4.10 Experimental result of subjective test with varying depth resolution: (a) pyramid, (b) car, (c) cow, and (d) beergarden

Figure 4.10 shows the result of subjective test in the different contents and modes with 20 participants. The participants are staff and students of my research groups (17 men and 3 women) with a mean age of 28.95 years (range from 23 to 37 years). All participants have the experience of the 3D display and do not have strabismus. They can feel the 3D effect from the multi-view display and perceive the reconstructed 3D objects with different depth resolution and modes. As shown in Figure 4.10, the threshold of perceived depth resolution is not increased with the depth resolution of depth maps, which is saturated around 5 to 7 bits in the CG contents. In the case of pyramid content, most of the participants chose the same depth resolution as the threshold of the perceived depth resolution. On the other hand, the experimental result of cow content is a little bit spread out. The reason of different variance of experimental result is the characteristics of contents. The pyramid content has smooth, continuous and simple structure whereas the cow content has many curve and complex structures such as legs and horns. Although the result depends on the characteristic of contents and the result of the case of complex contents is spread out, the threshold of perceived depth resolution in the virtual mode marks the lowest value and the real-and-virtual mode needs the highest depth resolution.

In contrast, the result of beergarden contents marks the lower depth resolution than

the CG cases because of the cardboard effect from the synthesis process. When the cardboard effect occurs, the observer perceives the reconstructed 3D object as the floating planes. Therefore, the observer is insensitive to the increments of depth resolution due to the cardboard effect.

The result of subjective test shows that the threshold of perceived depth resolution exists in the environments of multi-view broadcasting system. I calculate the fundamental depth resolution of multi-view display to compare with the fundamental depth resolution of multi-view display and the subjective test results. The fundamental depth resolutions are 5.6724, 5.2854 and 6.4919 bits in the real, the virtual and the real-and-virtual modes from Eq. (4.7).

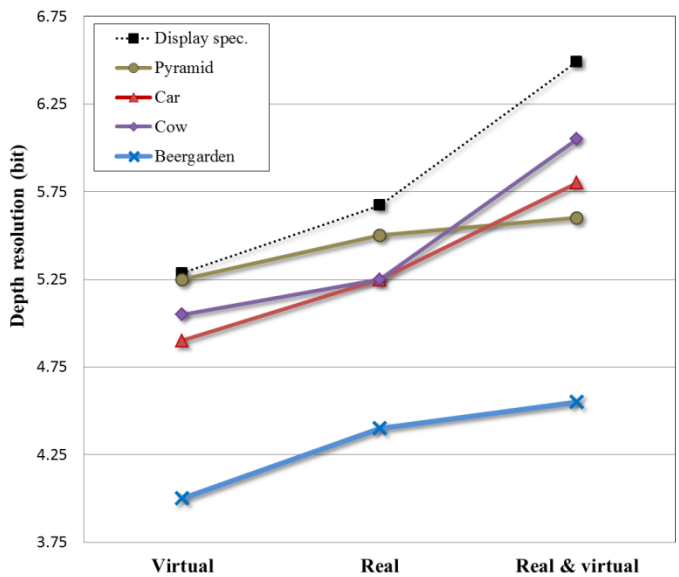

Figure 4.11 Experimental result of subjective test with average values in different modes

To show the tendency of the perceived depth resolution in the multi-view display with the different depth resolution, the result of subjective test in the different modes with average values is represented as shown in Figure 4.11. From the tendency, the distribution of the threshold of perceived depth resolution in each mode is very similar to the fundamental depth resolution of multi-view display. However, all depth resolution values from the subjective tests mark the lower value than the fundamental depth resolution. Especially, the perceived depth resolution of beergarden content marks the lowest value because of the cardboard effect. Therefore, the observer perceives the depth resolution

lower than the fundamental depth resolution of multi-view display and the depth perception in the multi-view display is more insensitive when the cardboard effect appears.

The cognitive factors, the technical factors and the psychological condition affect the perception of depth resolution in multi-view display. I analyze and find the threshold of perceived depth resolution based on the technical factors from the specification of multi-view display and broadcasting process. From the numerical and subjective experimental results, the technical factors to saturate the perceived depth resolution in the multi-view broadcasting are the multi-view synthesis process, the fundamental depth resolution of multi-view display and the cardboard effect.

The first technical factor occurs in the multi-view synthesis process from the stereo images and the depth information using DIBR. From the numerical experiments with PSNR and NCC values, the depth resolution of 3D contents for multi-view display is saturated around 5 to 7 bits, which comes from the DIBR process. Even if the depth resolution of 3D contents is over the saturated depth resolution from the numerical experiments, the DIBR process cannot improve the quality of synthesized view-image. The second technical factor is the fundamental depth resolution of multi-view display which is determined by the principle of multi-view display and the depth quantization problem. Therefore, the perceived depth resolution follows the lowest depth resolution from the first or second factor.

The last factor is the cardboard effect between pickup and display processes. Generally, the depth range of pickup specification exceeds the expressible depth range of multi-view display, which results in the cardboard effect from the difference of the ratio of spatial thickness. Although the depth resolution of 3D contents satisfies the numerical limitation and the fundamental depth resolution of multi-view display, the observer is becoming desensitized to the depth resolution because of the cardboard effect.

4.1.7 **Conclusion**

I find the effect of the fundamental depth resolution of multi-view display and the cardboard effect from the synthesis process to the depth perception on multi-view display. To find the threshold of perceived depth resolution, I analyze the fundamental depth

resolution and the factors for cardboard effect and perform the evaluation process. According to the subjective tests with 20 participants and the numerical comparison with PSNR and NCC, I find the threshold of depth resolution in the view synthesis process and the limitation of perceived depth resolution in multi-view display. The perceived depth resolution is lower than the fundamental depth resolution and shows very similar distribution with the fundamental depth resolution. In addition, the cardboard effect decreases the perceived depth resolution in the multi-view display. The technical factors for the limitation of perceived depth resolution in the multi-view display are analyzed and described.

4.2 Effect of viewing region satisfying super multi-view condition in integral imaging

I analyze viewing region satisfying SMV condition in integral imaging and evaluate the accommodation response when the observer is located inside and outside of the SMV region in integral imaging. To reveal the relation between the SMV condition and accommodation response of integral imaging, I perform the numerical analysis with SMV condition in integral imaging and present the experimental results of accommodation response using autorefractometer.

4.2.1 Introduction

In recent years, three-dimensional (3D) display technologies have been developed and researched by many groups and manufacturers as the next generation display [3]. For perceiving realistic 3D images without nausea and headaches, many research groups measured and analyzed the human factors and the key technical factors of 3D displays. Commercialized stereoscopic type 3D displays give limited depth cues such as binocular disparity and convergence. From the limited depth cues in stereoscopic type 3D display, the observer feels nausea and headaches from the conflict between accommodation and convergence [93–95]. To avoid this conflict, the key issue of next-generation 3D display is the method for leading accommodation response. However, many 3D display technologies have the accommodation-convergence (AC-CV) conflict which causes vertigo, nausea and headaches except holography and volumetric 3D display. In autostereoscopic 3D display technologies, the SMV display and integral imaging are suggested to overcome the AC-CV conflict, and their accommodation responses were evaluated by many research groups [93–95].

The SMV condition is a widespread conviction that leads to accommodation response, and it was also shown in recent researches that integral imaging can give the depth cue of accommodation [93, 96, 97]. Figure 4.12 shows the concept of SMV display. In the extension of the previous researches, I first find viewing region satisfying SMV condition in integral imaging with varying system characteristics. In this study, I analyze the observer position which is satisfied with the SMV condition in integral imaging to

verify the relation between integral imaging and SMV condition. The SMV region in integral imaging following the lens specification and the observer position is analyzed by numerical simulation. In addition, I find the effect of viewing region satisfying SMV condition in integral imaging from the point of view of the accommodation response. I evaluate the accommodation response of the observer inside and outside of SMV region in integral imaging to reveal the relation between accommodation response of integral imaging and SMV condition.

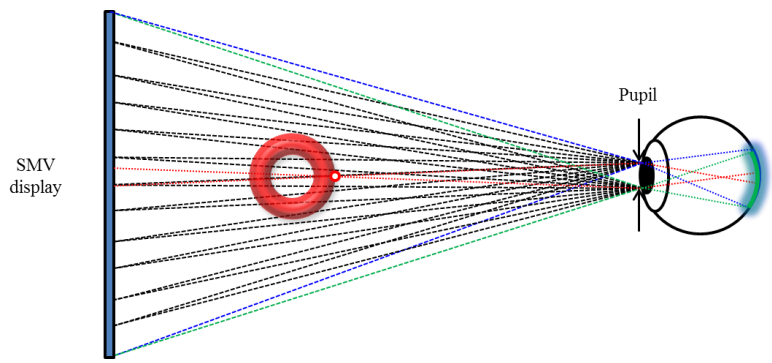

Figure 4.12 Concept of super multi-view display

4.2.2 **Analysis of viewing region satisfying super multi-view condition in integral imaging**

To induce accommodation response in autostereoscopic type 3D display, SMV condition was suggested by Honda and Shimomatsu [93]. In multi-view display, the accommodation response of observer is changed by disparity of two different view images projected on the single retina when each view interval is narrower than eye pupil size. This condition is called SMV condition and its application is SMV display. In the case of multi-view display, the rays from each view image are concentrated at each view point. However, the rays of integral imaging system from elemental images are diverging in the range of viewing angle. Therefore, the SMV condition in integral imaging is different from multi-view based methods and has a relation between the viewing region and accommodation response.

Figure 4.13 shows the principles of integral imaging with focal mode at the observer position (x, y). To analyze the viewing region satisfying SMV condition in integral

imaging, I assume that the right eye of observer is located at (x, y) and 4 different views are reconstructed at (x, y), ($x+d_p$, y), ($x+d_e$, y) and ($x+d_e+d_p$, y) viewpoints where the eye pupil size is d_p and the interpupillary distance is d_e. For satisfying SMV condition in integral imaging, the observer has to be located in the non-flipped image region with satisfying binocular disparity condition and take at least one pixel disparity among view images at (x, y) and ($x+d_p$, y) or ($x+d_e$, y) and ($x+d_e+d_p$, y).

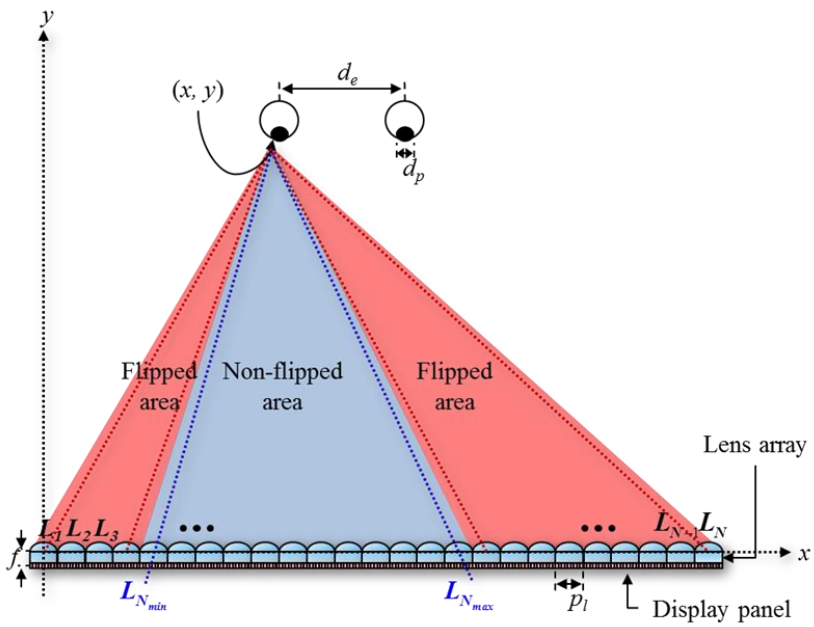

Figure 4.13 Principle of integral imaging at observer position (x, y)

The first constraint to reveal the region satisfying SMV condition in integral imaging is that the observer should be located in non-flipped area in integral imaging as shown in Figure 4.13. Equation (4.11) shows the reconstruction condition without flipping problem in integral imaging, where the lens number is n, pitch of lens is p_l and focal length of lens array is f.

$$-\frac{p_l}{2} \le \frac{f\left[(n-1)\,p_l - x\right]}{y} \le \frac{p_l}{2}. \tag{4.11}$$

As shown in Eq. (4.11), lens number n is limited by the non-flipped area where the observer watches the elemental image region without exceeding boundary. The maximum

lens number N_{max} and minimum lens number N_{min} without flipping problem at the observer position (x, y) are derived as follows:

$$N_{\min}(x,y)=\begin{cases}1 & , \ \dfrac{x}{p_l}-\dfrac{y}{2f}\le 0\\ \left\lceil \dfrac{x}{p_l}-\dfrac{y}{2f}+1\right\rceil & , \ \dfrac{x}{p_l}-\dfrac{y}{2f}>0\end{cases}$$

$$N_{\max}(x,y)=\begin{cases}\left\lfloor \dfrac{x}{p_l}+\dfrac{y}{2f}+1\right\rfloor & , \ \dfrac{x}{p_l}+\dfrac{y}{2f}+1<N_l\\ N_l & , \ \dfrac{x}{p_l}+\dfrac{y}{2f}+1\ge N_l\end{cases}, \tag{4.12}$$

where $\lceil x \rceil$ is ceiling function of x, $\lfloor x \rfloor$ is floor function of x and N_l is the number of lens array.

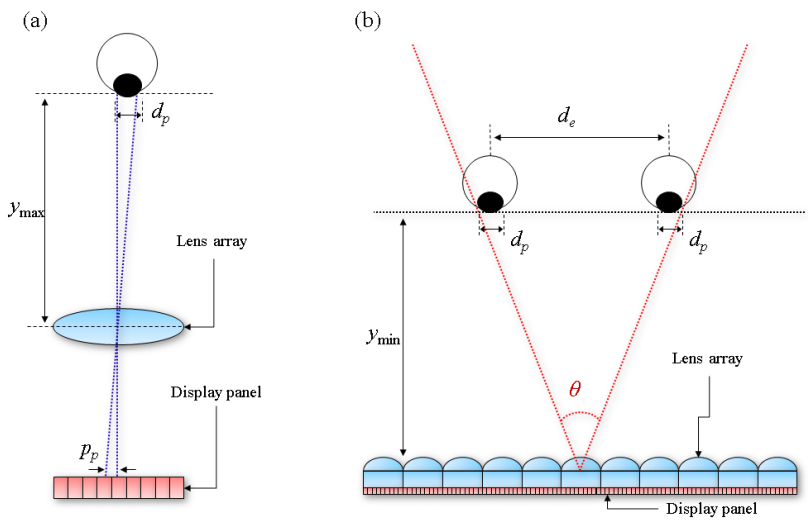

Figure 4.14 Super multi-view condition in integral imaging: (a) condition of disparity between two views in same eye pupil, (b) condition of binocular disparity

As shown in Figure 4.14(a), two different views which are formed at the same eye pupil have at least one pixel disparity without flipping problem to satisfy the SMV condition. Figure 4.14(b) shows the other condition of integral imaging to reconstruct 3D image, which is the binocular disparity condition. From the SMV and binocular disparity

condition, the observer distance from the position of lens array is limited between y_{max} and y_{min} as follows:

$$y_{\min} = \frac{f\left(d_e + d_p\right)}{p_l}, \quad y_{\max} = \frac{f d_p}{p_p}. \tag{4.13}$$

If the observer is located out of the range between y_{min} and y_{max} or y_{min} is bigger than y_{max}, the SMV condition is dissatisfied and then accommodation response does not occur in integral imaging.

4.2.3 Expressible depth range and size of 3D object in integral imaging with super multi-view condition

In integral imaging, the expressible depth range with SMV condition and the width of 3D object is also limited by intersection of each view as shown in Figure 4.15. The 3D object has to be reconstructed between the plane of lens array and $d_{max}(x, y)$ when the observer is located at (x, y), and then the width of 3D object $w_{max}(d_{obj})$ is also limited by the depth of 3D object d_{obj}.

Equation (4.14) shows the maximum depth of 3D object by the observer position $d_{max}(x, y)$ and the maximum width of 3D object by the depth of 3D object $w_{max}(d_{obj})$ where the $N_{max}(x, y)$ and $N_{min}(x, y)$ are the maximum and minimum lens number at the observer position (x, y).

$$\begin{aligned} d_{\max}\left(x,y\right) &= \frac{\left[N_{\max}\left(x,y\right) - N_{\min}\left(x + d_e + d_p, y\right)\right] p_l y}{\left(d_e + d_p\right) + \left[N_{\max}\left(x,y\right) - N_{\min}\left(x + d_e + d_p, y\right)\right] p_l}, \\ w_{\max}\left(d_{obj}\right) &= \frac{\left[d_{\max}\left(x,y\right) - d_{obj}\right] p_l}{d_{\max}\left(x,y\right)} \\ &\quad \times \left[N_{\max}\left(x,y\right) - N_{\min}\left(x + d_e + d_p, y\right)\right]. \end{aligned} \tag{4.14}$$

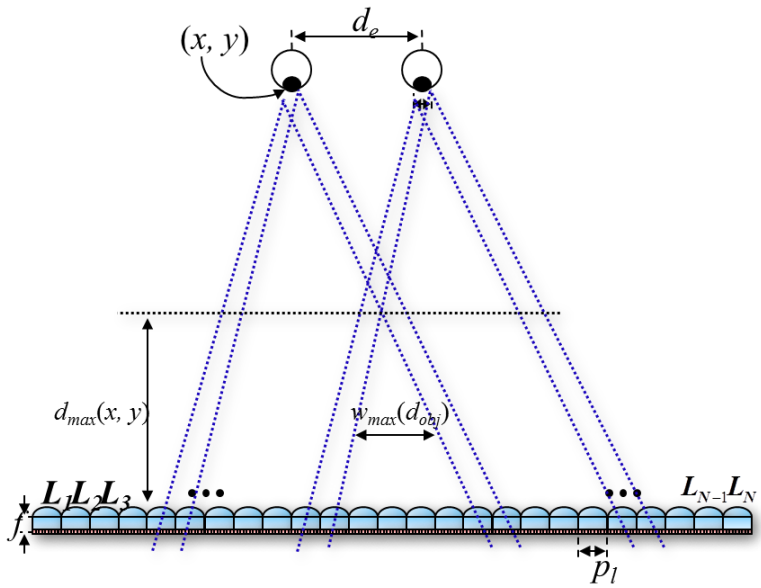

Figure 4.15 Expressible depth range and object size with super multi-view condition in integral imaging

4.2.4 **Simulation**

As shown in Eqs. (4.12), (4.13) and (4.14), the viewing region is limited by 3 different conditions such as filliped image condition, binocular disparity condition and SMV condition. I perform the simulation of viewing region satisfying SMV condition in integral imaging to verify the analysis.

Figure 4.16 shows the simulation result of SMV region in integral imaging with different lens specification when the observer is located 400 mm in front of lens array. As shown in Figure 4.16(a), the observer distance is limited between y_{max} of 650 mm and y_{min} of 143 mm when the lens pitch is 5 mm, focal length is 10 mm and pixel pitch is 0.1 mm. The blue rays from lens array to observer position are the rays in the non-flipped area, while the red dashed rays reconstruct flipped 3D image at the observer position. If the observer is located inside of the SMV region colored yellow, the reconstructed 3D image is satisfied with the SMV condition in integral imaging. Although the observer in the outside of yellow region can see the reconstructed 3D object, the SMV condition cannot be satisfied and the accommodation response will be different in the case of satisfying

SMV condition.

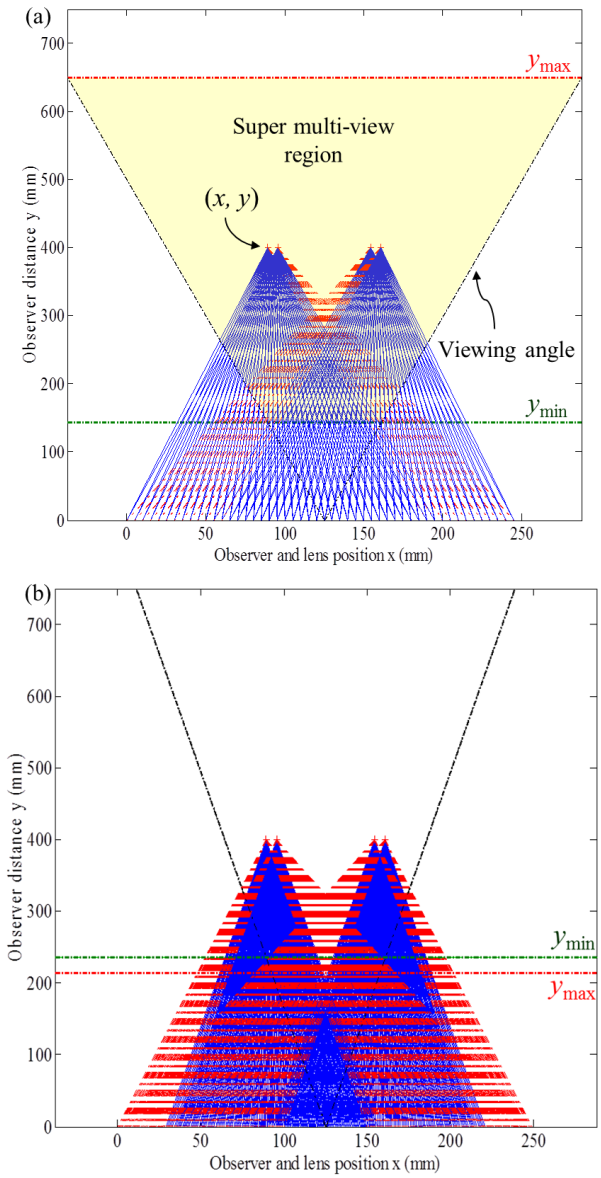

Figure 4.16 Simulation result of super multi-view region in integral imaging: (a) integral imaging with super multi-view condition (5 mm lens array), (b) integral imaging without super multi-view condition (1 mm lens array)

However, the case of 1 mm lens array with 3.3 mm focal length cannot satisfy the

SMV condition because the y_{min} of 236.0 mm is bigger than y_{max} of 214.5 mm as shown in Figure 4.16(b). The observer inside the black lines, which are the boundaries of viewing angle of integral imaging, can see the 3D object without flipping problem, but the satisfaction of SMV condition is impossible at all locations in viewing region.

Figure 4.17 shows the simulation result with observed view images at 4 different eye and pupil positions for different lens specifications. The resolution of observed view image is the same as the number of lens arrays in focal mode integral imaging. As shown in Figure 4.17(a), the observed view images at the SMV positions with 5 mm lens array have disparities without flipping problem, which induce accommodation response. On the other hands, the case of 1mm lens array shows the flipped and inappropriate disparities as shown in Figure 4.17(b), which comes from dissatisfaction of the SMV condition in integral imaging.

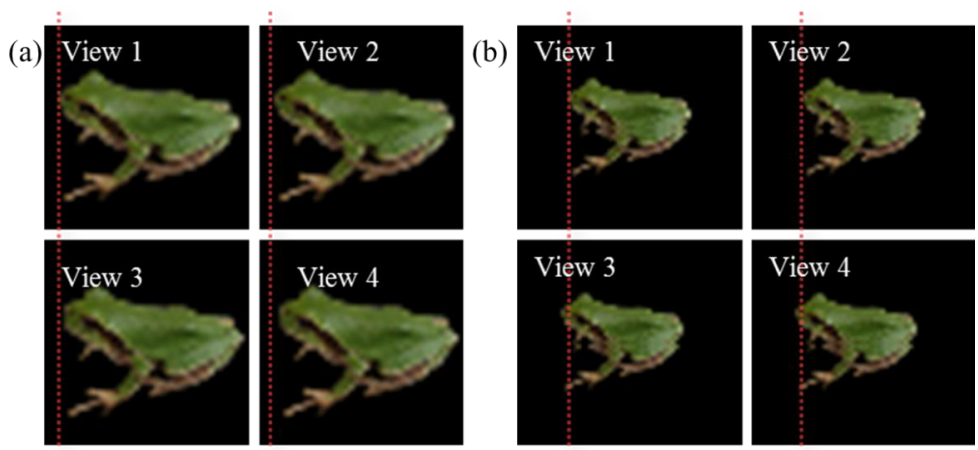

Figure 4.17 Simulation result of observed view images at (x, y), ($x+d_p$, y), ($x+d_e$, y) and ($x+d_e+d_p$, y): (a) view images with 5 mm lens array, (b) view images with 1 mm lens array

4.2.5 **Accommodation response with super multi-view condition in integral imaging**

To verify the simulation result, I evaluate the accommodation response of two different experimental setups of integral imaging using autorefractometer as shown in Figure 4.18. I use WAM-5500 autorefractometer of Grand Seiko for measuring accommodation

response of 3D display which is composed of 1 mm or 5 mm lens array, same as simulation specification, and 3840 by 2400 resolution 22-inch display panel.

To reveal the relation between the SMV condition and the accommodation response of integral imaging, I reconstruct the 3D image 50 mm in front of lens array using integral imaging with 5 mm and 1 mm lens arrays. As above-mentioned lens specification in simulation result, the case of 1 mm cannot satisfy the SMV condition in integral imaging and the specification of 5 mm lens array can satisfy the SMV condition in integral imaging. Accommodation response is measured by autorefractometer in 30 times per each case, such as lens surface, the case of 5 mm lens array and the case of 1 mm lens array. I set the reference of accommodation response to the accommodation of two-dimensional image at the surface of lens array which is located 500 mm in front of the observer.

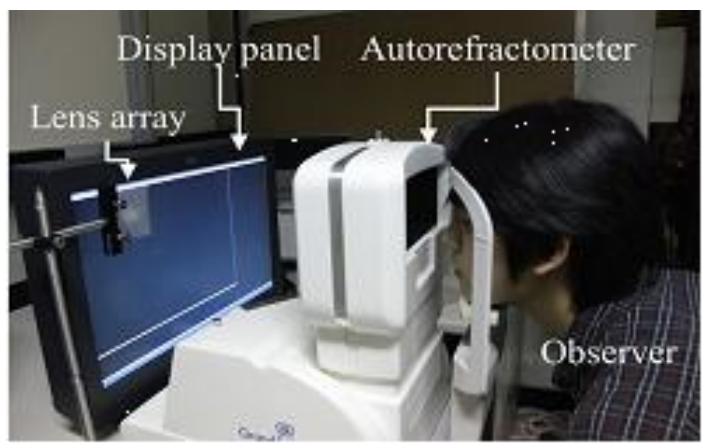

Figure 4.18 Experimental setup

4.2.6 **Experimental result**

Table 4.4, 4.5 and 4.6 show evaluation results of accommodation response of 3 different subjects with real target object located at lens surface, reconstructed 3D image by using 1 mm lens array, reconstructed 3D image by using 5 mm lens array and real target object located 50 mm in front of lens array. Figure 4.19 shows the evaluation results of accommodation response with 5 mm and 1 mm lens arrays and the real target object as reference in diopter and meter units. As shown in Figure 4.19, the accommodation response with the SMV condition in integral imaging (the case of 5 mm lens array) is

more similar to the actual accommodation response than the accommodation response without the SMV condition in integral imaging (the case of 1mm lens array). In the case of 1mm lens array, the accommodation response is fixed at the surface of lens array because of dissatisfaction of SMV condition. However, in the case of 5 mm lens array, the accommodation response is changed to the situation of real 3D object located at 50 mm in front of lens array.

From the results, we see that the accommodation response of 3D image with SMV condition is the same as real target object by about 90%, which corresponds to 40% increment compared with the case and without SMV. The observer who is inside the SMV region in integral imaging can feel the 3D effect with relief of accommodation-convergence conflict. Although integral imaging can lead to accommodation response when the observer watches the reconstructed 3D object, it depends on the specification of lens and the observer position. Therefore, the experimental results show that integral imaging with the SMV region can relieve the AC-CV conflict.

Table 4.4 Accommodation response of observer A

Mode	Lens surface		1 mm lens array		5 mm lens array		Real target	
Power	*Sph.	**Cyl.	Sph.	Cyl.	Sph.	Cyl.	Sph.	Cyl.
Accommodation response (D)	-1.495	-0.655	-1.335	-0.815	-1.56	-0.84	-1.85	-0.29
	-1.43	-0.84	-1.185	-1.055	-1.525	-0.91	-1.86	-0.26
	-1.215	-0.845	-1.155	-0.99	-1.515	-0.97	-1.71	-0.35
	-1.35	-0.885	-1.41	-0.835	-1.61	-0.915	-1.63	-0.47
	-1.415	-0.85	-1.46	-0.73	-1.655	-1.055	-1.72	-0.43
	-1.455	-0.58	-1.47	-0.695	-1.615	-0.755	-1.79	-0.25
	-1.47	-0.475	-1.415	-0.995	-1.45	-0.43	-1.86	-0.05
	-1.5	-0.53	-1.515	-0.77	-1.24	-0.33	-1.89	-0.05
	-1.48	-0.515	-1.23	-1.08	-1.385	-0.425	-1.98	-0.16
	-1.375	-0.61	-1.11	-0.99	-1.4	-0.62	-1.88	-0.07
Mean (D)	-1.4185	-0.6785	-1.3285	-0.8955	-1.4955	-0.725	-1.817	-0.238
***SEP (D)		-1.75775		-1.77625		-1.858		-1.936

*Spherical power (Sph.), **Cylindrical power (Cyl.), ***Spherical Equivalent Power (SEP)

Table 4.5 Accommodation response of observer B

Mode	Lens surface		1 mm lens array		5 mm lens array		Real target	
Power	Sph.	Cyl.	Sph.	Cyl.	Sph.	Cyl.	Sph.	Cyl.
Accommodation response (D)	-1.5	-0.115	-1.425	-0.55	-1.35	-0.76	-2	-0.19
	-1.42	-0.185	-1.335	-0.62	-1.29	-0.61	-1.73	-0.26
	-1.415	-0.07	-1.06	-0.6	-1.37	-0.6	-1.88	-0.34
	-1.535	-0.05	-1.15	-0.63	-1.41	-0.57	-1.76	-0.26
	-1.46	-0.045	-1.02	-0.62	-1.47	-0.72	-1.75	-0.33
	-1.22	-0.29	-1.48	-0.78	-1.38	-0.66	-1.85	-0.06
	-1.195	-0.38	-1.355	-0.76	-1.21	-0.67	-1.78	-0.28
	-1.295	-0.485	-1.275	-0.695	-1.25	-0.64	-1.73	-0.28
	-1.385	-0.545	-1.345	-0.635	-1.21	-0.63	-1.71	-0.2
	-1.31	-0.525	-1.095	-0.64	-1.16	-0.62	-1.6	-0.32
Mean (D)	-1.3735	-0.269	-1.254	-0.653	-1.31	-0.648	-1.779	-0.252
SEP (D)		-1.508		-1.5805		-1.634		-1.905

Table 4.6 Accommodation response of observer C

Mode	Lens surface		1 mm lens array		5 mm lens array		Real target	
Power	Sph.	Cyl.	Sph.	Cyl.	Sph.	Cyl.	Sph.	Cyl.
Accommodation response (D)	-1.75	-0.25	-1.31	-0.51	-1.68	-0.435	-1.69	-0.33
	-1.5	-0.25	-1.34	-0.435	-1.675	-0.425	-1.74	-0.32
	-1.5	-0.25	-1.42	-0.35	-1.66	-0.35	-1.89	-0.26
	-1.5	-0.5	-1.26	-0.345	-1.705	-0.075	-1.92	-0.26
	-1.5	-0.5	-1.415	-0.325	-1.78	-0.055	-1.82	-0.28
	-1.25	-0.5	-1.335	-0.47	-1.655	-0.33	-2.02	-0.29
	-1.25	-0.5	-1.235	-0.535	-1.635	-0.37	-1.95	-0.28
	-1.25	-0.5	-1.43	-0.23	-1.625	-0.27	-1.9	-0.28
	-1.25	-0.5	-1.51	-0.045	-1.665	-0.14	-1.94	-0.2
	-1.25	-0.5	-1.52	-0.04	-1.665	-0.18	-1.94	-0.26
Mean (D)	-1.4	-0.425	-1.3775	-0.3285	-1.6745	-0.263	-1.881	-0.276
SEP (D)		-1.6125		-1.54175		-1.806		-2.019

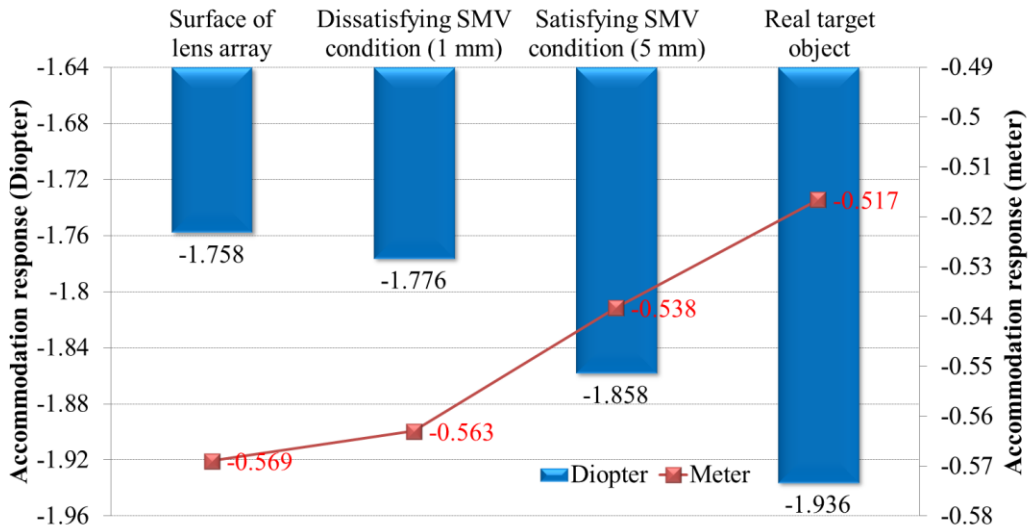
Surface of lens array
Dissatisfying SMV condition (1 mm)
Satisfying SMV condition (5 mm)
Real target object
Accommodation response (Diopter)
Accommodation response (meter)
-1.64
-1.68
-1.72
-1.76
-1.8
-1.84
-1.88
-1.92
-1.96
-0.49
-0.5
-0.51
-0.52
-0.53
-0.54
-0.55
-0.56
-0.57
-0.58
-1.758
-1.776
-1.858
-1.936
-0.569
-0.563
-0.538
-0.517
Diopter
Meter

(a)

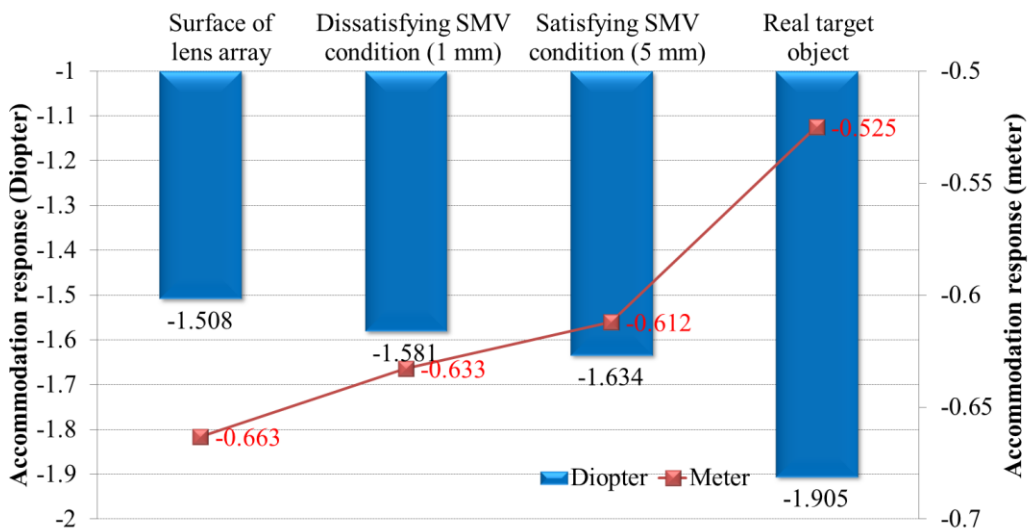
Surface of lens array
Dissatisfying SMV condition (1 mm)
Satisfying SMV condition (5 mm)
Real target object
Accommodation response (Diopter)
Accommodation response (meter)
-1
-1.1
-1.2
-1.3
-1.4
-1.5
-1.6
-1.7
-1.8
-1.9
-2
-0.5
-0.55
-0.6
-0.65
-0.7
-1.508
-1.581
-1.634
-1.905
-0.663
-0.633
-0.612
-0.525
Diopter
Meter

(b)

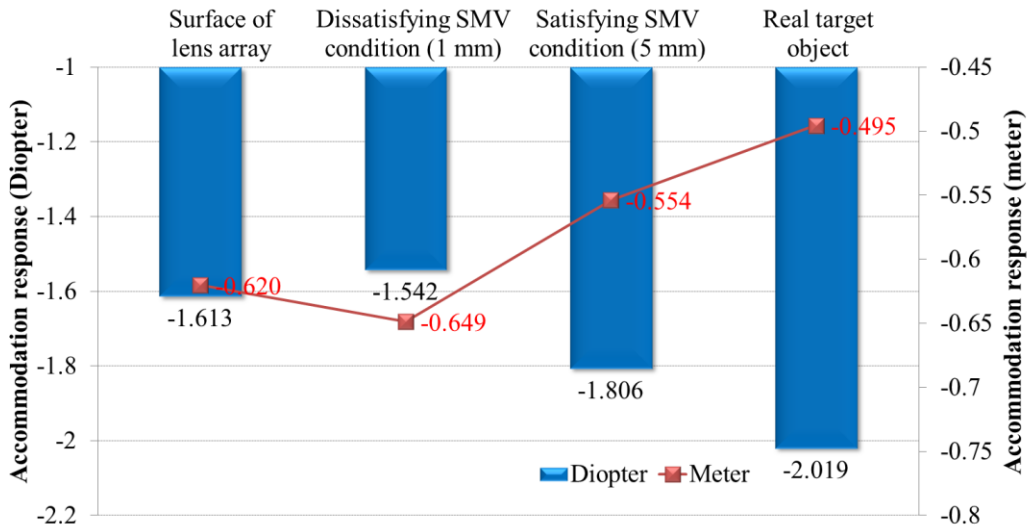

(c)

Figure 4.19 Experimental results of accommodation response with different lens specifications: (a) accommodation response of observer A, (b) observer B and (c) observer C

4.2.7 **Experimental result**

To my knowledge, this is the first study about the SMV region in integral imaging and relation between the SMV condition and accommodation response of integral imaging. I reveal the SMV region of integral imaging with various lens specifications. The observer inside the SMV region in integral imaging can feel the 3D effect with relief of AC-CV conflict. Although the observer watches the reconstructed 3D image using integral imaging, the observer will suffer from the AC-CV conflict at outside of the SMV region in integral imaging. This research will be helpful to find human factors for perceiving 3D image.

Chapter 5

Conclusion

This dissertation presents studies on improvement of three-dimensional (3D) displays based on multi-view display and pinhole-type integral imaging. Among various types of 3D displays, integral imaging and multi-view display such as parallax barrier and lenticular 3D display are almost commercialized autostereoscopic 3D display. For commercialization, autostereoscopic 3D display has three issues that are limitation of display technology, human factors related on human visual system and optical information processing technology. In this dissertation, the author addresses the studies about the improvement methods for multi-view display and pinhole-type integral imaging in the three issues.

In the issue of display technology, the improvement methods of pinhole-type integral imaging using electroluminescent (EL) film and color filters on display panel are proposed to enhance the viewing angle, resolution, ray density and two-dimension (2D)/3D convertibility. For large expressible depth range and 2D/3D convertibility in pinhole-type integral imaging, pinhole-type integral imaging is modified by new light source conversion layer based on EL film. The EL film has the advantage that it can operate continuously even when it is cut or punctured. Using this characteristic, the author generates an array of pinholes on an EL film to form a point light source array for reconstructing 3D images based on integral imaging. Taking advantage of the flexibility of EL films, a 2D/3D convertible integral imaging system with a wide viewing angle using a curved EL film is proposed which is extended to 360-degree viewable cylindrical

3D display system. For enhancement of ray density, resolution and expressible depth range in pinhole-type integral imaging, the pinhole-type integral imaging using color filter pinhole array on liquid crystal display panel with projection scheme is proposed. A color filter structure on liquid crystal display panel acts as pinhole array in integral imaging with separation of color channel. The use of color filter pinhole array and projection scheme can enlarge the region of one-elemental image and improve the resolution and ray density remarkably.

In addition to the improvement of pinhole-type integral imaging, analysis and convergence of multi-view display and one-dimensional (1D) integral imaging are presented for improvement of characteristics in autostereoscopic display. For the convergence of two different autostereoscopic 3D display, multi-view display and integral imaging, light field analysis of spatio-angular distribution and its frequency domain analysis are performed. From the analysis, the convergence type of autostereoscopic 3D display based on multi-view display and 1D integral imaging is proposed by using time-multiplexing and sub-pixel multiplexing technique.

As another issue in autostereoscopic 3D display, the depth resolution and accommodation response of human factors in multi-view display and integral imaging are researched. To find the effect of fundamental depth resolution and cardboard effect to the perceived depth resolution in multi-view display, the fundamental depth resolution and the cardboard effect from the synthesis process in the multi-view 3D TV broadcasting are analyzed and the subjective tests are performed. In addition, the analysis and measurement of accommodation response of integral imaging satisfying SMV condition is performed to reveal the relation between the accommodation response of integral imaging and SMV condition.

On the other issue of autostereoscopic 3D display, the optical information processing from elemental image and multi-view images in depth extraction, reconstruction of occluded region and reacquisition of 3D object are presented. More accurate depth extraction algorithm using optical flow from sub-images of elemental image is proposed and its applications are also presented in this dissertation. The depth extraction and reconstruction of 3D object using optical flow and triangular mesh reconstruction with sub-pixel accuracy can be adopted to the reconstruction of occluded region in 3D objects.

In addition, computational reacquisition for real 3D object in integral imaging is proposed without pseudoscopic problem from the 3D object reconstruction with sub-pixel accuracy.

Throughout the dissertation, analysis and enhancements of autostereoscopic 3D display are proposed in display technology, human factor and optical information processing issues. The studies about improvement of multi-view display and integral imaging in three issues are helpful to the commercialization of autostereoscopic 3D display.

Bibliography

1. N. A. Dodgson and A. Neil, "Autostereoscopic 3D Displays," Computer **38**, 31-36 (2005).

2. C. Wheatstone, "Contributions to the physiology of vision. Part the first. On some remarkable, and hitherto unobserved, phenomena of binocular vision," Philos. Trans. R. Soc. London **128**, 371-394 (1838).

3. J. Hong, Y. Kim, H.-J. Choi, J. Hahn, J.-H. Park, H. Kim, S.-W. Min, N. Chen, and B. Lee, "Three-dimensional display technologies of recent interest: principles, status, and issues," Appl. Opt. **50**, H87-H115 (2011).

4. G. Lippmann, "La photographie integrale," C. R. Acad. Sci. **146**, 446-451 (1908).

5. T. Kawai, "3D displays and applications," Displays **23**, 49-56 (2002).

6. E.-S. Kim, "Three-dimensional projection display system," in *Digital Holography and Three-Dimensional Display*, T.-C. Poon, ed. (Springer, 2006), pp. 302-315.

7. K.-C. Kwon, Y.-T. Lim, N. Kim, Y.-J. Song, and Y.-S. Choi, "Vergence control of binocular stereoscopic camera using disparity information," J. Opt. Soc. Korea **13**, 379-385 (2009).

8. A. Kubota, A. Smolic, M. Magnor, M. Tanimoto, T. Chen, and C. Zhang, "Multiview imaging and 3DTV," IEEE Signal Processing Magazine **24**, 10-21 (2007).

9. M. Okutomi and T. Kanade, "A multiple-baseline stereo," IEEE Transactions on Pattern Analysis and Machine Intelligence **15**, 353-363 (1993).

10. B. Lee, J.-H. Park, and S.-W. Min, "Three-dimensional display and information processing based on integral imaging," in *Digital Holography and Three-Dimensional Display*, Ting-Chung Poon, ed. (Springer, 2006), pp. 333-378.

11. Y. Kim, K. Hong, and B. Lee, "Recent researches based on integral imaging display method," 3D Research **1**, 17-27 (2010).

12. D. Minoli, "3DTV/3DV encoding approaches," in *3DTV Content Capture, Encoding and Transmission: Building the Transport Infrastructure for Commercial Services* (John Wiley and Sons, 2010), pp. 47-80.

13. C. van Berkel, J. A. Clarke, and C. V. Berkel, "Characterization and optimization of 3D-LCD module design," Proc. SPIE **3012**, 179-186 (1997).

14. C. van Berkel, "Image preparation for 3D LCD," Proc. SPIE **3639**, 84-91 (1999).

15. Y.-G. Lee and J. B. Ra, "New image multiplexing scheme for compensating lens mismatch and viewing zone shifts in three-dimensional lenticular displays," Opt. Eng. **48**, 044001 (2009).

16. H. Kim, J. Hahn, and H.-J. Choi, "Numerical investigation on the viewing angle of a lenticular three-dimensional display with a triplet lens array," Appl. Opt. **50**, 1534-1540 (2011).

17. J.-C. Liou and F.-H. Chen, "Design and fabrication of optical system for time-multiplex autostereoscopic display," Opt. Express **19**, 11007-11017 (2011).

18. C. Fehn, "Depth-image-based rendering (DIBR), compression, and transmission for a new approach on 3D-TV," Proc. SPIE **5291**, 93-104 (2004).

19. K.-jung Oh, A. Vetro, Y.-sung Ho, and S. Member, "Depth coding using a boundary reconstruction filter for 3-D video systems," IEEE Transactions on Circuits and Systems for Video Technology **21**, 350-359 (2011).

20. Y. Zhao, C. Zhu, Z. Chen, D. Tian, and L. Yu, "Boundary artifact reduction in view synthesis of 3D video: From perspective of texture-depth alignment," IEEE Transactions on Broadcasting **57**, 510-522 (2011).

21. J.-H. Jung, K. Hong, G. Park, I. Chung, J.-H. Park, and B. Lee, "Reconstruction of three-dimensional occluded object using optical flow and triangular mesh reconstruction in integral imaging.," Opt. Express **18**, 26373-87 (2010).

22. M. Tanimoto, T. Fujii, and K. Suzuki, "View synthesis algorithm in view synthesis reference software 2.0 (VSRS2.0)," ISO/IEC JTC1/SC29/WG11 Doc. M16090 (2009).

23. P. Benzie, J. Watson, S. Member, P. Surman, I. Rakkolainen, K. Hopf, H. Urey, V. Sainov, and C. V. Kopylow, "A survey of 3DTV displays : Techniques and technologies," Computer (2007).

24. F. Okano, H. Hoshino, J. Arai, and I. Yuyama, "Real-time pickup method for a three-dimensional image based on integral photography.," Appl. Opt. **36**, 1598-603 (1997).

25. J.-H. Park, S. Jung, H. Choi, Y. Kim, and B. Lee, "Depth extraction by use of a rectangular lens array and one-dimensional elemental image modification," Appl. Opt. **43**, 4882-4895 (2004).

26. M. Martinez-Corral, B. Javidi, R. Martínez-Cuenca, G. Saavedra, and R. Mart'inez-Cuenca, "Formation of real, orthoscopic integral images by smart pixel mapping," Opt. Express **13**, 9175-9180 (2005).

27. G. Passalis, N. Sgouros, S. Athineos, and T. Theoharis, "Enhanced reconstruction of three-dimensional shape and texture from integral photography images," Appl. Opt. **46**, 5311-5320 (2007).

28. D.-H. Shin and E.-S. Kim, "Computational integral imaging reconstruction of 3D object using a depth conversion technique," J. Opt. Soc. Korea **12**, 131-135 (2008).

29. J.-H. Park, G. Baasantseren, N. Kim, G. Park, J.-M. Kang, and B. Lee, "View image generation in perspective and orthographic projection geometry based on integral imaging," Opt. Express **16**, 8800-8813 (2008).

30. M. Zhang, Y. Piao, and E.-S. Kim, "Occlusion-removed scheme using depth-reversed method in computational integral imaging," Appl. Opt. **49**, 2571-2580 (2010).

31. S.-H. Hong and B. Javidi, "Distortion-tolerant 3D recognition of occluded objects using computational integral imaging," Opt. Express **14**, 12085-12095 (2006).

32. D.-H. Shin, B.-G. Lee, and J.-J. Lee, "Occlusion removal method of partially occluded 3D object using sub-image block matching in computational integral imaging," Opt. Express **16**, 16294-16304 (2008).

33. K.-J. Lee, D.-C. Hwang, S.-C. Kim, and E.-S. Kim, "Blur-metric-based resolution enhancement of computationally reconstructed integral images," Appl. Opt. **47**, 2859-2869 (2008).

34. C. M. Do and B. Javidi, "3D integral imaging reconstruction of occluded objects using independent component analysis-based K-means clustering," J. Disp. Tech **6**, 257-262 (2010).

35. J.-H. Park, K. Hong, and B. Lee, "Recent progress in three-dimensional information processing based on integral imaging," Appl. Opt. **48**, H77--H94 (2009).

36. M. Levo, P. Hanrahan, and M. Levoy, "Light field rendering," in *Proceedings of the 23rd Annual Conference on Computer Graphics and Interactive Techniques* (ACM, 1996), pp. 31-42.

37. B. Lee, S. Jung, S.-W. Min, and J.-H. Park, "Three-dimensional display by use of integral photography with dynamically variable image planes," Opt. Lett. **26**, 1481-1482 (2001).

38. K. Hong, J. Hong, J.-hyun Jung, J.-hyeung Park, and B. Lee, "Rectification of elemental image set and extraction of lens lattice by projective image transformation in integral imaging," Opt. Express **18**, 12002-12016 (2010).

39. F. Okano, H. Hoshino, J. Arai, and I. Yuyama, "Gradient-index lens-array method based on real-time integral photography for three-dimensional images.," Appl. Opt. **37**, 2034-45 (1998).

40. N. Davies, M. Mccormick, and L. Yang, "Three-dimensional imaging systems: a new development," Appl. Opt. **27**, 4520 (1988).

41. M. C. Forman, N. Davies, and M. McCormick, "Continuous parallax in discrete pixelated integral three-dimensional displays.," J. Opt. Soc. Am. A **20**, 411-20 (2003).

42. M. Martinez-Corral, B. Javidi, R. Martinez-Cuenca, G. Saavedra, M. Martínez-Corral, and R. Martínez-Cuenca, "Integral imaging with improved depth of field by use of amplitude-modulated microlens arrays," Appl. Opt. **43**, 5806-5813 (2004).

43. H. Liao, M. Iwahara, N. Hata, T. Dohi, I. Sakuma, T. Koike, Y. Momoi, T. Minakawa, M. Yamasaki, F. Tajima, and H. Takeda, "High-quality integral videography using a multiprojector," Opt. Express **12**, 1067-1076 (2004).

44. S.-W. Min, M. Hahn, J. Kim, and B. Lee, "Three-dimensional electro-floating display system using an integral imaging method," Opt. Express **13**, 4358-4369 (2005).

45. S. Jung, J. Hong, J.-H. Park, Y. Kim, and B. Lee, "Depth-enhanced integral-imaging 3D display using different optical path lengths by polarization devices or mirror barrier array," J. Soc. Inf. Display **12**, 461-467 (2004).

46. B. Lee, S.-W. Min, and B. Javidi, "Theoretical analysis for three-dimensional integral imaging systems with double devices," Appl. Opt. **41**, 4856-4865 (2002).

47. J. Ren, A. Aggoun, and M. McCormick, "Maximum viewing width integral image," J. Electronic Imaging **14**, 23019 (2005).

48. D.-C. Hwang, D.-H. Shin, S.-C. Kim, and E.-S. Kim, "Depth extraction of three-dimensional objects in space by the computational integral imaging reconstruction technique," Appl. Opt. **47**, D128--D135 (2008).

49. N. Sgouros, I. Kontaxakis, and M. Sangriotis, "Effect of different traversal schemes in integral image coding," Appl. Opt. **47**, D28--D37 (2008).

50. Y. Kim, J.-H. Park, H. Choi, S. Jung, S.-W. Min, and B. Lee, "Viewing-angle-enhanced integral imaging system using a curved lens array," Opt. Express **12**, 421-429 (2004).

51. S.-W. Min, J. Kim, and B. Lee, "Wide-viewing projection-type integral imaging system with an embossed screen.," Optics letters **29**, 2420-2 (2004).

52. Y. Kim, J.-H. Park, S.-W. Min, S. Jung, H. Choi, and B. Lee, "Wide-viewing-angle integral three-dimensional imaging system by curving a screen and a lens array," Appl. Opt. **44**, 546-552 (2005).

53. J. Kim, Y. Kim, H. Choi, S.-W. Cho, Y. Kim, J. Park, G. Park, and B. Lee, "Implementation of polarization-multiplexed tiled projection integral imaging system," J. Soc. Inf. Display **17**, 467-468 (2009).

54. J. Hong, J.-H. Park, S. Jung, and B. Lee, "Depth-enhanced integral imaging by use of optical path control.," Optics letters **29**, 1790-2 (2004).

55. H. Choi, Y. Kim, J. Kim, S.-W. Cho, and B. Lee, "Depth- and viewing-angle-enhanced 3-D/2-D switchable display system with high contrast ratio using multiple display devices and a lens array," J. Soc. Inf. Display **15**, 315 (2007).

56. J.-H. Park, H.-R. Kim, Y. Kim, J. Kim, J. Hong, S.-D. Lee, and B. Lee, "Depth-enhanced three-dimensional-two-dimensional convertible display based on modified integral imaging," Opt. Lett. **29**, 2734-2736 (2004).

57. H. Liao, T. Dohi, and M. Iwahara, "Improved viewing resolution of integral videography by use of rotated prism sheets.," Optics express **15**, 4814-22 (2007).

58. Y. Kim, S.-gi Park, S.-W. Min, and B. Lee, "Projection-type integral imaging system using multiple elemental image layers," Appl. Opt. **50**, B18--B24 (2011).

59. T. Okoshi, "Three-dimensional displays," Proc. IEEE **68**, 548-564 (1980).

60. H. Choi, J. Kim, S.-W. Cho, Y. Kim, J. B. Park, and B. Lee, "Three-dimensional-two-dimensional mixed display system using integral imaging with an active pinhole array on a liquid crystal panel," Appl. Opt. **47**, 2207-2214 (2008).

61. H. Choi, S.-W. Cho, J. Kim, and B. Lee, "A thin 3D-2D convertible integral imaging system using a pinhole array on a polarizer," Opt. Express **14**, 5183-5190 (2006).

62. S.-W. Cho, J.-H. Park, Y. Kim, H. Choi, J. Kim, and B. Lee, "Convertible two-dimensional-three-dimensional display using an LED array based on modified integral imaging," Opt. Lett. **31**, 2852-2854 (2006).

63. Y. Kim, H. Choi, S.-W. Cho, Y. Kim, J. Kim, G. Park, and B. Lee, "Three-dimensional integral display using plastic optical fibers," Appl. Opt. **46**, 7149-7154 (2007).

64. Y. Y. Kim, J. Kim, H. Choi, J.-H. Jung, and B. Lee, "Thin-type integral imaging method with an organic light emitting diode panel," Appl. Opt. **47**, 4927-4934 (2008).

65. J.-hyun Jung, Y. Kim, J. Kim, and B. Lee, "A thin 3D-2D convertible integral imaging system using a pinhole array on an electroluminescent (EL) sheet," in *DH 2008* (2008), pp. 3-5.

66. Y. A. Ono, *Electroluminescent Displays* (World Scientific, 1995), pp. 7-17.

67. S.-W. Min, B. Javidi, and B. Lee, "Enhanced Three-Dimensional Integral Imaging System by Use of Double Display Devices," Appl. Opt. **42**, 4186-4195 (2003).

68. S.-W. Min, S. S. Jung, J.-hyeung Park, B. Lee, and S.-wook Mm, "Three-dimensional display system based on computer-generated integral photography," Proc. SPIE **4297**, 187-195 (2001).

69. M. Martinez-Corral, B. Javidi, R. Martinez-Cuenca, G. Saavedra, M. Martínez-Corral, and R. Martínez-Cuenca, "Multifacet structure of observed reconstructed integral images," J. Opt. Soc. Am. A **22**, 597-603 (2005).

70. Y. Kim, J. Kim, J.-M. Kang, J.-H. Jung, H. Choi, and B. Lee, "Point light source integral imaging with improved resolution and viewing angle by the use of electrically movable pinhole array," Opt. Express **15**, 18253-18267 (2007).

71. S. Pastoor, M. Wijpking, and M. Wöpking, "3-D displays: A review of current technologies," Displays **17**, 100-110 (1997).

72. I. Sexton and P. Surman, "Stereoscopic and autostereoscopic display systems," IEEE Signal Processing Magazine **16**, 85-99 (1999).

73. A. Jones, I. McDowall, H. Yamada, M. Bolas, and P. Debevec, "Rendering for an interactive 360° light field display," ACM Trans. Graph. **26**, (2007).

74. G. E. Favalora, "Volumetric 3D displays and application infrastructure," Computer **38**, 37-44 (2005).

75. J.-H. Jung, Y. Y. Kim, J. Kim, K. Hong, and B. Lee, "Integral imaging system using an electroluminescent film backlight for three-dimensional-two-dimensional convertibility and a curved structure.," Appl. Opt. **48**, 998-1007 (2009).

76. J.-hyun Jung, Y. Y. Kim, J. Kim, and K. Hong, "An integral imaging system using electroluminescent film backlight for 3D-2D convertibility," Society **467**, 4856-4865 (2005).

77. J.-H. Jung, K. Hong, G. Park, I. Chung, and B. Lee, "360 ° -viewable cylindrical integral imaging system using a 3-D / 2-D switchable and flexible backlight," J. Soc. Inf. Display **18**, 527-534 (2010).

78. J.-Y. Son, V. V. Saveljev, Y.-J. Choi, J.-E. Bahn, S.-K. Kim, and H. Choi, "Parameters for designing autostereoscopic imaging systems based on lenticular, parallax barrier, and integral photography plates," Opt. Eng. **42**, 3326 (2003).

79. H. Hoshino, F. Okano, H. Isono, and I. Yuyama, "Analysis of resolution limitation of integral photography," J. Opt. Soc. Am. A **15**, 2059-2065 (1998).

80. D. Lanman, M. Hirsch, Y. Kim, R. Raskar, and O. S. Id, "Content-adaptive parallax barriers for automultiscopic 3D display," in *ACM SIGGRAPH Asia 2010* (ACM Press, 2010), Vol. 29, p. 1.

81. S.-W. Min, J. Kim, and B. Lee, "New characteristic equation of three-dimensional integral imaging system and its applications," Japanese Journal of Applied Physics **44**, L71-L74 (2005).

82. A. Isaksen, L. Mcmillan, and S. J. Gortler, "Dynamically Reparameterized Light Fields," in *ACM SIGGRAPH 2000* (2010), pp. 297-306.

83. A. Veeraraghavan, R. Raskr, A. Agrawal, A. Mohan, and J. Tumblin, "Dappled photography : Mask enhanced cameras for heterodyned light fields and coded aperture refocusing," ACM Trans. Graph. **26**, 69 (2007).

84. Z. Zhang and M. Levoy, "Wigner distributions and how they relate to the light field," in *Proc. IEEE International Conference on Computational Photography* (2009), pp. 1-10.

85. T. Koike, A. Yuuki, S. Uehara, K. Taira, G. Hamagishi, K. Izumi, T. Nomura, K. Mashitani, A. Miyazawa, T. Horikoshi, and H. Ujike, "Measurement of multi-view and integral photography displays based on sampling in ray space," in *IDW '08 Technical Digest (Niigata Convention Center, Japan, 2008)* (2008), pp. 1115-1118.

86. J.-H. Park and K.-M. Jeong, "Frequency domain depth filtering of integral imaging.," Optics express **19**, 18729-41 (2011).

87. J.-H. Kim, J.-H. Jung, J.-S. Hong, J. Yeom, and B.-H. Lee, "Elemental image generation method with the correction of mismatch error by sub-pixel sampling between lens and pixel in integral imaging," J. Opt. Soc. Korea **16**, 29-35 (2012).

88. A. J. Woods, T. Docherty, and R. Koch, "Image distortions in stereoscopic video systems," Proc. SPIE **1915**, 36-48 (1993).

89. H. Yamanoue, M. Okui, and I. Yuyama, "A study on the relationship between shooting conditions and cardboard effect of stereoscopic images," IEEE Transactions on Circuits and Systems **10**, 411-416 (2000).

90. H. Yamanoue, M. Okui, and F. Okano, "Geometrical analysis of puppet-theater and cardboard effects in stereoscopic HDTV images," IEEE Transactions on Circuits and Systems **16**, 744-752 (2006).

91. J. C. and P. Vishton, "Perceiving layout and knowing distances: The integration, relative potency, and contextual use of different information about depth," in *Perception of Space and Motion*, W. Epstein, ed. (Academic Press, 1995), pp. 90-131.

92. Philips (in Coop with 3D4YOU), "Response to New Call for 3DV Test Material: Beergarden," ISO/IEC JTC1/SC29/WG11 Doc. M16421 (2009).

93. T. Honda, M. Shimomatsu, H. Imai, S. Kobayashi, H. Nate, and K. Iwane, "Second version of 3-D display system by fan-like array of projection optics," Virtual Reality **5006**, 118-127 (2002).

94. Y. Kim, K. Hong, J. Kim, H. K. Yang, J.-M. Hwang, and B. Lee, "Accommodation measurement according to angular resolution density in three-dimensional display," Proc. SPIE **7956**, 79560Q-79560Q-7 (2011).

95. Y. Kim, J. Kim, K. Hong, H. K. Yang, J.-H. Jung, H. Choi, S.-W. Min, J.-M. Seo, J.-M. Hwang, and B. Lee, "Accommodative response of integral imaging in near distance," J. Disp. Tech **8**, 70-78 (2012).

96. Y. Takaki and N. Nago, "Multi-projection of lenticular displays to construct a 256-view super multi-view display.," Opt. Express **18**, 8824-35 (2010).

97. J. Nakamura, K. Tanaka, C.-H. Tsai, and Y. Takaki, "Reduced-view super multi-view display," Displays **7863**, 78631P-78631P-8 (2011).

Appendix

Portions of the work discussed in each chapter of this dissertation are also presented in the following publications:

[Chapter 2.1] J.-H. Jung, Y. Kim, Y. Kim, J. Kim, K. Hong, and B. Lee, "Integral imaging system using an electroluminescent film backlight for three-dimensional-two-dimensional convertibility and a curved structure," Applied Optics, vol. 48, no. 5, pp. 998-1007, 2009.

[Chapter 2.2] J.-H. Jung, K. Hong, G. Park, I. Chung, and B. Lee, "360-degree viewable cylindrical integral imaging system using three-dimensional/two-dimensional switchable and flexible backlight," Journal of the Society for Information Display, vol. 18, no. 7, pp. 527-534, 2010.

[Chapter 2.3] J.-H. Jung, S.-g. Park, Y. Kim, and B. Lee, "Integral imaging using color filter pinhole array on display panel," Optics Express (accepted for pubilcation)

[Chapter 4.1] J.-H. Jung, J. Yeom, J. Hong, K. Hong, S.-W. Min, and B. Lee, "Effect of fundamental depth resolution and cardboard effect to perceived depth resolution on multi-view display," Optics Express, vol. 19, no. 21, pp. 20468-20482, 2011.

한글 초록

최근 10년간, 디스플레이 시장은 미세 공정과 유기 및 무기 발광 소자의 발달로 인하여 급속도로 평판 디스플레이 시장으로 전환되었고, 보다 현실감 있는 영상을 재생하기 위한 노력을 통하여 2차원 고화질 영상의 시대에서 3차원 입체 영상의 시대로 전환되어 가고 있다. 이미 TV시장과 영화 시장에는 편광 방식의 안경을 이용한 3차원 디스플레이가 성공적으로 자리를 잡고 있으며, 이들을 활용한 컨텐츠 또한 지속적으로 제작되고 있다. 그러나 궁극적인 3차원 디스플레이를 향한 연구는 현재의 안경식 방식에서 안경을 착용하지 않으면서도 다시점의 3차원 영상을 관측할 수 있는 무안경식 3차원 디스플레이 방식으로 집중 되고 있다.

본 논문은 무안경식 3차원 디스플레이 방식 중 다시점 디스플레이와 핀홀형 집적영상에 기반을 둔 3차원 디스플레이의 개선에 관한 연구이다. 지금까지 연구된 다양한 3차원 디스플레이 방식 중, 패럴랙스 배리어, 렌티큘러와 같은 다시점 디스플레이와 집적영상은 가장 상용화에 가까운 무안경식 3차원 디스플레이 방식이다. 그러나 무안경식 3차원 디스플레이의 상용화를 위해서는 디스플레이 기술, 관찰자의 인지요인, 그리고 광학적 정보처리 기술의 세 가지 측면에서의 문제점들에 대한 논의가 필요하다. 이 논문은 무안경식 3차원 디스플레이 중, 다시점 디스플레이와 핀홀(pinhole)형 집적영상을 이 세 가지 측면에서 개선하는 연구에 대한 내용을 담고 있다.

먼저 디스플레이 기술적인 측면에서는, 전계발광소자(electroluminescent film) 혹은 평판 디스플레이에 배열된 컬러 필터를 이용하여 핀홀형 집적영상의 시야각, 해상도, 광선 집적도 그리고 2차원/3차원 변환을 개선하는 방법들을

제안한다. 먼저 깊이 표현 범위가 기본적으로 넓은 핀홀형 집적영상의 2차원/3차원 변환으로의 확장을 위하여 전계발광소자에 기반을 둔 새로운 광원 변환 기술을 제안한다. 전계발광소자는 기본적으로 자르거나 휘거나 혹은 구멍을 뚫어도 발광에 영향을 받지 않는 특성을 가지고 있어, 전계발광소자에 균일한 핀홀을 배열하여 기존의 핀홀형 집적영상으로 이용이 가능하다. 따라서 이를 이용하여, 2차원/3차원 변환이 가능한 집적영상을 설계할 수 있고, 구부리면서 발광 상태를 유지하는 특성을 이용하여 광시야각을 갖는 반원 형태의 3차원 디스플레이로 제작할 수 있다. 또한 360도 전체에서 관찰이 가능한 집적영상 기반의 3차원 디스플레이로 확장하여 제안한다. 그리고 현재 대중적으로 사용되는 액정 디스플레이상의 컬러 필터 층을 핀홀 배열과 빔 프로젝터를 이용하여 광선 집적도, 해상도 그리고 깊이 표현 범위를 확장한 핀홀형 집적영상으로 제안한다. 실제 액정 디스플레이상의 컬러 필터는 3가지 색으로 나뉘어져 있고, 이를 이용하여 각각 색 영역이 다른 핀홀 배열로 사용이 가능하다. 이와 함께 빔 프로젝터를 이용하여, 한 요소 영상의 영역이 기존의 방식에 비해 넓어지고 서로 침범할 수 있게 되어 해상도와 광선 집적도가 최대 3배 향상되는 것을 확인할 수 있다.

집적영상의 개선과 함께 디스플레이 측면에서의 개선에서는, 무안경식 3차원 디스플레이의 특성을 개선하기 위하여 다시점 디스플레이와 1차원 집적영상을 분석하고 융합하는 연구도 진행한다. 두 가지의 다른 무안경식 3차원 디스플레이 방식을 융합하기 위하여, light field를 이용한 공간-각도 분포 분석과 이의 주파수영역에서의 분석을 진행한다. 분석을 통해 얻어진 두 방식의 공간-각도 분포 특징을 이용하여 다시점 디스플레이와 1차원 집적영상을 시분할 및 부픽셀분할을 통해 한 디스플레이 상에서 구현하여, 보다 품질이 향상된 무안경식 3차원 디스플레이를 제안한다.

또 다른 무안경식 3차원 디스플레이의 과제는 관찰자의 인지 요소로, 본 논문에서는 다시점 디스플레이와 집적영상에서의 깊이 해상도 및 조절력 반응에 대한 연구를 진행한다. 먼저 다시점 디스플레이 상에서 3차원 디스플레이 자체의 해상도와 cardboard 효과에 의한 인지 깊이 해상도 변화를 살펴보기 위해,

다시점 디스플레이 기반의 3차원 방송 환경을 구축하고, 디스플레이 자체의 깊이 해상도 표현의 제한, 다시점 영상 합성 과정 중의 깊이 해상도 표현의 제한 그리고 cardboard 효과에 의한 깊이 해상도 제한을 수식적으로 분석하고, 관찰자를 대상으로 한 설문을 진행한다. 이를 통해, 다시점 3차원 디스플레이 방송 환경에서 3차원 영상을 위한 깊이정보의 해상도를 위한 기준을 제시한다. 또한 무안경식 3차원 디스플레이에서 수렴-조절의 충돌을 해결하기 위해 논의되고 있는 초다시점 조건과 집적영상의 상관관계를 밝히기 위하여, 집적영상에서 초다시점 조건을 만족하는 영역을 분석 및 시뮬레이션을 진행하고 이 영역 안과 밖에서 관찰자의 조절력을 측정한다. 이 과정을 통해, 집적영상에서 초다시점 조건과 관찰자의 조절력 변화와의 상관관계를 찾을 수 있다.

그리고 무안경식 3차원 디스플레이를 이용한 또 다른 과제인 광학적 정보처리에서는, 요소영상과 다시점 영상을 이용한 깊이 추출과 3차원 영상의 재획득에 대한 연구를 진행한다. Optical flow에 기반을 둔 보다 정확한 깊이 추출 알고리즘을 이용하여 요소영상에서 추출한 부영상의 깊이를 추출하는 방법과 이의 응용에 대해 본 논문에서 설명한다. Optical flow에 기반을 둔 3차원 물체의 깊이 추출을 컴퓨터를 이용한 실사 3차원 영상의 재획득에 활용하는 경우, 집적영상의 본질적인 문제인 pseudoscopic 문제를 해결할 수 있다.

본 논문을 통한 무안경식 3차원 디스플레이의 디스플레이 기술, 관찰자의 인지요인, 그리고 광학적 정보처리 기술적인 측면에서의 개선 방법들은 추후 무안경식 3차원 디스플레이 시장의 확대와 가정용 TV시장으로의 진출에 크게 기여할 수 있을 것으로 보인다.

주요어 : 3 차원 디스플레이, 다시점 디스플레이, 집적영상, 핀홀형 집적영상, 깊이 해상도, 조절력 측정, 깊이 추출

학번 : 2007-21085